ATOMIC LAYER DEPOSITION OF NANOSCALE ALUMINUM SUPERCONDUCTING MATERIAL

サーメー, アハメド オカシャ ザキ モハメド

ATOMIC LAYER DEPOSITION OF NANOSCALE ALUMINUM SUPERCONDUCTING MATERIAL

Ph.D. Thesis
Submitted as partial fulfillment of the requirements for the degree
Doctorate of Philosophy

by

SAMEH AHMED OKASHA ZAKI MOHAMED

3ES18111G

Department of Molecular and Material Sciences
Interdisciplinary Graduate School of Engineering Sciences
Kyushu University,
Japan

2023

A dissertation

submitted

to the Interdisciplinary Graduate School of Engineering Sciences,

Kyushu University

to obtain the Degree of

Doctor of Philosophy

Supervised by

Prof. Yuichi Harada

Professor at Global Innovation Center, Kyushu University, Japan.

Inspected by

Prof. Hiroki Ago

Professor at Global Innovation Center, Kyushu University, Japan.

Associate Prof. Keisuke Yamamoto

Interdisciplinary Graduate School of Engineering and Sciences,

Kyushu University,

Japan

This thesis has been approved by the

Supervisor: Prof. Yuichi Harada

Composition of the doctoral committee:

Prof. Hiroki Ago
Professor at Global Innovation Center, Kyushu University, Japan.

Assoc. Prof. Keisuke Yamamoto
Interdisciplinary Graduate School of Engineering and Sciences, Kyushu University, Japan

Collaboration Members:

Dr.Yoshiaki Sekine

NTT Basic Research Laboratories, NTT Corporation

Dr. Satoshi Sasaki

NTT Basic Research Laboratories, NTT Corporation

Contents

Table of figures

List of Tables

List of abbreviations

SEM	Scanning Electron Microscopy
XRD	X-ray Diffraction
ALD	Atomic layer deposition
Al	Aluminum
Al_2O_3	Aluminum oxide
DMEAA	Dimethylethylamine alane
TMA	Trimethylaluminum
DMAH	Dimethylaluminum hydride
AlH_3	Alane
Ti	Titanium
FWHM	Full width at half maximum
M	Metal
Me	Methyl
CVD	Chemical Vapor deposition
DFT	Density functional theory
JJ	Josephson junction
SQUIDs	Superconducting quantum interferometer device
SCB	Single Cooper pair box
MQC	Macroscopic Quantum Coherence
Rf	Radio frequency
φ	Superconducting phase difference
S	Superconducting electrodes

N	Normal metal
dc	Direct current
E_j	Josephson junction energy
CNT	Carbon nanotube
M_L	Monolayer
PV	Peak-to-valley
RMS	Root mean square
T_C	Superconducting critical temperature
MQT	Macroscopic quantum tunneling

SUMMARY

This thesis outlines the growth of thin aluminum films and aluminum nanoparticles through the use of atomic layer deposition (ALD) and the subsequent characterization of these films and nanoparticles. We utilized dimethylethylamine alan (DMEAA) as the aluminum precursor. Our investigations focused on the morphology and crystal orientation of both the thin films and nanoparticles, and we also examined the superconducting properties of the thin aluminum films.

Our key findings are as follows:

1. The ALD growth conditions were optimized for achieving approximately a single layer using DMEAA for aluminum films.

2. It was found that the DMEAA precursor requires a metallic underlayer to enable the growth of aluminum films on silicon (Si) substrates. This property can be used for area-defined thin film growth. Furthermore, the growth of an aluminum film on very thin insulators, as thin as 2 nm can be achieved to obtain the tunnel effect.

3. In the absence of a metallic underlayer, we found that aluminum nanoparticles can be grown on Si substrates under certain conditions, and they exhibit distinct crystal structures.

4. Both thin aluminum films and aluminum nanoparticles exhibit a (111) orientation on Si (100) substrates.

5. Remarkably, the grown thin films of aluminum exhibited the same superconducting transition temperature and critical magnetic field as bulk aluminum. In usual aluminum films by other growth methods thin aluminum films tend to show enhanced superconductivity

resulted from lattice stress and impurity effects. Our result may imply that thin aluminum films are ideal.

6. These findings regarding aluminum films suggest that ALD growth using the DMEAA precursor can be employed to fabricate lateral small Josephson junctions with controlled junction areas achieved through a metallic underlayer. This development could solve the scalability challenges associated with current superconducting qubits, which are traditionally based on shadow evaporation with a suspended bridge.

7. Furthermore, aluminum nanoparticles have the potential to serve as energy materials and in nanosensing applications.

To provide a clearer structure for the thesis, the chapters are organized as follows:

Chapter 1: Introduction to Atomic Layer Deposition (ALD) Growth, encompassing both oxide materials and metals.

Chapter 2: Explanation of Superconducting Quantum Bits (Qubits) and an in-depth examination of current fabrication methods. We explore how ALD growth offers a novel approach to fabricate superconducting qubits.

Chapter 3: Detailed insights into aluminum growth using ALD, focusing on the selection of the DMEAA precursor. We clarify the importance of a conductive layer for initiating aluminum film growth, which could have implications for fabricating vertical qubits composed of Al/Al2O3/Al. We also highlight the (111) orientation of Al films through X-ray diffraction measurements.

Chapter 4: Exploration of the superconducting properties of thin aluminum films grown via ALD using DMEAA. We compare ALD growth, demonstrating that ALD provides ideal aluminum films comparable to bulk aluminum.

Chapter 5: Investigation of the ALD growth of polyhedral crystallites formed by isolated aluminum (111) nanoparticles using the DMEAA precursor. We detail the growth process, the use of the passivation agent Trimethylaluminum (TMA) as an initiator, and the methods used for characterizing the aluminum nanoparticles, including SEM, X-ray diffraction, and statistical analysis using ImageJ. Our findings reveal the formation of well-oriented aluminum nanoparticles in tetrahedral shapes with (111) orientation, which subsequently evolve into polyhedral crystallites, including octahedra.

Chapter 6: Summary and Conclusions, encapsulating the key insights presented in the previous chapters.

1. Atomic layer deposition (ALD)

1.1. Introduction

Atomic Layer Deposition (ALD) is a thin-film deposition technique that allows the growth of conformal, uniform, and precise layers of materials on substrates. ALD is often used in the semiconductor industry and is becoming increasingly popular in the production of advanced materials for various applications [1].

Compared to other growth methods such as Chemical Vapor Deposition (CVD), E-gun evaporation, and sputtering, ALD offers several unique advantages and disadvantages:

1. Growth mechanism: Precursors are consecutively added in ALD, and a self-limiting chemical reaction is included in each cycle of deposition. This makes it perfect for high-resolution applications because it enables the creation of thin films that are extremely precise, uniform, and conformal with precise thickness control. Sputtering and e-gun evaporation, in comparison, do not provide as fine a degree of control over film thickness and uniformity.

2. Material deposition: Metals, oxides, nitrides, and sulfides are wide range of various materials that can be deposited using ALD. Comparatively, e-gun evaporation and sputtering are often utilized to deposit metals and metal oxides, while CVD is for materials that can be vaporized and deposit on the substrate.

3. Temperature: ALD may work at lower temperatures than CVD, often between 100 and 300 °C. This qualifies ALD for the deposition of thin films on substrates that are sensitive to temperature, such polymers.

4. Film quality: For semiconductor applications, ALD provides high-quality films with excellent adhesion, uniformity, and purity. Sputtering and e-gun evaporation, on the other hand, might result in films with defects.

ALD is partially underlined by pulsed Chemical vapor deposition (CVD) Technology, which considers a cycle gas-solid reaction to form a very uniform structure of thin-film layer by layer on the substrate[1]. ALD could be known by different names such as atomic layer chemical vapor deposition, atomic layer epitaxy, molecular lamination, molecular layer epitaxy, molecular layering, and molecular stratification. The deposition process occurs in cycle form; each cycle consists of gas injection of precursor (A), then purge, then the same process for precursor (b) called half-reactions of ALD as shown in figure 1(b). The number of publications per year has been rapidly increasing since 1970, according to Scopus as shown in figure 1(a). It has several applications by field, mainly Material science, physics, engineering, and chemistry as shown in figure 2. The history of ALD could go back to Suntola and co-workers in 1970 in Finland, which led to commercial application. Some resources refer to the group of Professor Aleskovskii, who start published his processing in 1967. They're also a publication named "molecular layering reactions" in 1960 by Kol'tsov and co-workers.

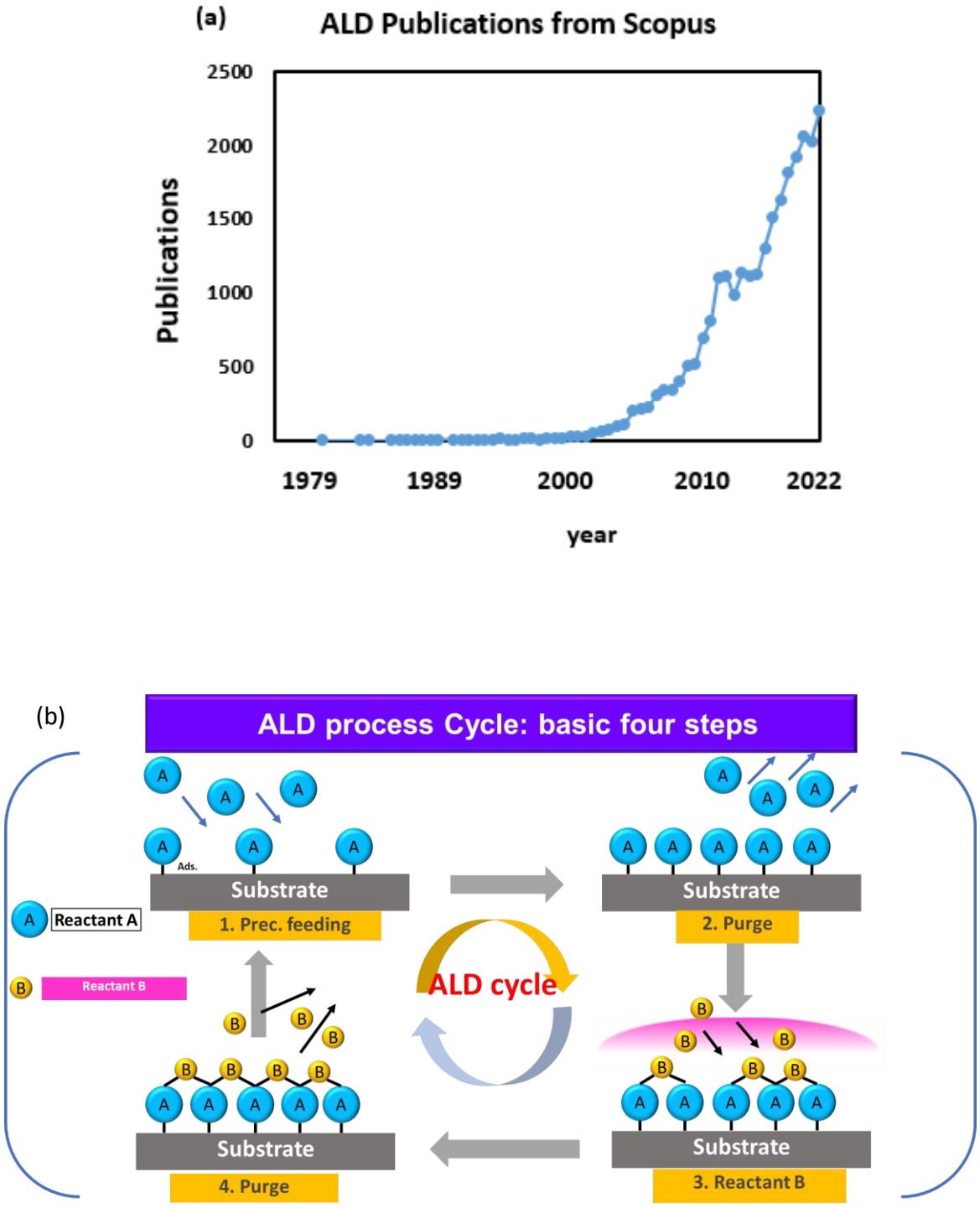

Figure 1: (a) ALD publications annually, Scopus-29551-Analyze-Year, and (b) ALD process cycle.

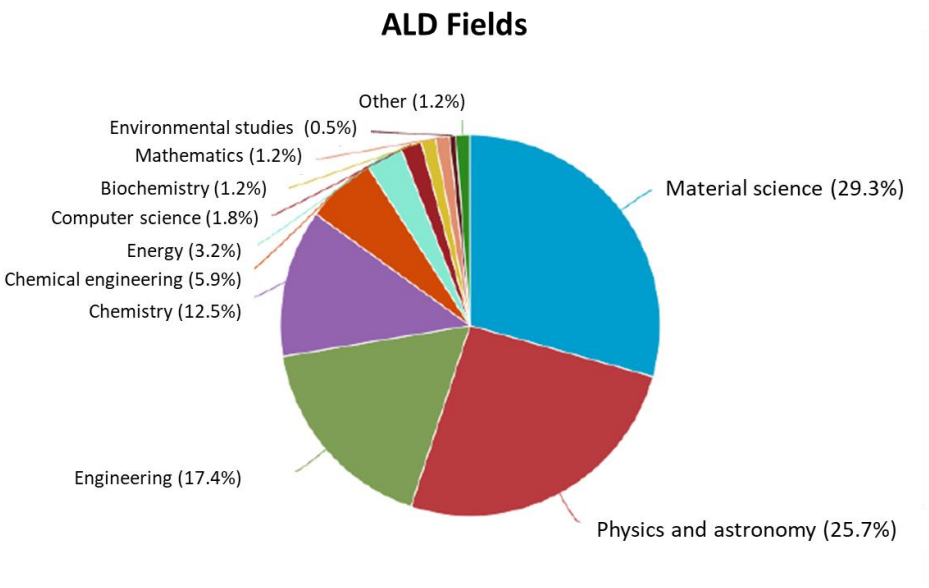

Figure 2: ALD publications cited by web of science, Clarivate.

Self-terminating behavior also depends on the windows of parameters, such as flow rate, concentration of precursors, selection of oxidants as well as growth temperature.

Trimethylaluminum (TMA) and water (H_2O) form the ideal combination for fabricating aluminum oxide through the ALD process due to the following reasons:

1- High temperature is required for TMA/H_2O reaction, that would open the door to understanding the thermal process of energy enhanced on ALD growth. Reactants are not difficult to handle, especially during energy enhancement, while another process could be unstable, and unconformity appears if reactants such as ozone or plasma discharge.

2- Oxide deposited materials are generally used for ALD, and water is often a source of material oxidation, and its vapor pressure is suitable for the process.

3- TMA is often used for ALD as an aluminum source, and its reaction applies to self-termination in the ideal reaction form. Furthermore, it is highly reactive and can produce several compound types such as Arsenides, Nitrides, oxides, and Pure Al, in addition to the gas product of methane considered inert compared to halides, and alkoxides, alkyl/silylamides, beta-diketonates which would show some difficulties to handle them.

4- TMA/H_2O is widely studied with plenty of reports and materials to be reviewed and could indirectly represent other ALD processes such as issues and phenomena, which could investigate other models after that.

5- Al_2O_3 is the ideal oxide for as the tunnel barrier of aluminum Josephson junctions.

1.2. Growth mechanism

- **Features and Characterization for ALD & TMA/H_2O Process**

Deposited Thickness grown by ALD could be down to less than a nanometer. Surface Chemistry is a curial apart of science to understand and control growth. Here will discuss General characterizations of surface chemistry after that Trimethyl Aluminum (TMA) & water reaction chemistry mechanism in particular as follows:

- **Self-terminating reactions requirement**

ALD is a chemisorption gas-solid reaction, and self-termination requires irreversible and is not allowed to reach saturated as shown in figure 3. Material Monolayer (MZ_x) of ALD is one plane of crystal unit from their growth orientation. Chemisorption (Chemical-adsorption) is the key factor to having uniform and conforming atomic layer deposition. The coverage (Q) with respect to

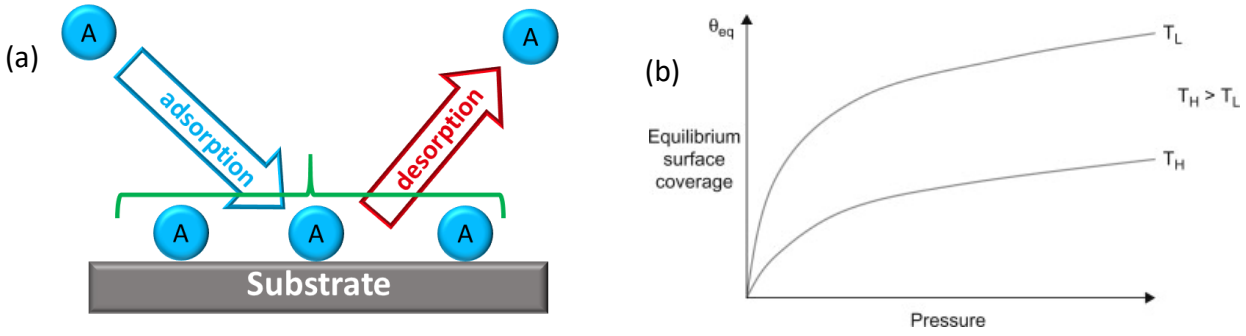

Figure 3: (a) Chemisorption reaction, and (b) coverage isotherm. Excerpt from reference [2].

time would be the difference between the adsorption rate (Ra) and desorption rate (Rd), [Coverage rate (dQ/dt) = adsorption rate (Ra)- desorption rate (Rd)].

TMA/Water self-terminated process as shown in figure 4, the deposition by cycle could be affected by the time of pluses and purges for both precursors. From each graph of figure 4, it could get the shortest time to achieve maximum deposition.

After a certain time of each step of the growth cycle, there is no change in deposition rate. Pluses (steps 1 & 3) need sufficient time to reach compilation, while a short time of purges (steps 2 & 4) would increase (growth per cycle (GPC) due to gases' existence continuously enabling deposition.

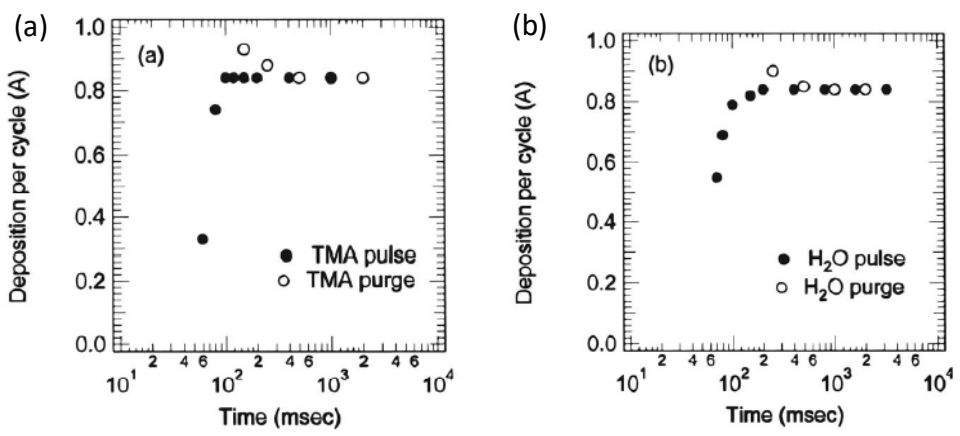

Figure 4: The deposition per cycle according to pulse and purge time of (a) TMA, and (b) water. Excerpt from the reference [3].

- **Adsorption kinetics**

This section discusses the effect of reactant concentrations and temperature as process parameters on reaction rates. Simple explanation of molecular compound A on a surface site ||* can present ALD adsorption kinetics [1].

If adsorption reaction could be considered as:

$$|| * + A_{(g)} \xrightarrow{ra} || * A, \quad \textbf{(1-1)}$$

r_a: is adsorption rate

And desorption reaction:

$$|| * A \xrightarrow{rd} || * + A_{(g)} \quad \textbf{(1-2)}$$

r_d: is the desorption rate

Adsorption rate refers to the speed at which a substance adheres to the surface of another material through the process of adsorption. Adsorption is a phenomenon where molecules or particles from a fluid (liquid or gas) adhere to the surface of a solid or liquid material.

Desorption rate refers to the speed at which molecules or particles are released from the surface of a material during the process of desorption. Desorption is the opposite of adsorption, where molecules that were previously adsorbed onto a surface are released back into the surrounding fluid (liquid or gas). There are three assumptions (idealize the other conditions) to describe the effect of pressure as follows:

1- Monolayer is the maximum amount of adsorbed species.

2- Adsorption sites on the surface are equal; they are Equivalent to each other.

3- All adsorbed spices don't interact with others.

After optimizing the conditions at condition, the coverage (Q) with respect to time(t) would be the difference between adsorption rate (r_a) and desorption rate(r_d), which would function in pressure (P). At saturation (equilibrium) conditions, the result of the equation would equal zero.

$$\frac{dQ}{dt} = r_a - r_d = k_a P(1 - Q) - k_d Q = 0, \quad \textbf{(1-3)}$$

in case of irreversible reaction k_d =zero. Then,

$$Q^{eq} = \frac{1}{1+(KP)^{-1}}, \quad \textbf{(1-4)}$$

where $K = \frac{k_a}{k_d}$, representing the Langmuir adsorption isotherm and equilibrium.

For irreversible reaction, Always Q at equilibrium equals (1) when substituting K_d with zero or K with infinity.

For reversible reaction, time would play a role as

$$Q = Q^{eq}\left(1 - e^{-(k_a P + k_d)t}\right), \quad \textbf{(1-5)}$$

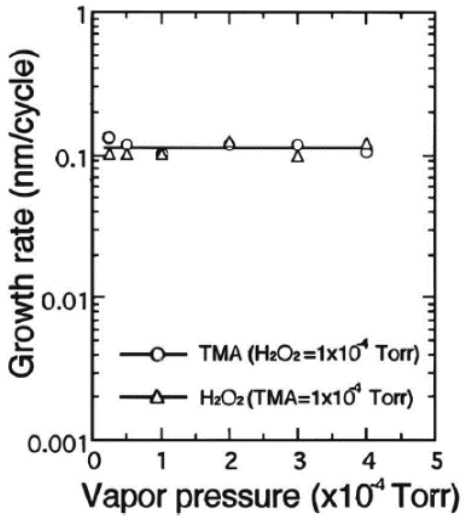

Figure 5: ALD kinetics graphs of growth per cycle vs. vapor pressure. Excerpt from the reference [4].

For the cause of TMA/Water, pressure date is missing, however, H_2O_2 instead of H_2O reaction could make Growth per cycle (GPC) independent from pressure as shown in figure 5. Nevertheless, the H_2O pressure effect and exposure time are missing.

For temperature as shown in figure 6, the effect could be concluded from the Arrhenius equation as a direct proportion, the temperature versus the reaction rate.

$$K_i = Ae^{\frac{-E_i}{RT}} \quad \textbf{(1-6)}$$

where Ki, A, Ei, R, and T represents the rate constant, a pre-exponential factor, the activation energy, the gas constant, and the absolute temperature, respectively.

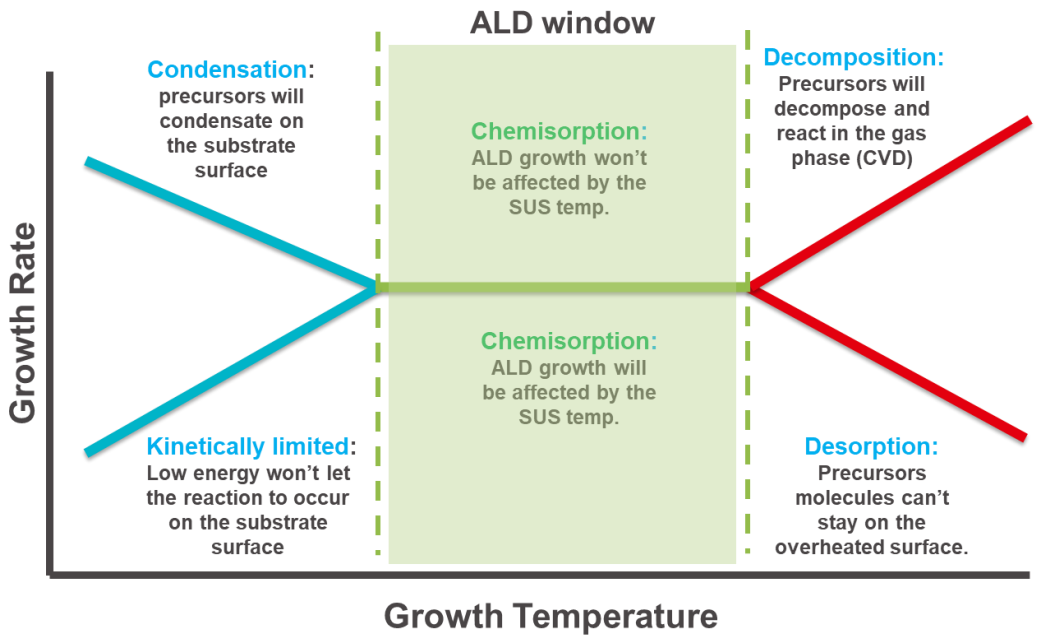

Figure 6: ALD window is proportional with temperature, ALD window in greenish zone.

GPC changes with different temperatures due to the type and number of reactive sites, following these probabilities:

- It could decrease with higher temperature due to decreasing in the number of reactive sites and due to the ratio of L/M ration of MLz species from the reaction mechanism
- It could be constant due to steric hindrance saturation on reactive surface sites. Sometimes temperature has no effect at all, or GPC has different constant values with varying temp values.
- It could increase with higher temperature due to overcoming some energy barriers of some reactions. Sometimes GPC increases first and then decreases due to the effect of reducing reactive surface sites. Figure 7 shows the growth temperature and reaction temperature of TMA/Water on GPC. For growth temperature, it has used several data from different references.

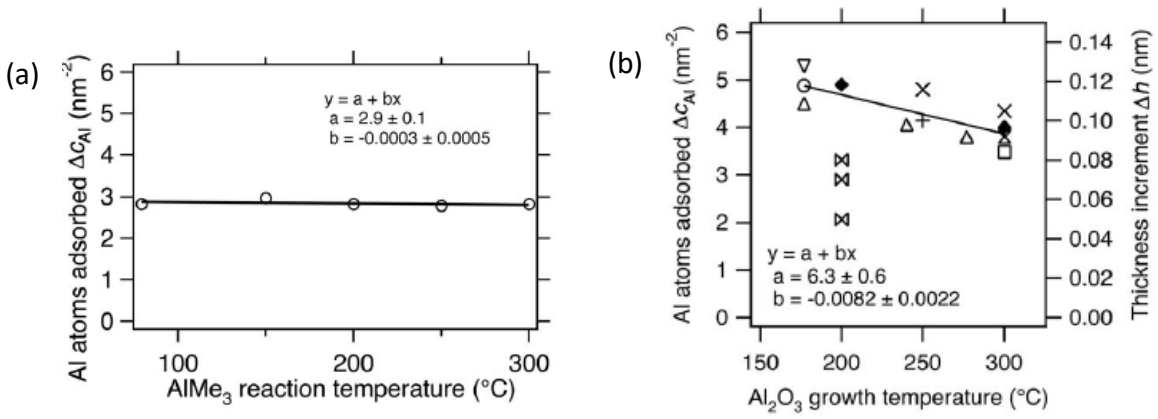

Figure 7: GPC with respect to (a) TMA reaction temperature, (b) Al_2O_3 growth temperature [1].

However, GPC was always defined as the amount of deposited Aluminum per square nanometer per cycle $\Delta C_{Al}/nm^2$, which could consider the thickness, Δh nm per cycle.

$$\Delta C_{Al} = \rho N_A M^{-1} \Delta h \qquad \textbf{(1-7)}$$

, where ρ=3.5 g/cm^{-3}

The growth temperature was defined as the steady-state process of TMA/H_2O reaction, which shows decreasing in GPC with increasing it. The maximum temperature was 300 °C could be reached as TMA would thermally decompose after it. On the other hand, Reaction temperature showed no effect on GPC.

Furthermore, Heat treatment for the Substrates such as aluminum and silica would decrease GPC due to decreasing in OH group concentration on the surface.

- **Chemisorption mechanisms**

The saturation growth of ALD surfaces involves three main chemisorption mechanisms: ligand exchange, dissociation, and association as shown in figure 8. these three mechanisms for chemisorption mechanisms are as fellow:

- Ligand exchange mechanism: where adsorbate molecules exchange some atoms or release a byproduct with the adsorbent surface molecules as a gas-solid reaction.

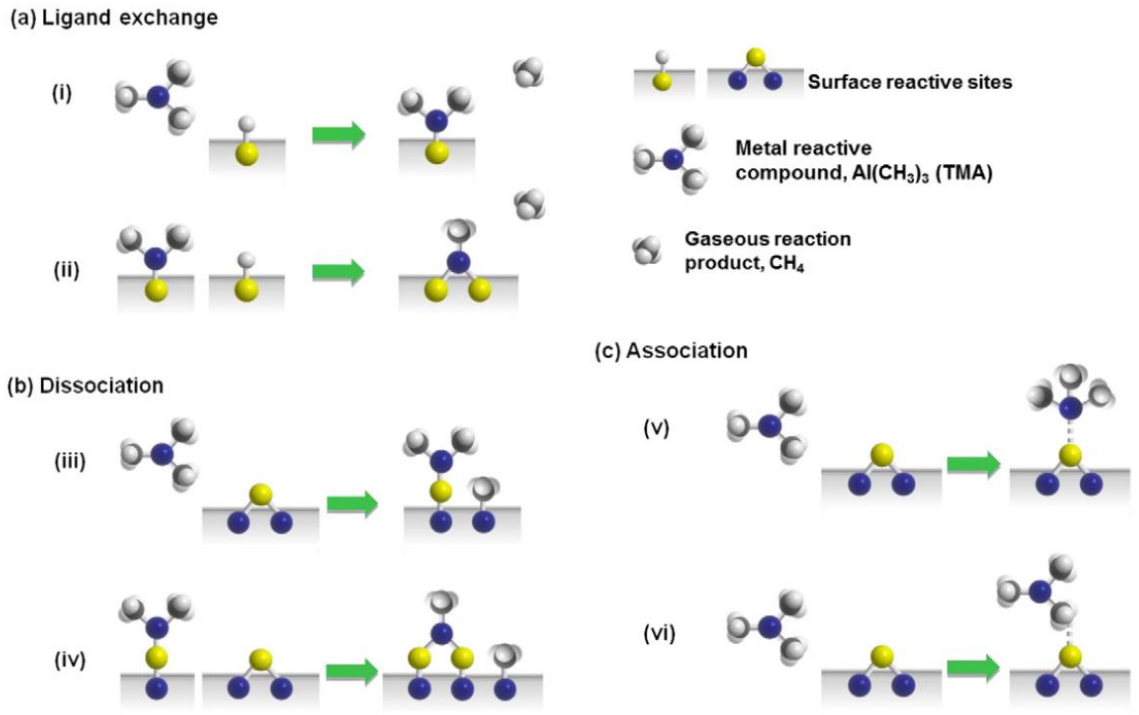

Figure 8: ALD chemisorption mechanisms of (a) ligand exchange, (b) dissociation, and (c) association. Excerpt from the reference [5].

There would be a simple mass balance equation for the reaction:

$$\Delta C_L = n\Delta C_M - \Delta C_a \quad \textbf{(1-8)}$$

where ΔCL, ΔCM, and ΔCa, are amount of ligand of metal, and of surface group reacted or ligands released, respectively.

- Dissociation mechanism: where the gas molecule is separated into two different molecules and then attached to two different reactive sites on the surface.
- Association mechanism: Where the adsorbent molecule reacts with one reactive surface site without producing a byproduct or even splitting. It considers a simple form of adsorption; one molecule attaches chemically to one site with a coordinative bond.

For TMA/Water reaction, Ligand exchange of TMA occurs with OH group surface resulting Methane CH_4^+ releasing within temperature between 80-300℃, in addition to dissociative adsorption on Silica and aluminum oxide surfaces.

- **Factors causing saturation of monolayer saturation per cycle**

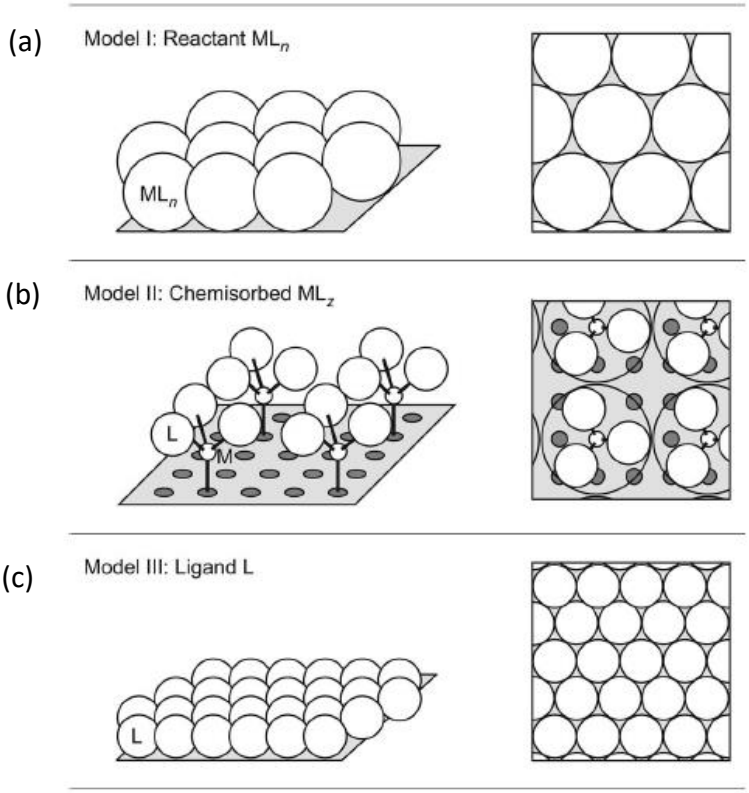

Figure 9: Models of gas-solid self-termination reaction (a) Model I MLn reactant by Ritala *et al*. Excerpt from the reference [6,7], (b) Model II Chemisorbed MLz by Ylilamm. Excerpt from the reference [8], (c) Model III ligand by Siimon. Excerpt from the reference [9]and Puurunen. Excerpt from the reference [10].

There are two main factors that affect the adsorption process of gas-solid self-termination reaction

- Steric hindrance of adsorbate molecule on surface sites
- Number of reactive sites.

Three models were developed to explain the steric hindrance effect due to the incorrect assumption of monolayer growth per cycle as shown in figure 9. All models are considered less than a monolayer per cycle.

- Model I rely mainly on adsorbent molecule size corresponding to the irreversible physisorbed monolayer to estimate maximum GPC. It calculated molecule size by knowing the density of the reactant liquid to its area covered by it. That model developed by Ritala et al. & Morozov et al. could give an approximate value of real achievable GPC.
- Model II adds the geometry shape of adsorbate into the calculation with size. That required knowing the chemical bond of different species of atoms. GPC could increase with size decreasing. Ylilammi developed that model.
- Model III Considered the number of ligands beside their sizes, that modal developed by Siimon and Aarik from one side & Puurunen from another side separately. GPC could be calculated from the amount of metal (M) adsorbate from ligands (L) divided by the L/M ratio of ML_z adsorbate.

For example, if there are spices of (MLz) as Mx-Ly So the GPC = M= L* (y/x), GPC increases with decreasing molecule adsorbent sizes. (Thickness to the area).

Steric hindrance for TMA/Water reaction, model III has applied, achieving 7.2 nm^{-2} representing 70-80 % of theoretical calculation coverage. The radius of methyl groups is 0.20 nm from the van der Waals calculation.

On the other hand, hydroxyl (OH) groups consider mainly reactive sites for TMA reactions, hence the OH group concentration control number and type of reaction species. The amount of adsorbed aluminum increases linearly with increased OH concentration while Methyl groups stay constant, hence the ratio of Me/Al decreases. Even with the absence of the OH group, there is an adsorbed amount of Al due to dissociative or associative mechanism; hence the ratio of Me/Al is three and decreases with increasing OH group.

- **GPC depended on the number of cycles**

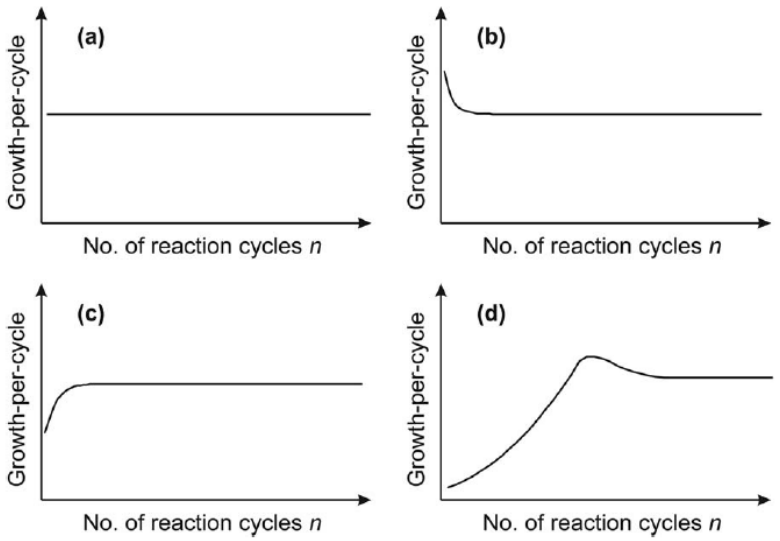

Figure 10*:* GPC relation with no of cycles, (a) constant, (b) constant after decreasing with certain cycles, (c) constant after increasing with initial certain cycles, (d) constant after increasing and decreasing of initial certain cycles. Excerpt from the reference [11].

Growth per cycle (GPC) could change when varying growth conditions. The first cycle occurs on the substrate surface, which later would be on the substrate surface and grown material, while after several cycles would be on grown material growth mode. That change of surface causes a change in GPC with respect to the number of cycles resulting in four classified growths; liner growth, substrate-enhanced growth, substrate-inhibited growth type I, and substrate-inhibited growth type II (island growth), as shown in figure 10. The difference in reactive sites between the substrate and grown material controls the growth classified group, either enhanced or inhibited.

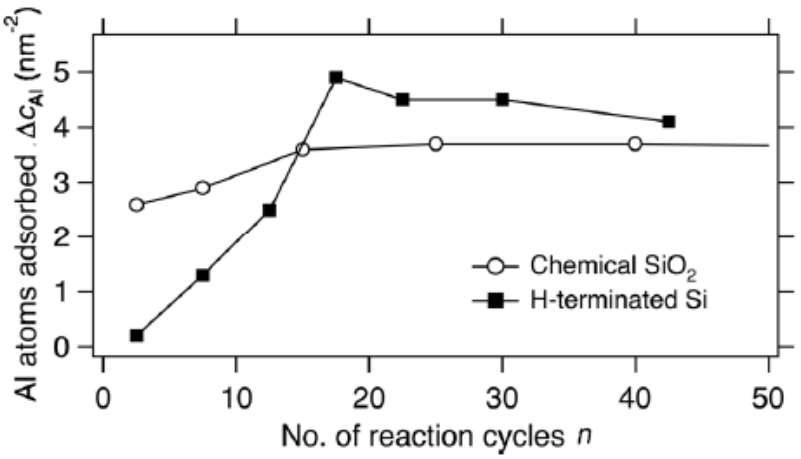

Figure 11: Aluminum atoms adsorbate Vs no of cycles with treated surface of Si-substrate. Excerpt from the reference [1].

For TMA/H_2O reaction, GPC changes due to the number of cycles and substrate type. Generally, the growth process is substrate-inhibited growth. While SiO_2 substrate shows substrate-inhibited growth type I, hydrogen-terminated silicon substrate shows substrate-inhibited growth type II as shown in figure 11. The increase in GPC is due to the increasing number of reactive sites cycle after cycle. For example, GPC increases from 3–5 nm^{-2} to 7 nm^{-2} at 300℃ on SiO_2 substrate. The defect sites on the H-terminated silicon substrate initially react with TMA causing high GPC at the beginning and bringing island growth type to appear.

- **Growth mode**

The form and shape of material growth as a part of multilayer adsorption layer after layer could be defined by the growth mode. There are several modes of growth mode as shown in figure 12 as follows:

- Island growth, or Volmer–Weber growth, is valid for several ALD processes where deposited material prefers to lay down on grown material, forming an island shape.
- Two-dimensional growth, Layer by layer growth or Frank–van der Merwe growth, is a simple way of growing fulling lower level first, then higher to higher until the full deposition process. Although it is simple, but could be existed university.
- Random deposition considers anything else different from the previous two modes. It represents equal probably to growth on all possible sites. Still, it produces smooth layers in ALD rather than in continuous deposition processes similar to the Shower model vs rain deposition model. That mode is reported for two types of ALD processes.
- Stranski–Krastanov growth mode could be described as when growth mode can be changed from one to another during growth process such like from two-dimension growth to an island or random later, on the contrary process could start island then merged to grow in two dimensions.

The relation between GPC with respect to growth modes are independent, however, it is not fully reported yet. Reported data could conclude an island growth mode connected to substrate-inhibited growth, while a two-dimensional growth mode appears related to Linear growth. Finally, island growth mode & random deposition related to Substrate-enhanced growth.

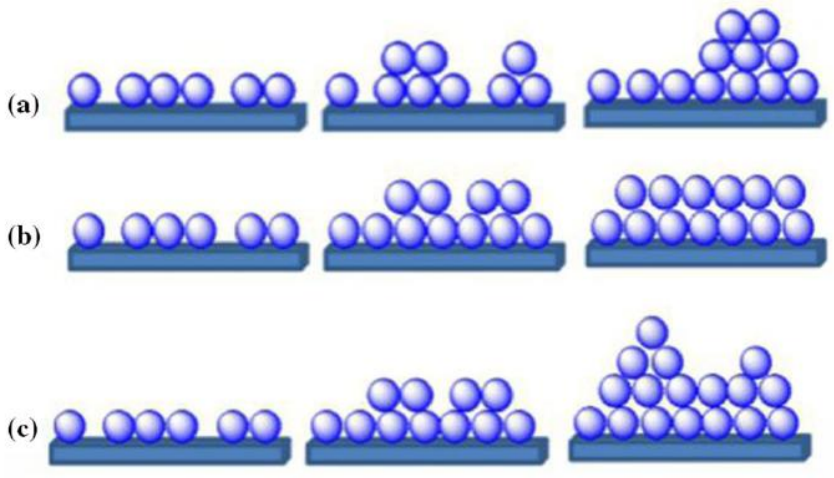

Figure 12: Growth mode (a) island growth (Volmer–Weber) mode, (b) layer-by-layer (Frank–van der Merwe) mode, and (c) mixed growth (Stranski–Krastanov) mode. Excerpt from the reference [12].

The TMA/H_2O process hasn't been reported as systematic data due to getting high dense layers that look like two-dimension growth on SiO_2 substrate, while it was Island growth on H-terminated silicon substrate. That investigation used growth-mode modeling and transmission electron microscopy.

- **Epitaxial growth**

Epitaxy considers a connection between science and art in crystal growth for circuits fabrication in optoelectronics, microelectronics, and photonics which makes controlling epitaxy capabilities essential to implementing a high-quality manufacturing [13]. The term

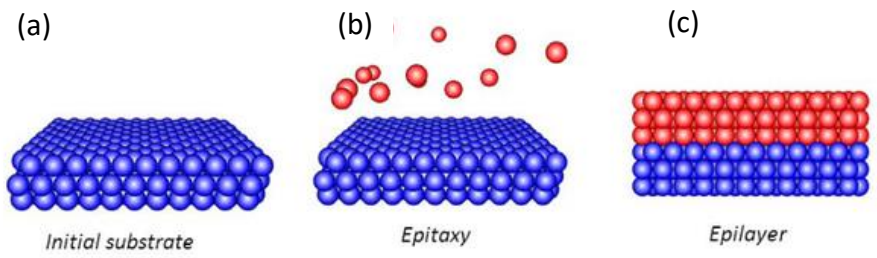

Figure 13: Illustrative epitaxy growth, (a) initial substrate, (b) epitaxy, and (c) epilayer. Excerpt from the reference [14].

"epitaxy" originates from the combination of two Greek words, "Epi" meaning "On" and "Taxos" meaning "ordering." This implies the growth on a crystal surface in an ordered manner, as depicted in figure 13, or alternatively, it refers to the crystal growth on a substrate with a preferred orientation. Modifying the growth process allows the tuning of material properties for both inorganic and organic compounds [15]. There exist narrow and broad definitions for metallic deposition and superconductivity. In superconducting materials, the grain boundary plays a crucial role in electron transfer, unlike in metals where it is less significant due to the abundance of electrons.

- **Epitaxy types:**

Topically epitaxy term refers to single-crystal film deposition on a single crystal substrate. When they (deposited film and substrate) are the same material, it is called homoepitaxy (ex; Si on Si) while called heteroepitaxy for different materials of substrate and film from each other such like (Al_2O_3 or GaAs on Si). There is required specified energy called (epitaxial

temperature) to initiate atoms and order them on the surface. Lattice Mismatch plays a significant role in the case of heteroepitaxy.

Sometimes a buffer layer could be used to decrease the effect of crystal mismatch and to control strain and defect. For example, a buffer layer of Carbon on the Si surface to grow up a 20% mismatch of SiC. Seeds on surface by depositing small amount of material, surface heating up for form oriented isolated grains could be enhancing growth orientation in low temperature as well [16,17].

CVD used to grow up the two types of epitaxies. Homoepitaxy by CVD used to deposit low doped layer on high doped substrate while heteroepitaxy used to fabricate some electronics circuits such like bipolar heterojunction transistors. The deposited material lay on substrate surface shape in alignment geometrically by minimum surface energy of it [18].

- **TMA/water kinetics:**

There are some reports for quantitative and qualitative analysis for TMA/Water process kinetics using quartz crystal microbalance (QCM) and mass spectrometry (MS) until 300 ^{o}C as shown in the figure 14, because above that temperature TMA would be decomposed [19–21]. The results show that the ligand exchange reacts faster than TMA&H2O self-termination dissociation and association reactions. It has been found that by increasing water dose would increase OH group but not methane which indicate a water reaction of association and dissociation and hence ligand exchange reaction completes much faster [19]. GPC shown increasing with increasing temperature due to increasing to adsorption rate as well as mass transfer [19].

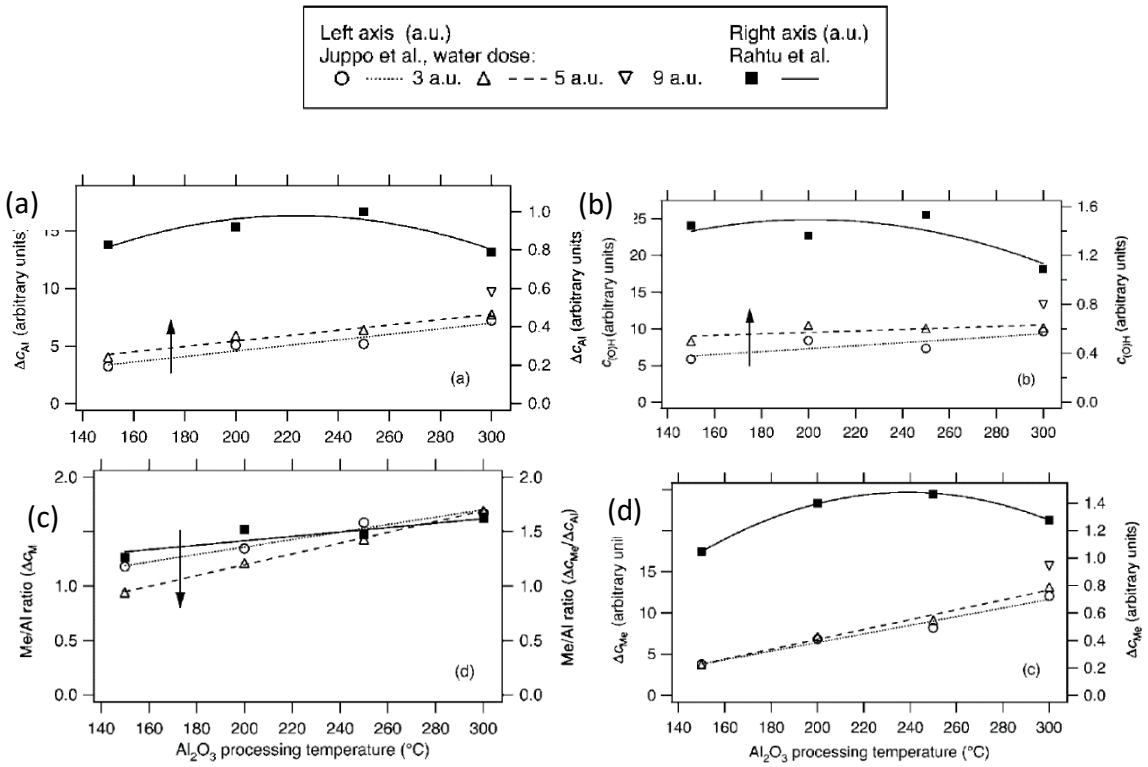

Figure 14: Surface concentration increases with temperature with respect of (a) aluminum, (b) OH groups, (c) methyl/Al ratio, and (d) methyl. Excerpt from the reference [1].

- **OH group distribution on Si substrate**

Water molecule could be adsorbed on Si surface through an attraction between the negativity of oxygen (O) atom with positivity of Si atom and the hydrogen (H) atom lays upside in inverse direction against Si surface [22], as shown in figure 15(a). Generally, surfaces could be descried to be hydrophilic or hydrophobic according to its potential tendency to adsorb or reject water molecule. More particularly there is an interaction between boundary layer between water molecule and solid surface. Water polarity nature (existence partial charge of positive and negative at water molecule) is main reason to be adsorbed and attracted by ionic surfaces.

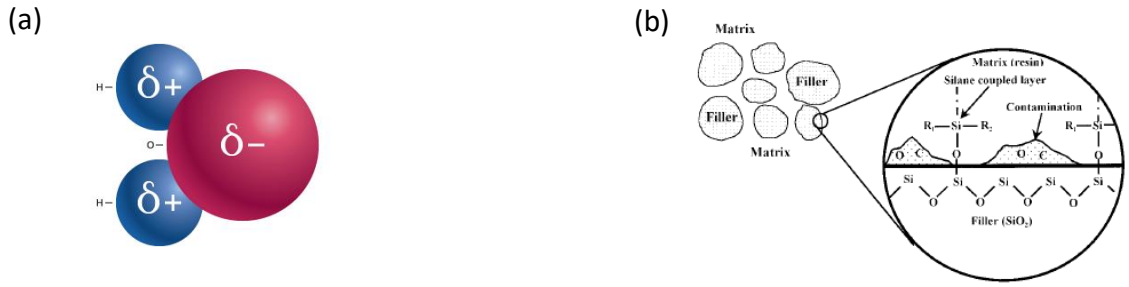

Figure 15: (a) Water molecule polarity[22], and (b) surface contaminations effects adsorption process. Excerpt from the reference [23].

Hydrophilicity and hydrophilicity term could be defined for surface according to contact angle with one water droplet; high hydrophilicity designated to be less than 30° while hydrophilicity with angle higher that 90°. Silicon contact angle is 86-88 which consider to be a hydrophobic surface [23] as shown in figure 15(b). It is most abundant element in the earth after oxygen and followed by aluminum. Some reports show ability to increase OH concentration group by cleaning pretreatment of glass and silica substrates surface by submerge for 30 minutes in one-to-one solutions of 30% H_2O_2 and 50% of H_2SO_4 then rinses it with Deionized water and methanol then drying by air. It is also recommended alternatively, to boil with 5% $Na_2S_2O_8$ (Sodium peroxydisulfate) then ultra-sonication rinse with acetone but that way could leave sodium ion contaminations [24]. Surface contaminations such like potassium, sodium and calcium effect adsorption process especially for glass substrate which has tendency to accumulate impurities during manufacturing. Although they are not bonding ions however, they cover and reduce active sites of the surface.

An immersion in a solution with 5% HCL for 4 hours following with rinsing with water overnight could dramatically decrease impurities level, while high temperature in vacuum can eliminating carbonates [23]. In addition to that, OH group concentration could be increased on silicon and silicon dioxide surfaces by using plasma [25].

- **Atomic layer deposition reactors types**

ALD is a deposition technique for monolayer thin film fabrication by highly control of growth process. ALD become recently getting more concerns for innovative nanoelectronics due to its high-performance film quality. It has several applications field such like data storage, energy harvesting, communication and sensing that make it a one of highly advanced coating system down to single nm. Pervious vapor phase deposition technique such like chemical vapor deposition and physical vapor deposition were considered for polycrystalline and amorphous, however the demand to decrease the thickness of coated thin film made the need to develop the growth control technology of ALD as well as achieving uniformity and conformity in low temperature.

ALD has advantages which hard to meet across in PVD&CVD which are flux deposition in over high temperature as explained below [26]:

- Ultra-thin and high-quality deposited film down to less nanometer.
- Deposited films are uniform where it is on large substrates such large wafers, foils or sheet materials which make its availability for industry.
- High conformity (uniformity in non-flat surfaces) on randomly roughness and corrugated surfaces topology whatever it is such like pores and trenches could unlock some new features of material functionalities without voids or pinholes as shown in figure 16.

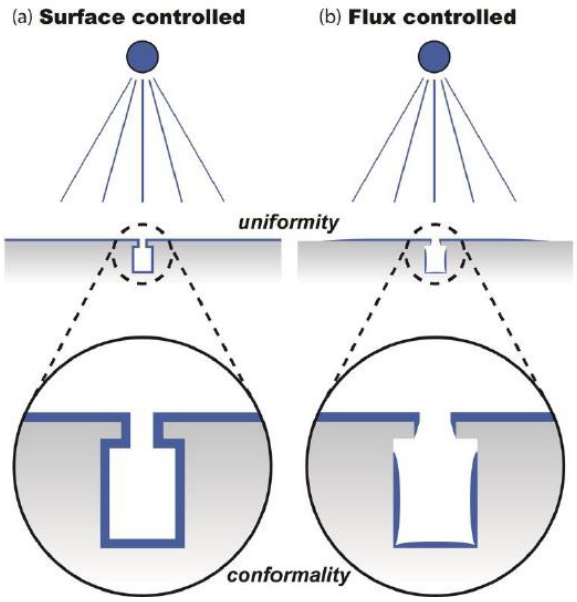

Figure 16: Conformality by (a) surface controlled, and (b) flux controlled. Excerpt from the reference [27,28].

That includes coating of different nanomaterials such like nanoparticles, nanowires and nanotubes with their applications.

- ALD doesn't required a high temperature which extend usage low temperature substrate such like polymeric and organic of flexible electronics.

Historically ALD (atomic layer deposition) derived from ALE (Atomic layer epitaxy). ALE is back from first usage to deposit a thin film of polycrystalline of ZnS on a display to make it with an electroluminescent property [27,28]. So, the main purpose was to deposit single layer from main elements (Zn & S) on crystalline and polycrystalline, however the same method also used for Amorphous thin films such like Al_2O_3 that later derived its name ALD to make it as a general term for crystal and amorphous material thin film growth. Crystal growth by ALD was limited at that time due its complexity of surface chemistry comparing with other traditional methods of metal organic vapor phase epitaxy (MOVPE) & molecular

beam epitaxy (MBE). On another hand the interest in growth amorphous material by ALD for silicon microelectronics industry make appropriate calling of ALD rather than ALE [29].

ALD has several types starting with basic flow-type reactor and alternative designs. The common basics aspects of any ALD reactor are energy supplement to elevate the substrate to desired temperature then processors pulses injection and finally the inert gas which is used for reactor purging to maintain reactor pressure that vary from ambient to 0.1-10 Torr. ALD designs are come mostly from CVD reactors, however ALD reactors, as previously mentioned in details, is not continuous process and contains precursors injection and purge steps with precise time to achieve ALD single growth per cycle. If both precursors are existed in same time, it would be continuing growth.

- **Types of reactors**

Various types of Atomic Layer Deposition (ALD) reactors are designed as shown in figure 17 to cater the different requirements and challenges in thin film deposition as following:

- Flow-type ALD reactor is similar to CVD in furnace surrounding gases flow, while the substrate lay at bottom side, the temperature arises from wall. The inert gas flow gets optimized according to reactor volume to maintain the pressure for efficient cycle.
- Showerhead ALD reactor uses a showerhead for precursor better distribution among the reactor to decrease side effect reactions. Sometimes wall reactor set to be colder than the substrate to avoid side reaction at wall that effect growth on the substrate.

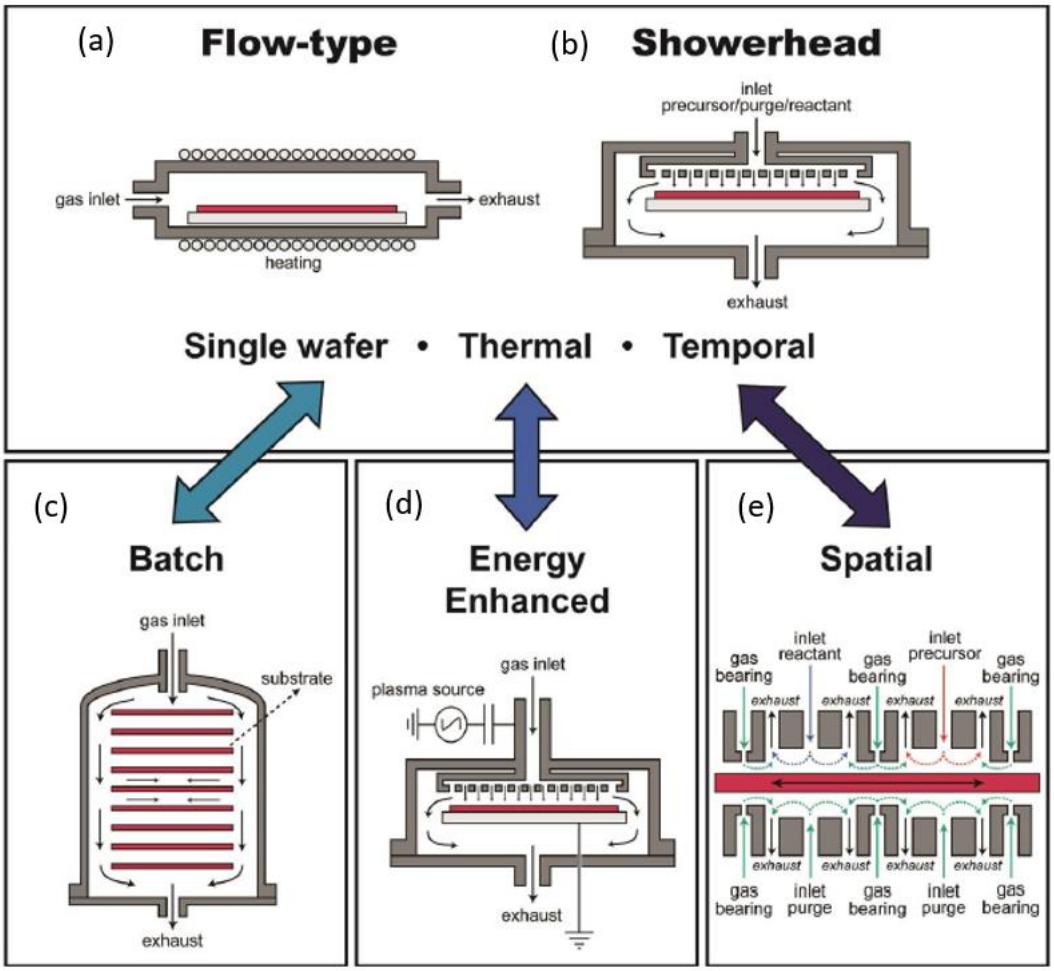

Figure 17: Types of reactors, (a) flow-type, (b) showerhead, (c) batch, and (d) energy-enhanced, (e) spatial. Excerpt from the reference [26].

- Batch ALD reactor can be used to increase the productivity which could contain many substrates (from 50 to 500) in one batch. Precursor's exposure time and purging would be longer due to slow gas diffusion in higher volume of the reactor with increment on side effect reaction which would effect on uniformity as well.
- Energy-enhanced ALD reactor is used when there is a requirement for more than one source of energy rather thermal, such like ozone or plasma discharge. It looks like a

flow-type reactor with an integration system such like a plasma generator set closely to the substrate [30] or an inlet close to substrate in case of ozone [31].

- Spatial ALD reactor idea is to separate the cycle step in spatial domain instead of time domain. In another word all steps are existed in same time but in different position place inside the reactor with purging zones between each step. That process could be implemented by moving the substrate or deposition head itself which would extend the technical specifications and reactor productivity regardless dimensions, substrates amount and surface kinetics. It is suitable reactor to produce high deposition rate with same film quality of ideally short time half reactions (~milliseconds).

- **(2D & 3D) nomination and growth theories**

The better understanding the material behavior growth, the faster we can control their properties. The dimension account (ex: 0D, 1D, 2D or 3D) of nanomaterial relies on the nano scale (less than 100 nm) of each dimension; it decreases with decrease the size into nano, or from another words, **dimension is disappeared** when getting smaller [32], as shown in figure 18. It is the number of dimensions which electrons are not confined and energy levels increase in their discreteness. So according to that; nanoparticles all dimensions are in nano-scale so they called zero-dimension (0D) material. Nanowires and nanotubes could be become one-dimension (1D). Nano sheet or thin films are two dimensions (2D) due to existence of two dimensions not in Nano scale sized.

The last description of three dimensions (3D) is called in bulk material and in this class, material is no more could describe as Nano material in size, however could be Nano material if they showed one of Nano size properties. 2D nanomaterials could be existed in form of

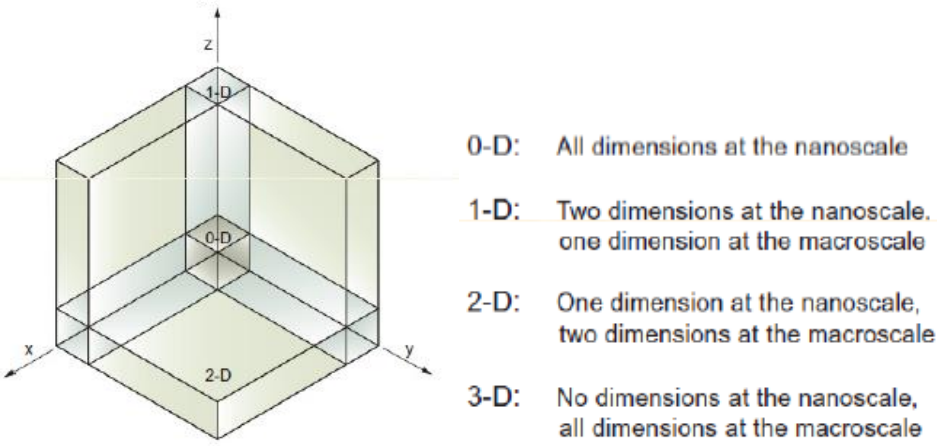

Figure 18: A dimension is disappeared when getting smaller. Excerpt from the reference [32].

Amorphous or crystalline structure from one or several types of chemical compositions. A single layer of thin film up to more layer could be deposited on substrate from metal, oxide or another element. Conducted electron(s), in case of 2D nanomaterial, would delocalize a long wide of thin film plane and coexisted with confinement across the thickness with following equation;

$$E_n = \left[\frac{\pi^2 \hbar^2}{2mL^2}\right](n_x^2) \qquad \textbf{(1-9)}$$

, where E_n is an energy level of n,

n_x, quantum number in the three dimensions x, y, and z

Where; m is the mass of the electron L: is the width (confinement) of the infinitely deep potential well

$\hbar = h/2\pi$, h is Planck's constant.

From pervious equation shows the smaller dimension, wider separation between energy levels.

- **Nucleation and growth theories**

Particle formation has theories such like density functional theory (DFT) or classical nucleation theory (CNT). They also applicable for nature systems like snow, rain, clouds and stone formation. Nucleation starts when the phase transforming by crossing the boundaries to stable solid state phase. The first irreversible formation of nucleus starts to grow then.

a. Classical nucleation theory (CNT)

It is a phenomenological approach rely on thermodynamics of macroscopic properties like surface tension and density to calculate the free energy to form a small cluster. The driving force to form a heterogeneous from a homogeneous system could be calculated from interface affinity (φ) [33]

$$\Phi = -\frac{\Delta G}{\Delta n} \quad \textbf{(1-10)}$$

, where; ΔG: Gibes free energy and Δn: number of unstable nucleus sites.

When Φ> zero, the nucleation starts spontaneously while less won't start and zero consider equilibrium

While the energy cost of transformation,

$$\Delta G_{surface} = \sigma \cdot A \quad \textbf{(1-11)}$$

Where σ: surface tension, A: area

After that, there were a lot of modifications to consider various factors such like translational and rotational degrees of freedom [34] or a partial pressure of the cluster [35], curvature dependence of σ [36].

b. Density functional theory (DFT)

It has a microscopic approach. The first calculation was by cahn& hillard [37] in following form:

$$\Omega[\rho(r)] = \int dr\{f_h[\rho(r)] - \mu\rho(r) + K[\nabla\rho(r)]1^2\} \quad \textbf{(1-12)}$$

, where μ is chemical potential, ρ(r) an average density, fh a free energy per volume of a homogeneous system. $K[\nabla \rho(r)]^2$ represents a nonlocal contribution to fh.

It describes inhomogeneous structure of nucleating system by getting the average of density at specific temperature of thermodynamic states. DFT mainly use for modelling and simulation of nucleation.

c. van der Waals contact:

The nucleation growth in 2D in ultra-thin of monolayer or 3D material relies mainly on the migration rate of precursor molecule due to van der waals contact between interface of surface and gaseous molecules where substrate surface effect their diffusion and migration coefficient (D) as following:

$$D \approx D_\infty \exp(-U/K_B) \quad \textbf{(1-13)}$$

Where U is energy barrier (U) for surface diffusion,

T is the temperature and K_B is the Boltzmann constant.

When the surface is smooth that expect small energy barrier and higher migration rate and atoms diffusion resulting in 2D thin film formation. If the surface dominates high surface energy film tend to accumulate above each other resulting thinker film with island growth. The SiO2/Si substrates contains dangling bond which increase much surface energy of substrate so Surface dangling bond- free substrate of bare Si is recommended to eliminate

the effect of those bonds and hence better thin film in 2D formation as substrate surface energy is essential to grow Confront and uniform thin films[38,39].

d. Arrhenius equation:

It gives the dependence of the rate constant of a chemical reaction on the absolute temperature, a pre-exponential factor and other constants of the reaction from equation (1-6). The equation has been explained at section of equation (1-6)

1.3. Various precursors

ALD involves the sequential exposures a substrate by alternating precursor gases in a controlled environment.

Here are some precursors commonly used in ALD processes:

- **Metal precursors**

TMA (Trimethylaluminum): Used for depositing aluminum oxide (Al_2O_3) films.

TDMAT (Tetrakis(dimethylamido)titanium): Used for depositing titanium dioxide (TiO_2) films.

TDMAH (Tetramethylammonium hydride): Used for depositing cobalt and nickel films.

Cp_2Mg (Cyclopentadienylmagnesium): Used for depositing magnesium oxide (MgO) films.

- **Metal halide precursors**

TDMAT (Tetrakis(dimethylamido)titanium): Also used as a titanium precursor.

TDEAT (Tetrakis(diethylamino)titanium): Used for depositing titanium nitride (TiN) films.

DEZ (Diethylzinc): Used for depositing zinc oxide (ZnO) films.

$HfCl_4$ (Hafnium (IV) chloride): Used for depositing hafnium oxide (HfO_2) films. As it is solid and required to heat up adding up difficulty to be controlled, it not used anymore.

Metal halide precursors are less commonly used in ALD for safety reasons.

- **Oxygen precursors**

Water (H_2O): Used as an oxygen source for metal oxides.

ozone (O_3): Provides oxygen radicals for some ALD processes.

- **Nitrogen precursors**

NH_3 (Ammonia): Used for depositing nitrides like gallium nitride (GaN) and titanium nitride (TiN).

DEZ (Diethylzinc): Can also be used for nitrogen-doped films.

- **Organic precursors**

DEZ (Diethylzinc): Can be used for carbon-doped films.

TMA (Trimethylaluminum): Can be used for carbon-doped films.

DEZn (Diethylzinc): Used for depositing zinc oxide films with organic components.

- **Silicon precursors**

SiH_4 (Silane): Used for depositing silicon films.

Si_2H_6 (Disilane): Used for depositing silicon films. Both pervious precursors are old which widely used in the past due to not being liquid.

TBAS (Tert-butyldimethylsilylamine): Used for depositing silicon nitride (Si_3N_4) films.

Trisilane (Si_3H_8): It may offer distinct advantages in terms of film quality and properties.

Tris(dimethylamino)silane (TDMAS): it used in some ALD processes, particularly for silicon nitride films.

- **Phosphorus precursors**

TBP (Tri-n-butylphosphine): Used for depositing phosphorus-doped films.

- **Sulfur precursors**

H_2S (Hydrogen sulfide): Used for depositing metal sulfide films.

It's important to note that the choice of precursors depends on the specific material and film properties desired in the deposition process. Different combinations of precursors allow for the deposition of a wide range of materials with varying compositions, properties, and applications.

1.4. Surface treatment of the substrate

Surface treatment of a substrate refers to the process of modifying the surface properties of a material to achieve specific desired characteristics.[40–43] This treatment can involve various methods and techniques aimed at altering the surface's chemical, physical, or mechanical properties. The goal of surface treatment is often to enhance adhesion, corrosion

resistance, wear resistance, lubrication, appearance, or other functional properties of the substrate. Common methods of surface treatment include: cleaning, chemical Treatment, coating and plating, thermal treatment, surface modification techniques, surface texturing

- **Cleaning process**

This is the basic step in many surfaces' treatment processes. Removing contaminants such as dirt, grease, oils, and oxides from the surface is essential to ensure proper adhesion and effectiveness of subsequent treatments.

- **Chemical treatment**

Chemical processes include methods like etching, passivation, anodizing, and chemical conversion coatings. These processes alter the surface chemistry, creating protective layers or enhancing adhesion.

- **Coating and plating**

Applying coatings like paints, varnishes, polymers, or metal plating (electroplating) can provide protection, improved appearance, and unique properties.

- **Thermal treatment**

Heat treatment processes like annealing, case hardening, and tempering can alter the material's microstructure and thus its mechanical properties.

- **Surface modification techniques**

Techniques like ion implantation, laser surface modification, and plasma treatment can change the surface composition and structure, imparting specific properties.

- **Surface texturing**

Creating micro or nano-scale patterns on the surface can modify its wetting characteristics, friction, and other properties. The choice of surface treatment method depends on the substrate material, desired properties, and intended application.

1.5. Properties of ALD thin films

-Advantages of ALD and differences from CVD

There are some crucial differences between atomic layer deposition (ALD) and Chemical vapor deposition (CVD) as shown in table 1; CVD is a continuous mixed vapors phase reaction causing in continuously growing of thin-film. In contrast, ALD gases injection occurs separately for each gas, including a purge step which causes a controllable growth of one single layer of deposited material without being dependent on the gas flow. Furthermore, ALD grows films in high level of uniformity with complete conformity as a result of atomic-level control as shown in figure 19, which has great ability for surfaces coating of top and sides walls [44,45]. ALD growth mechanism has a unique advantage of not requiring

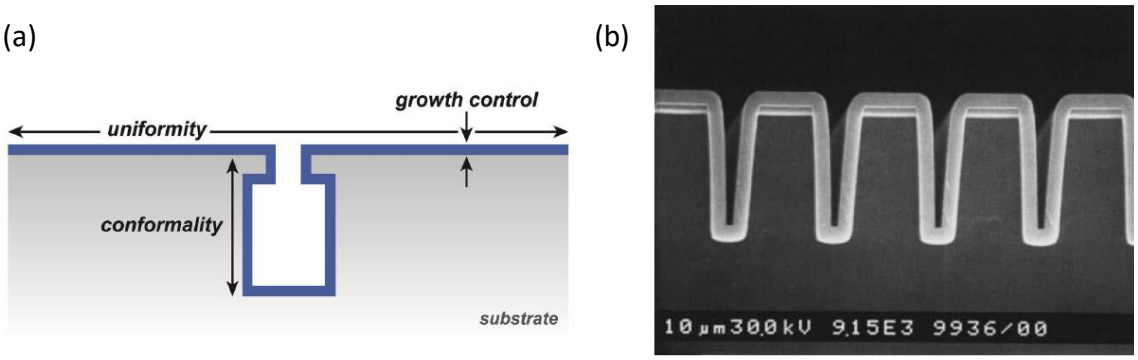

Figure 19: (a) Illustrative conformal and uniform growth of ALD, and (b) cross-sectional SEM image of an Al_2O_3 ALD film with a thickness of 300 nm on a Si wafer with a trench structure, the film follows the trench structure conformally. Excerpt from the reference [46].

nucleation as an initiation, on contrary to CVD and other deposition technique, grown thin films doesn't have pinholes and are stress-free. Nucleation is the main reason for grains growth which later grows together into a thicker film of 50 -100 Å with a lot of pinholes and stresses, indicating a non-ideal grain boundary limiting its application to higher than 500 nm, While ALD thin films could reach to less than 1 nm which extend to more application for better performance [47–49]. The ALD grow film with advantages of being robustly controlled, very thin layer by layer growth per cycle (GPC), independency from gas flow distribution, and free from pinholes and stresses, makes it preferable from CVD and other deposition techniques.

Table 1: Comparisons table of main process properties between ALD and CVD.

	Atomic layer deposition process	Chemical vapor deposition process
Film thickness and growth mode	Ultra-thin film layer by layer. It could be 1 nm or less in a discrete deposition	Several nms in a continuous deposition
Gas injection	Separately One by one, including a purge per each of them	Gases get mixed together into the same chamber
Temperature	Relatively Low temperature (80-300)℃ (Amorphous films)	High temperature 700℃ or more for (single crystal hetero structured) &migration
Growth initiation	Adsorption and not required Nucleation	Nucleation followed by grain growth
Film uniformity and conformity	High	Less than ALD
Thickness control	Control the number of cycles	Reaction rate time
Film properties	Insignificant stress without pinholes	Stresses with a dislocation (Due to high deposition rate and lattice mismatch)

Precursors	Shouldn't decompose thermally during the process	Decomposition is required during the process
Reaction	The gas-solid reaction on the substrate surface	the gas- gas reaction in the gas phase

1.6. Conclusions

Atomic Layer Deposition (ALD) is a powerful thin-film deposition technique that offers unique advantages over other growth methods as it allows for the growth of conformal, uniform, and precise layers of materials on substrates with excellent film quality, making it ideal for high-resolution applications in the semiconductor industry and other fields. ALD's growth mechanism, which involves consecutive addition of precursors in self-limiting chemical reactions, enables precise control over film thickness and uniformity. This sets ALD apart from other methods that may not provide the same level of control. ALD also allows for the deposition of a wide range of materials, including metals, oxides, nitrides, and sulfides, making it versatile for various applications. Another advantage of ALD is its ability to work at lower temperatures compared to CVD, making it suitable for deposition on temperature-sensitive substrates such as polymers. ALD films also exhibit high-quality characteristics such as excellent adhesion, uniformity, and purity, making them ideal for semiconductor applications. The history of ALD dates back to the 1970s, and it has rapidly gained popularity with increasing publication numbers and applications in fields such as material science, physics, engineering, and chemistry. Trimethylaluminum (TMA) and water (H_2O) are often used as precursors in ALD for fabricating aluminum oxide, and they offer

several advantages such as ease of handling, high reactivity, and ideal self-terminating behavior. Furthermore, TMA/H_2O has been widely studied, providing a wealth of literature that can be used to investigate other ALD processes and phenomena. Overall, ALD is a promising thin-film deposition technique with unique advantages and is expected to continue playing a significant role in the production of advanced materials for various applications in the future.

Surface chemistry plays a crucial role in understanding and controlling the growth of deposited thickness in ALD, which can be as thin as less than a nanometer. Self-termination is an important requirement for optimal ALD growth, where the gas-solid reactions should be irreversible and not allowed to reach saturation. The material monolayer (MZx) of ALD grows in a specific crystal unit orientation. The kinetics of adsorption and desorption reactions also affect ALD growth. The coverage (Q) of adsorbed species on the surface depends on the adsorption rate (r_a) and desorption rate (r_d), which are influenced by parameters such as pressure and temperature. Langmuir isotherm can be used to describe the equilibrium coverage (Q^{eq}) at saturation, where the ratio of adsorption rate constant (ka) to desorption rate constant (k_d) plays a role. Irreversible reactions result in Q^{eq} equal to 1, while reversible reactions depend on time. Temperature also affects ALD growth, where the reaction rate is directly proportional to temperature according to the Arrhenius equation. The growth per cycle (GPC) may decrease, remain constant, or increase with temperature, depending on the type and number of reactive sites and energy barriers of reactions. Heat treatment of substrates can also affect GPC. In the case of TMA/Water reaction, pressure data is missing, but the use of H_2O_2 instead of H_2O can make GPC independent from pressure. However, the effect of H_2O pressure and exposure time is not discussed. Growth temperature

has a significant effect on GPC, where increasing temperature decreases GPC due to thermal decomposition of TMA, and reaction temperature has no effect on GPC. Heat treatment of substrates can also decrease GPC by reducing surface OH group concentration. Understanding the surface chemistry and kinetics of ALD reactions, including self-termination, adsorption, desorption, and the effect of temperature and pressure, is crucial for controlling and optimizing the growth of deposited thickness in ALD processes. Further research and experimentation are needed to fully understand and manipulate these factors for precise ALD growth in various applications.

Chemisorption mechanisms play a crucial role in the gas-solid adsorption process, and three main mechanisms have been identified: ligand exchange, dissociation, and association. Ligand exchange involves the exchange of atoms between the adsorbate and the adsorbent surface molecules, resulting in the release of byproducts. Dissociation mechanism involves the gas molecule being separated into two different molecules and attached to different reactive sites on the surface. Association mechanism involves the adsorbent molecule reacting with a surface site without producing any byproducts. The saturation of monolayer per cycle in gas-solid self-termination reactions is influenced by two main factors: steric hindrance of the adsorbate molecule on surface sites and the number of reactive sites. Three models have been developed to explain the steric hindrance effect, taking into account factors such as molecule size, geometry, and ligand concentration. Growth per cycle (GPC) is dependent on the number of cycles, and it can change with different growth conditions, resulting in different growth modes such as linear growth, substrate-enhanced growth, and substrate-inhibited growth types I and II (island growth). For the TMA/Water reaction, ligand exchange of TMA occurs with the surface OH groups, resulting in the release of methane

(CH_4) as a byproduct. Dissociative adsorption on silica and aluminum oxide surfaces also occurs. The steric hindrance effect is accounted for by model III, which considers the number and size of ligands. GPC increases with decreasing molecule adsorbent size. The concentration and type of reactive sites, specifically the OH groups, also affect the adsorption process, with increasing OH group concentration resulting in a linear increase in adsorbed aluminum and a decrease in the Me/Al ratio. GPC is also influenced by the number of cycles and substrate type, with substrate-inhibited growth being the dominant mode for TMA/Water reaction, and GPC increasing with the number of cycles and the type of substrate used. Understanding the chemisorption mechanisms and factors affecting the saturation of monolayer per cycle is essential in optimizing gas-solid adsorption processes for various applications. Further research and modeling can help in developing more accurate predictions and strategies for controlling the adsorption process to achieve desired outcomes.

(ALD) has several advantages over other deposition techniques as allows for the growth of thin films with high uniformity and conformity due to atomic-level control, resulting in films without pinholes and stresses. ALD also does not require nucleation as an initiation step, unlike some other techniques, which can lead to non-ideal grain boundaries and limitations in film thickness. In contrast, ALD can achieve film thicknesses of less than 1 nm, extending its applicability to a wider range of applications. ALD also offers robust control, layer-by-layer growth per cycle, and independence from gas flow distribution, making it a preferred choice for many applications. Epitaxy, which involves the growth of single-crystal films on a substrate, is an important process in optoelectronics, microelectronics, and photonics, and ALD can be used for homoepitaxy and heteroepitaxy. However, ALD offers advantages such as precise control of film properties, low stress, and the ability to grow ultra-thin films layer

by layer, making it a promising technique for epitaxial growth. Overall, ALD has unique advantages and differences compared to CVD, making it a valuable technique for thin film deposition and epitaxy in various applications.

ALD reactors come in various types, each with its own advantages and disadvantages. Flow-type ALD reactors are similar to CVD in terms of gas flow, with the substrate located at the bottom and temperature arising from the walls. Showerhead ALD reactors use a showerhead for better precursor distribution to decrease side reactions. Batch ALD reactors can increase productivity by containing multiple substrates in one batch, but may have longer exposure times and increased side effects due to slow gas diffusion in a higher volume reactor. Energy-enhanced ALD reactors use additional sources of energy, such as ozone or plasma, to enhance the deposition process. Spatial ALD reactors separate the cycle steps in space rather than time, allowing for higher deposition rates and increased productivity. Nanomaterials can be classified based on their dimensions, with nanoparticles considered zero-dimensional (0D) materials, nanowires and nanotubes considered one-dimensional (1D) materials, thin films or nano sheets considered two-dimensional (2D) materials, and bulk materials considered three-dimensional (3D) materials. Growth theories such as classical nucleation theory and density functional theory (DFT) are used to understand the nucleation and growth of particles, with CNT being a phenomenological approach based on thermodynamics and DFT being a microscopic approach based on the average density and free energy of the nucleating system. Both theories have been modified to consider various factors and provide insights into the growth behavior of nanomaterials.

2. Superconducting quantum bit (qubit)

2.1. Properties of superconducting materials

Superconducting materials exhibit a unique set of properties when they are cooled below a critical temperature (T_c). Below this critical temperature, the material's electrical resistance drops to zero, allowing for the flow of electrical current without any energy loss.

The properties of superconducting materials can be listed as fellow:

- **Zero electrical resistance**

One of the defining characteristics of superconductors is their complete lack of electrical resistance below the critical temperature (T_c). This means that current can flow through these materials without any loss of energy due to resistance.

- **Critical temperature (T_c)**

Superconductivity occurs only at temperatures below a critical temperature (T_c). Different superconducting materials have different critical temperatures, ranging from a few Kelvin (-273.15 °C) to higher temperatures that are closer to room temperature in some newer materials.

- **Meissner effect**

When a superconductor transitions to its superconducting state, it expels magnetic fields from its interior. This is known as the Meissner effect, and it causes the superconductor to exhibit perfect diamagnetism. This effect is responsible for the levitation of superconductors above magnets.

- **Perfect diamagnetism**

Superconductors are perfect diamagnets, meaning they repel external magnetic fields, and it can lead to interesting applications like levitation and magnetic shielding.

- **Critical magnetic field (H_c)**

Above a certain magnetic field strength, superconductivity is destroyed. The critical magnetic field (H_c) represents the maximum magnetic field that a superconducting material can tolerate while maintaining its superconducting state.

- **Critical current density (J_c)**

Superconducting materials can carry electrical current without resistance, up to a certain current density. Beyond this critical current density, the superconducting state breaks down. J_c is an important parameter for assessing the practical usability of superconducting materials in various applications, particularly in superconducting wires and cables.

- **Isotope effect**

The critical temperature of a superconducting material can be influenced by the isotopic composition of the elements within the material. Substituting isotopes with different masses can affect the electron-phonon interactions responsible for superconductivity.

- **Type I and type II superconductors**

Superconductors are often classified into two types based on their behavior in the presence of an applied magnetic field. Type I superconductors expel all magnetic flux when cooled below their critical temperature. Type II superconductors can tolerate a certain amount of magnetic flux by forming quantized vortices.

- **Coherence length**

In superconductors, coherence length is a fundamental parameter that characterizes the spatial extent over which the superconducting state is coherent. For example, high-T_c materials are robust at low temperature with a very short coherent length.

- **Energy gap**

Superconducting materials have an energy gap between the condensate state where Cooper pairs exist and the excited states where quasiparticles. The superconducting energy gap corresponds to the energy to break up a Cooper pair.

- **Flux pinning**

In type II superconductors, vortices can become "pinned" by defects or impurities in the material. This phenomenon can enhance the critical current density and stability of the superconducting state.

Superconducting materials have a wide range of applications, including in high-field magnets, energy transmission, medical imaging (MRI), particle accelerators, quantum computing, and more.

2.2. Physical system of superconducting qubit

- **Quantum circuits**

Quantum bit (qbit, qubit) can be realized in any systems where two well-defined quantum states exist, such as photons, ions, trapped atoms, quantum dots, and superconducting circuits [50].

Flux qubit is composed of three JJs in a loop and charge qubit is composed of two JJ in series. Fluxon is a transmission line with JJs. [51];

1. linear (superposition ability) inductor of superconducting
2. Capacitors with Josephson junction.
3. Nonlinear Inductor of Josephson tunnel junction. (Inharmonic energy level)

Quantum circuits is not intuitive even if they are outcome from electromagnetic circuits which uses Kirchhoff and Maxwell equations as resulting of several GHz of long (Centimeters) wavelengths of superconducting qubit frequency comparing to big circuits size of submillimeter size. In electrical circuit the size much bigger which make it intuitive. Based on pervious, there is a non-conversion relation between currents and charges called quantum electrodynamics in 1950 [52], however macroscopic quantum tunneling (MQT) observed later on in 1981 through from Josephson junction [53].Quantum effect didn't appear in conventional electrical circuits consisting of normal metal and semiconducting opposing possibility expectation, although its availability in high frequencies of THz with of subcooled to milli-kelvin temperature, due to the dissipation effect during widening the energy levels which destroys the quantum coherence [54]. It could be avoided through high quality factor of resonators of LC circuits but still relying on Ehrenfest theorem (linear oscillators are same in classical and quantum dynamics) [55]. So, it is required a nonlinear nondissipative elements circuit to observe quantum dynamics which could be through Josephson tunneling of nonlinear inductance [56].

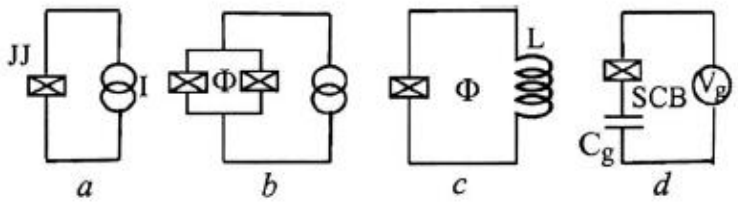

Figure 20: Basic superconducting circuit of qubit, (a) dc SQUID, (b) rf SQUID, (c) single Cooper box, and (d) the crossed box of Josephson tunneling element. Excerpt from the reference [57].

Hamilton form is the basis for qbit quantum description. In classical dynamics the variables are equal to Kirchhoff standards ($\Sigma I_n=0$), while Hamiltonian circuit building blocks are kinetic energy of capacitive elements charges ($K=0.5CV^2$), potential energy of Josephson inductance:

$$U_J = -E_J \cos\varphi \qquad \textbf{(2-1)}$$

and superconducting leads inductance [58–60]

$$U_L = \frac{0.5\varphi^2}{L} \qquad \textbf{(2-2)}$$

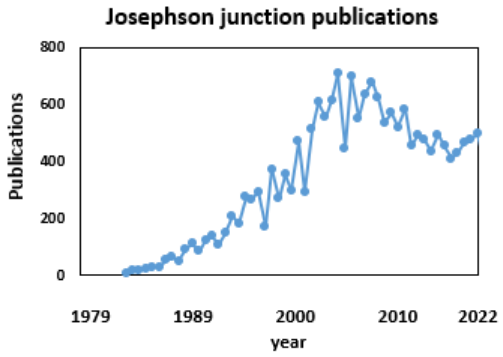

Figure 21: Josephson junction publications trend analysis by [Scopus-1838-Analyze-Year of Josephson junction].

Phase difference φ obviously could be expressed in Hamiltonian energy difference for a given element which would represent Josephson relation of voltage drop:

$$V = (\hbar/2e)\,\varphi \qquad \textbf{(2-3)}$$

and magnetic flux:

$$V = (\hbar/2e)^2\,\varphi \qquad \textbf{(2-4)}$$

Hamiltonian could be considered energy at very specific region.

Inductance-capacitor circuit (LC) as shown in figure 22, has harmonic energy level, so by replacing inductance with jj, we can get inharmonic energy level.

$$H = E_C + E_J. \qquad \textbf{(2-5)}$$

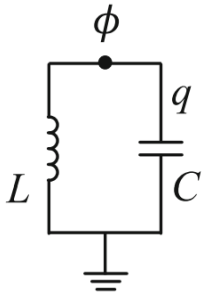

Figure 22: LC circuit. Excerpt from the reference [61].

- **Josephson junction**

Josephson junctions, as depicted in figure 21, play a crucial role in the structure of quantum bits. The trendy publication shown in figure 23(a) provides promising evidence for their potential to replace conventional bit circuits and establish quantum computers, which are also gaining popularity, as shown in figure 23(b). It is key to build up and understand Qbit working mechanism and theory. So, our work consists of how is Josephson junction in Qbit type's application with their challenges and solution [57]. Josephson junction (jj) represents phenomena of superconductivity current as apart development a super hardware by achieving quantum coherence to implement a quantum computer stronger than super convention binary computers which start in 1980s by Leggett [62–66]. Single cooper box came reported after 20 years to prove the oscillation of quantum coherent [67] and recently became great effort and progress on JJ to establish quantum computer. Superconducting quantum interferometers device (SQUIDs) research on a macroscopic quantum tunneling (MQT) and macroscopic Quantum coherence (MQC) basically through JJ to maintain quantum flux [54,68–75].

Despite of successful building 5-10 qubits jj-based computer in 2010, still forceful hundred qubits still a distance and hard to get so far due to qubit paring entanglement [57]. There were several reports of two qubits entanglement by operations gate and coupled JJ whether capacitive or inductive for controlled-NOT (CNOT) gate of two single cooper box (SCB)

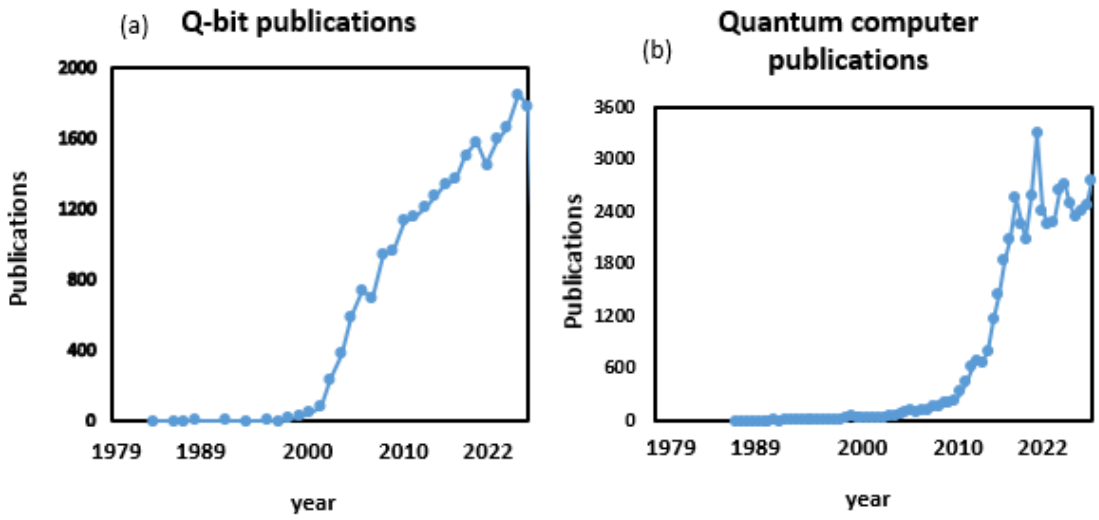

Figure 23: (a) q-bit publications annually cited by[Scopus-23669-Analyze-Year of qubit], and (b) shows publications related to quantum computer cited by [Scopus-13771-Analyze-Year of quantum computer].

with Hadamard gate[75–81]. Josephson junction (JJ) consider an example for lone work with q-bit coherence time with capability to scale up with two qubit gates where make it worthy to work with JJ in deep details. Qbit& Q-computer attract many researchers to produce it and number of publications increase rapidly as shown in the figure.

Josephson established as supercurrent law [82] of zero voltage between two superconductive electrodes connected by ultra-thin layer of isolative as following:

$$I_s = I_c \sin\Delta\theta \qquad \textbf{(2-6)}$$

I_C: critical current of junction considers the maximum supercurrent of zero voltage. Higher than Ic would shows no more zero voltage. It lies between µ-ampere and few milli-ampere

enough to overcome noise temperature especially in case of high temperature superconductors.

$\Delta\theta$: the two electrodes phase different of Ginzburg-landau wave function. If there is voltage exist, the equation would be as following:

$$\frac{d(\Delta\theta)}{dt} = \frac{2eV}{\hbar} \quad \textbf{(2-7)}$$

The quantum energy ($\hbar$) would be the energy difference of cooper pair moved through the junction. And energy get minimum when two phases of two electrodes are equal $\Delta\theta = n\pi$.

Those equations are applicable for any superconducting electrodes (S) connected with weak link such like isolative (I) material or normal metal (N) or constriction (C) as shown in figure 24. SEM image of Josephson junction is shown in figure 25.

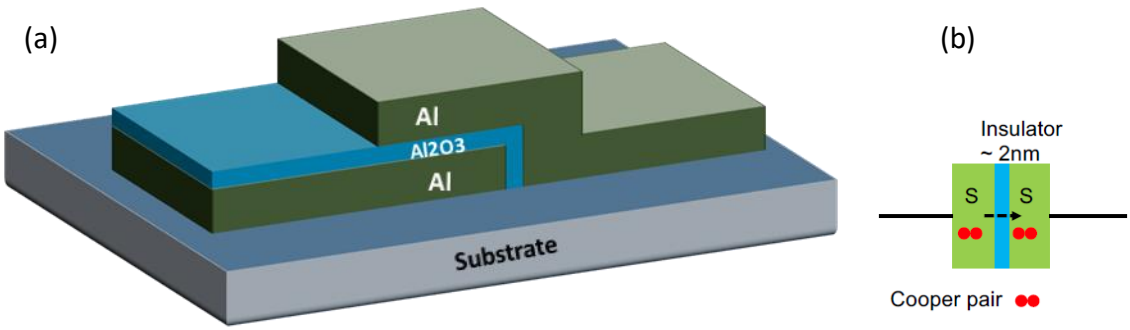

Figure 24: Superconducting Josephson tunnel junctions of (a) SIS- ($Al/Al_2O_3/Al$), and (b) Cooper pair electrons transfer through thin insulator.

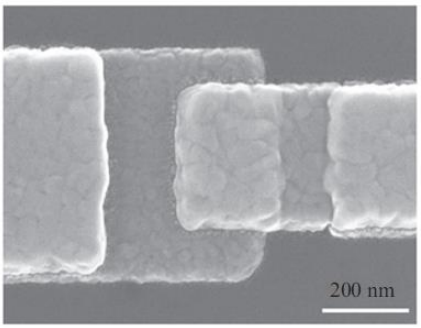

Figure 25: An SEM picture of a Josephson junction. Excerpt from the reference [83].

- **SQUID (superconducting quantum interferometer device) & Q-flux**

The superconducting quantum interference device (SQUID) has several applications due to consisting of superconductivity of two quantum phenomena: Cooper pair through isolative layer (Josephson Effect) and Flux loop quantization as shown in figure 26. It has two Josephson junctions causing a current that interfere with magnetic flux loop could be equal to (theoretically) a quantum flux which can be used to build up a Qbit [84].

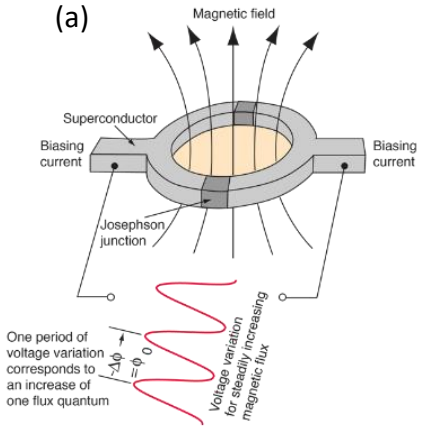

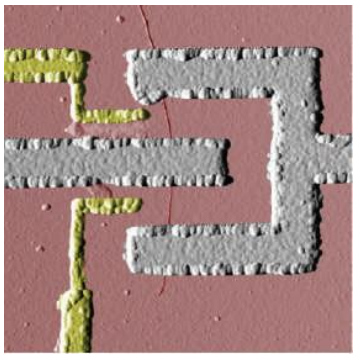

Figure 26: (a) SQUID with two Josephson junction interacts with magnetic field, and (b) CNT-SQUID device geometry with two gates G1 and G2 in yellow color. Excerpt from the reference [84].

It is so sensitive to magnetic field enough to be used as magnetometer to measure tiny magnetic field of brain activities. Fluxes in a superconducting loop are quantized in following equation: (quantum flux)

$$\varphi_0 = \frac{2\pi\hbar}{2e} \quad \textbf{(2-8)}$$

that could be measured practically by voltage variation through the circuits. [85] And hence The Josephson junction energy (E_j) would be

$$Ej = \frac{I_c\, \varphi_0}{2\pi} \quad \textbf{(2-9)}$$

the type of SQUID circuit relies on special element operation mode: direct current (dc-SQUID) and radio frequency (rf-SQUID). It took from 1984 to 2000 (16 years) to achieve quantum current macroscopic coherence in rf-squid by Friedman et al. after first mentioning of it by Leggett [64,74]. Relatively recent year in 2006 [84] carbon nanotubes have been used as structure of Josephson junction gate control in (CNT-SQUID) which showed more sensitive magnetometer makes it potential for more study of magnetization and spin states of single particle or molecule as shown in figure 26 (b).

- **Operation and decoherence**

Qubit operation could be defined as N-qubit in fully coherent system through a way of quantum algorithm which make it different from main body problem. It could be implanted

even with single or coupled q-bit pairs by set of universal gates of elementary operation [62,63].

Qbit superposition could represent by Bloch sphere as shown in figure 27 which rotate around x, y, z axes to get any point through the sphere by manipulating physical parameter values of JJ applied current representing phase qubit and applied magnetics flux representing flux qubit in addition to potential of electrostatic gate. The rotation could be implemented by rf pulses or microwaves with resonance frequency and small amplitudes, in another words: θ rotate by resonator frequency while Φ by phasing. As result; Hamiltonian of pseudospin could represent a universal quantum computer, it could be controlled by magnetic field.

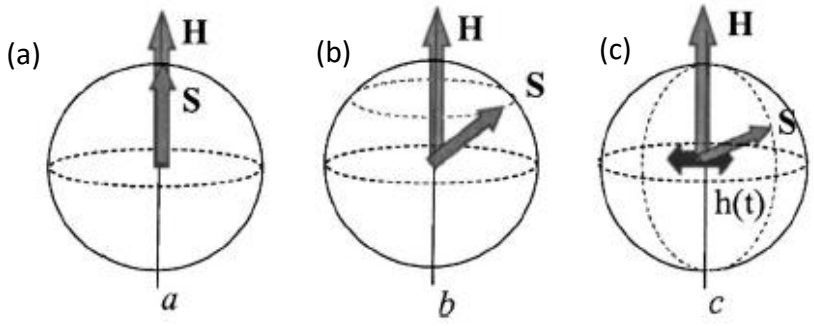

Figure 27: Bloch sphere with Bloch sphere vector S: (a) H (Hamiltonian) and S are parallel, (b) Free evolution of Bloch vector, and (c) Time dependent Rabi oscillation. Excerpt from the reference [57].

- **Pair Cooper box**

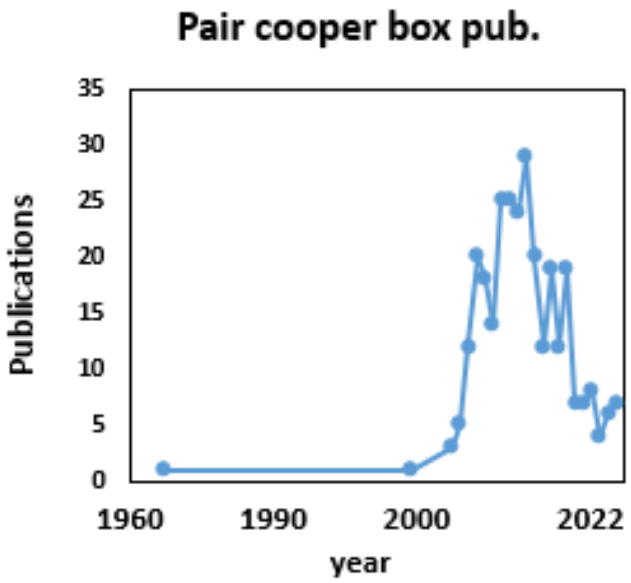

Figure 28: Cooper pair box publications trend is decreasing cited by [Scopus].

Cooper pair box is a qubit circuit which become less attractive due to high noisy level causing very short coherence time. The trend publications are start to disappear as shown in figure 28.

- **Transmon qubit**

The transmon qubit is a type of superconducting qubit that is designed to operate in the Cooper regime of $E_j \sim E_c$. Introduced by Michel Devoret, Robert Scheolkopf, and Steven Girvin in Yale University in 2007, the transmon qubit is a variant of the cooper pair box qubit, where the Josephson junction is shunted with a large capacitance to suppress charge noise sensitivity as shown in figure 29.

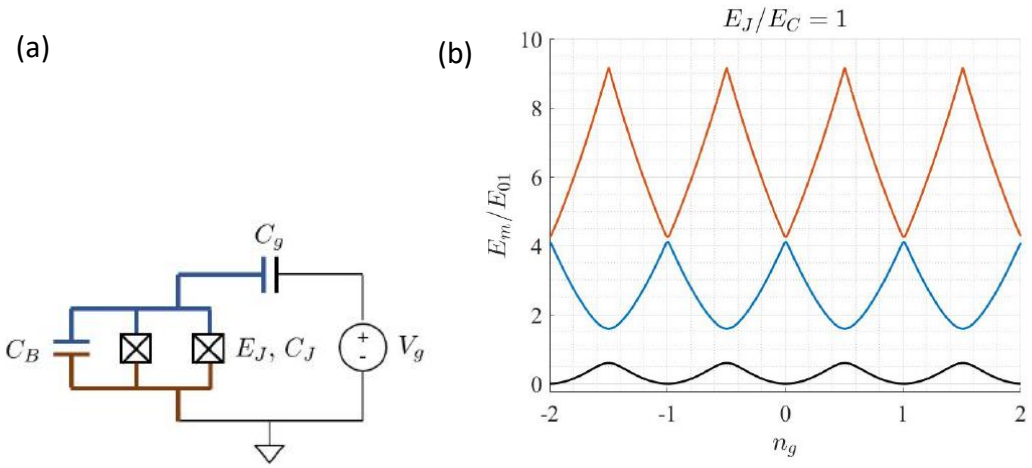

Figure 29: (a) transmon qubit circuit, and (b) noisy reduction signal from up to down. Excerpt from the reference [86].

This modification leads to an anharmonic energy spectrum, reducing the sensitivity of the qubit to charge fluctuations while maintaining a long coherence time. The huge capacitor looks like fingers to reduce the noise level

$$E_C = \frac{(2e)2}{2C}, \quad \textbf{(2-10)}$$

$$H = E_C\, n^2 + E_J \cos\varphi, \quad \textbf{(2-11)}$$

, noisy reduction: E_J/E_C.

2.3. Fabrication technology

Fabricating superconducting qubits [83], the basic units of quantum computers, requires specialized techniques and materials as shown in figure 30 to achieve the necessary quantum coherence and control. Here's an overview of the fabrication technology commonly used for superconducting qubits:

- **Substrate preparation:**

The fabrication process often begins with preparing a high-quality substrate, which is typically made of silicon wafer. This substrate provides a stable and well-defined platform for the subsequent layers of superconducting materials.

- **Deposition of bottom electrode:**

The first step involves depositing a superconducting material, such as niobium (Nb) or aluminum (Al), onto the substrate. This forms the bottom electrode of the qubit circuit. Techniques like sputtering or electron-beam deposition are commonly used for this step.

- **Lithography:**

Lithography is used to define the circuit pattern on the superconducting layer. Electron-beam lithography or photolithography techniques are employed to create precise patterns with nanometer-scale features.

- **Etching:**

Reactive ion etching (RIE) is used to remove the unwanted superconducting material, leaving behind the desired qubit circuit pattern. The etching process defines the shape of the qubit structure and the circuit's components, such as Josephson junctions and resonators.

- **Josephson Junctions:**

Josephson junctions are created by interrupting a superconducting wire with a thin insulating barrier, such as a thin oxide layer. This interruption allows for the quantum tunneling of Cooper pairs and is essential for qubit operation.

- **Dielectric layer deposition:**

Dielectric layers such as a metal oxide are deposited on top of the qubit circuit to insulate it from other layers and provide protection against environmental noise.

- **Resonators and microwave lines:**

Superconducting resonators and microwave lines are integrated into the qubit circuit for control and readout purposes. These components are designed to couple with microwave signals used to manipulate and measure qubit states.

- **Top electrode deposition:**

Another layer of superconducting material is deposited on top of the circuit, forming the top electrode. This completes the qubit structure. The junctions and other circuit components are carefully designed to create the desired quantum behavior.

- **Annealing and cleaning:**

After the deposition steps, the qubit circuit may undergo annealing at low temperatures to improve the quality of the superconducting material and reduce defects. Cleaning steps are also performed to ensure the purity of the qubit structure.

- **Wire bonding and packaging:**

Once the qubits are fabricated on a wafer, they are wire-bonded to external control and readout circuitry. The wafer is then encapsulated in a cryogenic package to maintain the low temperatures required for superconducting operation.

- **Cryogenic cooling and calibration:**

The packaged qubits are cooled to ultra-low temperatures using cryogenic systems. Calibration and tuning of the qubits' control parameters are performed to ensure their proper functioning and coherence.

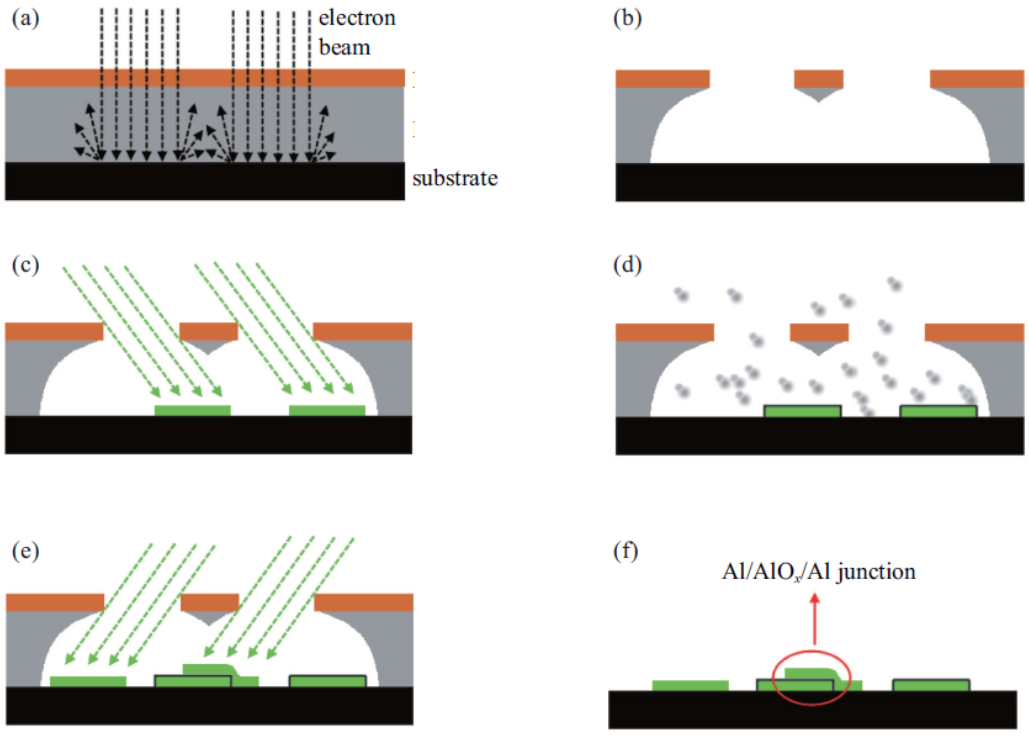

Figure 30: Schematics of Dolan bridge shadow evaporation fabrication process, (a) electron beam writing, (b) development,
(c) first aluminum layer evaporation, (d) oxidation, (e) second aluminum layer evaporation, and (f) liftoff. Excerpt from the reference [83].

- **Control and measurement:**

Control pulses and microwave signals are sent to the qubits through the microwave lines, and their quantum states are read out using resonators and amplifiers. This process enables quantum operations and state measurement.

2.4. Conclusions

Josephson junctions (JJ) play a crucial role in the development of quantum bits (qubits) and show promising potential for replacing conventional bit circuits in quantum computers. JJ allows for the phenomenon of superconducting current and enables the realization of quantum coherence, which is essential for building a quantum computer that can outperform classical binary computers. Over the years, there have been significant advancements in JJ-based quantum technologies, such as single Cooper box and Superconducting Quantum Interference Devices (SQUIDs), which have been used to study macroscopic quantum tunneling (MQT) and macroscopic quantum coherence (MQC). However, despite the successful demonstration of 5-10 qubit JJ-based computers, achieving a large-scale quantum computer with hundreds of qubits remains challenging due to issues such as qubit entanglement. Quantum circuits based on JJ can be developed with various configurations, including single JJ current-biased circuits, RF-SQUID circuits, and single Cooper pair box circuits. These circuits typically consist of linear inductors, capacitors with JJ, and nonlinear inductors of Josephson tunnel junctions. Quantum circuits are not intuitive, as they operate at GHz frequencies with wavelengths in the centimeter range, in contrast to classical circuits which are much larger in size. Quantum electrodynamics and macroscopic quantum

tunneling were observed in JJ circuits, and the nonlinear and nondissipative nature of Josephson tunneling allows for the observation of quantum dynamics. The Hamiltonian form is used as the basis for the quantum description of qubits, with the variables representing the kinetic and potential energies of the capacitive elements and Josephson inductance. The phase difference in JJ circuits can be expressed in terms of the Hamiltonian energy difference, which relates the voltage drop and magnetic flux in JJ circuits. By replacing the inductance in L_C circuits with JJ, inharmonic energy levels can be achieved, which are crucial for quantum information processing. In summary, JJ is a key component in quantum computing and quantum information processing. Despite the challenges in scaling up qubit systems, significant progress has been made in JJ-based technologies, and research in this field continues to grow rapidly. Further understanding and utilization of JJ in quantum circuits and systems can potentially lead to the realization of large-scale, fault-tolerant quantum computers with practical applications in various fields.

I_C is the critical current of the Josephson junction, which is a fundamental parameter that determines the maximum current that can flow through the junction without inducing voltage across it. $\Delta\theta$ is the phase difference across the junction, which represents the quantum mechanical phase associated with the superconducting wave function. Josephson junctions can be classified into two main types: the weak-link junction and the tunnel junction. In the weak-link junction, the superconductivity is suppressed due to a constriction in the junction, creating a narrow region with reduced superconducting order parameter. This results in a weak-link through which the supercurrent can flow. The tunnel junction, on the other hand, consists of an insulating barrier sandwiched between two superconducting electrodes. Quantum tunneling allows Cooper pairs to tunnel through the barrier, resulting in a Josephson

current. Josephson junctions have several unique properties that make them attractive for qubit applications. One of the key properties is their ability to exhibit macroscopic quantum phenomena, such as quantum tunneling and quantum interference, at relatively large scales. This allows for the creation of qubits that can be manipulated and controlled using electrical signals, making them compatible with existing semiconductor fabrication techniques. Furthermore, Josephson junctions can be fabricated in a variety of geometries and configurations, such as single junctions, SQUIDs, and superconducting resonators, allowing for flexibility in qubit design and implementation. They can also have long coherence times, which is a crucial requirement for qubits to maintain quantum information without decoherence. Despite their promising properties, Josephson junction-based qubits face several challenges. One major challenge is qubit coherence time, which refers to the duration for which a qubit can retain its quantum information. Coherence time is affected by various factors, such as energy relaxation, dephasing, and flux noise, which can limit the performance of Josephson junction-based qubits. Additionally, achieving high-fidelity two-qubit gates, which are necessary for quantum error correction and fault-tolerant quantum computing, remains challenging with Josephson junction-based qubits. To overcome these challenges, researchers have been exploring various techniques, such as using advanced fabrication methods to reduce defects in Josephson junctions, implementing error-correction codes to mitigate the effects of noise, and developing novel qubit designs that are less sensitive to environmental fluctuations. Additionally, advancements in materials science and device engineering have led to the development of new types of Josephson junctions, such as topological Josephson junctions and hybrid junctions, which offer potential solutions to some of the existing challenges. Overall, Josephson junctions play a crucial role in the development

of quantum bits (qubits) and show promising potential for replacing conventional bit circuits in quantum computers. They offer unique properties that make them attractive for qubit applications, such as macroscopic quantum phenomena, fabrication flexibility, and long coherence times. However, challenges related to qubit coherence time and two-qubit gate fidelity remain, and researchers are actively working on developing solutions to overcome these challenges. With continued advancements in materials science, device engineering, and quantum error correction techniques, Josephson junction-based qubits hold promise for the realization of scalable and fault-tolerant quantum computers.

3. Aluminum Thin films growth by the precursor of DMEAA

3.1. Introduction

Atomic layer deposition (ALD) technique enables us to fabricate atomically controlled thin films [1]. ALD technique can deposit insulating materials conformally which can cover the whole surface of nanowires [87] and realize quantum point contact made of a narrow $In_{0.75}Ga_{0.25}As$ channel [88]. It can be also used as the passivation layer in order to stabilize adsorbed molecules [89]. ALD technique can also deposit metallic thin films and show a sharp interface between different materials as the sequential deposition [90]. The rather low growth temperature of ALD technique offers in situ photoresist processes. These features are promising to fabricate stacked tunnel junctions including a Josephson tunnel junction that is composed of two superconducting electrodes separated by a very thin (~ 2 nm) insulating barrier.

In our study, we present an extensive analysis of the growth process employed for aluminum (111) thin films, utilizing the atomic layer deposition (ALD) technique with dimethylethylamine alane (DMEAA) as the precursor. Notably, we have observed that the presence of a metallic underlayer is crucial for achieving the uniform growth of aluminum films using DMEAA precursor. By employing a titanium thin film as the underlayer, we have successfully obtained aluminum thin films with a consistent (111) orientation, regardless of the substrate used.

Moreover, we have determined that the lattice constant and superconducting transition temperature of these aluminum thin films closely match those of bulk aluminum. These significant findings strongly indicate that the ALD technique exhibits exceptional capabilities in producing high-quality aluminum thin films, thereby demonstrating its potential for various applications in the field of superconducting devices.

Additionally, we delve into an in-depth discussion regarding the promising prospects of utilizing the ALD technique with the DMEAA precursor for the fabrication of vertical small Josephson tunnel junctions. Such junctions hold immense value as they can serve as the foundation for superconducting quantum bits, thereby paving the way for advancements in quantum computing and related technologies.

Here, we study the growth of aluminum thin films by ALD with DMEAA as a precursor. We found the metallic underlayer is necessary for growing aluminum films. The ALD-grown aluminum films show superconductivity as the same as bulk aluminum.

3.2. Precursor selection

There are several reports on precursors for the ALD growth of aluminum thin films. TMA and H_2O is a standard process to grow aluminum oxide [1], while TMA and hydrogen is used to grow aluminum thin film[91]. Dimethylaluminum hydride (DMAH) is also a good candidate as the precursor which offers reduced carbon contamination [92] and an area-selective growth [93]. DMEAA characteristics, such has no an Al-C bond, make it a promising candidate for a range of applications Among the three precursors, we decide to use DMEAA, which has several advantages: a low decomposition temperature [94], avoiding

carbon contamination, and a long-term stability compared with DMAH [95]. Although some groups reported the superiority of DMAH compared with DMEAA [92], DMAH has the disadvantages of the rough surface.

- **Dimethylethylamine alane**

Dimethylethylamine alane (DMEAA), with the chemical formula Al $(CH_3)_2(C_2H_5NH_2)$ as shown in figure 31(a), is a complex organoaluminium compound that combines the properties of both amine and aluminum source [96,97]. DMEAA characteristics, such has no an Al-C bond, make it a promising candidate for a range of applications, including energy storage, catalysis, and materials science. It has been investigated as potential materials for hydrogen storage due to their ability to reversibly release and store hydrogen [98]. It is worth noting that the viscosity of DMEAA is stable so that the reproducibility of deposition conditions for aluminum thin films is high while we found that the viscosity of DMAH changes in six weeks and thereby it is very difficult to grow reproducibly aluminum thin films under the same conditions.

- **Trimethylaluminum**

Trimethylaluminum (TMA), with the chemical formula Al $(CH_3)_3$ as shown in figure 31(b), is a highly reactive and pyrophoric organoaluminium compound. TMA has gained immense popularity owing to its unique properties and diverse applications in numerous scientific and industrial domains. It considers one of the simplest examples of an organoaluminium compound. Despite its name, it is a dimer and has the formula $Al_2(CH3)_6$ (also known as Al_2Me_6 or TMA). This liquid is pyrophoric and colorless[99].

(a) **DMEAA**

Dimethylethylamine alane

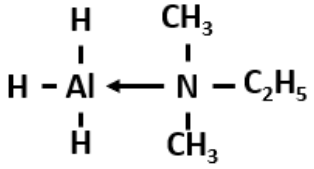

(b) **TMA**

Trimethylaluminum

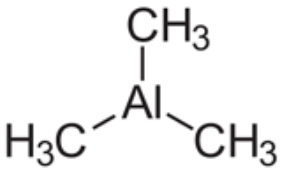

(c) **DMAH**

Dimethylaluminum hydride

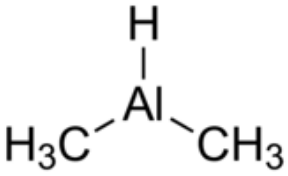

Figure 31: The chemical formula of (a) DMEAA, (b) TMA, and (c) DMAH.

- **Dimethylaluminum hydride**

Di-methyl-aluminum hydride (DMAH), with the chemical formula $(CH_3)_2AlH$ as shown in figure 31(c), is a versatile organoaluminium compound with diverse reactivity and applications. DMAH has much rapid aging effect compared with that of DMEAA. The properties will be changed. DMAH decomposition temperature is 623–673 °K [100].

3.3. Film growth conditions:

Surface treatments of Si wafers is essential to grow material thins films without troubles on surface. It performs inside a clean room where a control of all kind of contamination to a certain level specially dust particles and a place to supply chemicals and liquids essential for experimental. Furthermore, Humidity & Temperature are controlled. There is an ultra-cleanroom were extra control of low number of particles. ALD parameters are pulsing time, pursing time, and growth temperature.

- **Substrate preparation**

We used silicon (Si) substrates for aluminum deposition. Two of Si-substrates are prepared, one as bare substrate and the latter with a metallic layer. Both substrates are prepared with the standard degrease process and surface etching by tetramethylammonium hydroxide solution [101]. It is found that aluminum thin films can be grown on the metallic layer [102]. As a metallic underlayer, a 1.5 nm-thick titanium film is deposited on the silicon substrate by electron-beam with a very low deposition rate of 0.05 nm/sec., which gives a smooth surface. After the deposition of Ti seed layer on the Si substrate, the substrate must be installed into the ALD chamber within half an hour in order to avoid the surface oxidation.

The growth of aluminum from DMEAA is not a self-limited process, thus an aluminum monolayer (ML) growth can be tuned by the combination of an amount of DMEAA which is determined by the valve opening time of DMEAA, t_{open}, purging time

removing by-products from the chamber, t_{purge}, and the growth temperature in the chamber, T. The ALD chamber is equipped with the hot-wall and thus the whole chamber is kept at the same temperature during the film growth. By adjusting three conditions, we can obtain 0.3 ML to 4 ML growth per cycle (GPC). The following results were obtained with the growth conditions of 300 ALD cycles that t_{open}, $t_{purge,}$ and T are 0.3 seconds, 3.0 seconds, and 150 degrees Celsius, respectively.

The surface morphology of one of the aluminum thin films and its thickness are characterized by field emission scanning electron microscopy (SEM, JEOL JSM-6340F capable of getting image resolution of 3 nm). The rough estimate of the surface roughness was obtained from a 45° tilted view of cross-section SEM image of an Al film prepared over a Ti underlayer. No signal filtering was applied and data was corrected for the tilted geometry. The average distance between the edges of the Ti layer and along the lumen was evaluated. Moreover, the maximum peak-to-valley (PV) distance and root mean square (RMS) roughness of the edge of the Al film with the lumen were also estimated, all of these with the help of the Gatan digital micrograph ver. 3.4. The composition and crystal orientation of the two films were estimated from X-ray diffraction (XRD) measurements performed with XRD (Rigaku TTR-III) apparatus, using a Cu Kα x-ray source (1.5406 Å) and the apparatus software package.

The resistance measurements were performed into the 0.3 K refrigerator with a 3T superconducting magnet. The temperature was measured by the ruthenium oxide thermometer located at the sample stage.

- **Clean room regulations**

The clean room regulations outline strict guidelines for maintaining a controlled environment. Within the clean room, only specialized clean room notes are permitted, while regular paper or notes are prohibited. It's mandatory to don the designated clean room attire before entering to prevent contamination. The use of pencil and fountain pen is disallowed, with ballpoint pens being the approved writing instruments. Additionally, precautions must be taken to avoid contact with emergency locks, like those found in air shower transition areas, and a practice of not opening inner and outer doors simultaneously is emphasized until any ongoing procedures are completed, as indicated by the conclusion of a designated time.

- **Substrate preparation and washing process**

- Substrate can be cut by a diamond scriber. The edge shouldn't be scratch much to avoid surface crystal damage. Scratching is drawn on bottom non mirror surface. A ruler paper can be used to determine substrates desired dimensions.
- After drawing splitting line on the substrate, it could be separated by hands thumbs.
- We can use polished paper on fabric tissue to control substrate dust resulting from and scratching & splitting the wafer.
    - Flow box should be fully opened, it contains a sensor that release alarm after 20 minutes of illuminating red led. The flow box window could be open slightly enough to insert hands, the sensor red led would be turned off as well.
- Washing solutions prepare in different labelled **beaker** separately as following: Acetone, Isopropyl Alcohol (IPA), pure water, and Semico respectively. Substrates

should be completely soaked for **3 minutes each step** using ultra sonication (80% of power) in following certain sequences as shown in figure 32.

-The role of each solution:

- Acetone: removes Oil contamination on the substrate surface.
- Isopropyl Alcohol (IPA): removes Acetone from surface before immersing into water to avoid substrate surface intrinsic troubles.
- Pure water: removes IPA and other contaminations. It is a mixture between DI Water & pure water with elevated resistivity of DI from 15 to 18 million ohms (MΩ)/cm
- Semico 23: is a special secret Alkali solution of NTT, uses for pure Si substrate wash in while it is not recommended for SiO_2 & others subs.

- Then soak wafer surface with some Ethanol spray after putting it above fabric tissues then blowing all droplets by a gun of low N_2 pressure. This step to distribute OH groups on substrate surface.
- If there are some sticky droplets into surface that means surface still haven't cleaned well and require to repeat all pervious steps.
- No need to use O_2-plasma to avoid surface troubles.

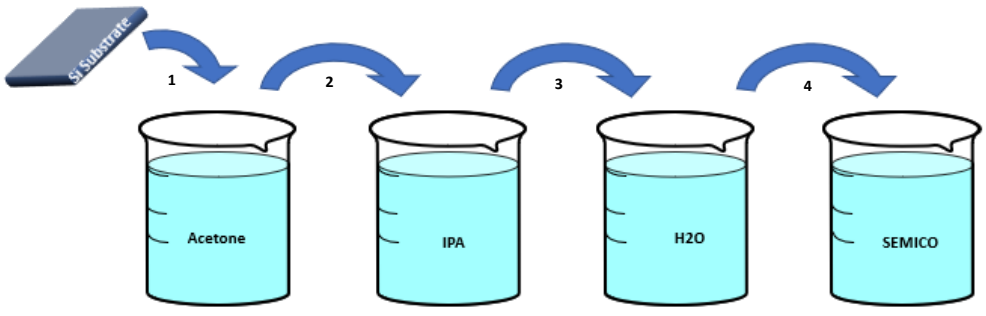

Figure 32: Si-Substrate cleaning process steps.

Figure 33: ALD equipment with a glove box.

- Plastic tweezers are used to carry substrates.
- The cleaned surface is maintained by preventing gases from entering through a flow glove box attached to the instrument, as shown in figure 33.

- **Waste management:**

  - **Beakers** can be cleaned with pure water and then dried by fabric tissues.
  - All working placed should be cleaned well and washed.
  - There are two flow boxes, one contains acid waste and another for Alkali. There is a special drainage for arsenic content materials. Water can be drained inside flow box.
  - There are three recycle bins for gloved and tissues as following: Acid and alkali contents, Organic content and uncontaminated.
  - Using any material sources should be registered and recorded.

- **Underlayer deposition**

An electron beam evaporator is a specialized device used in thin-film deposition processes, commonly employed in the manufacturing of semiconductors, optics, coatings, and other advanced materials. It is a method for depositing thin films of various materials onto substrates by utilizing the principle of thermal evaporation. A 1.5 nm-thick titanium film is applied as a metallic underlayer on the silicon substrate using electron-beam deposition. The deposition process has an exceptionally low rate of 0.05 nm/sec, ensuring the attainment of a smooth surface. Once the titanium underlayer is deposited on the silicon substrate, it is crucial to promptly transfer it into the ALD chamber within thirty minutes to prevent oxidation of the surface as shown in figure 34. Electron beam evaporation is used due to several advantages over other deposition techniques, such as sputtering or thermal resistance evaporation:

-High Purity: Because the source material is vaporized directly from a solid state, the deposited films tend to be of high purity with minimal contamination.

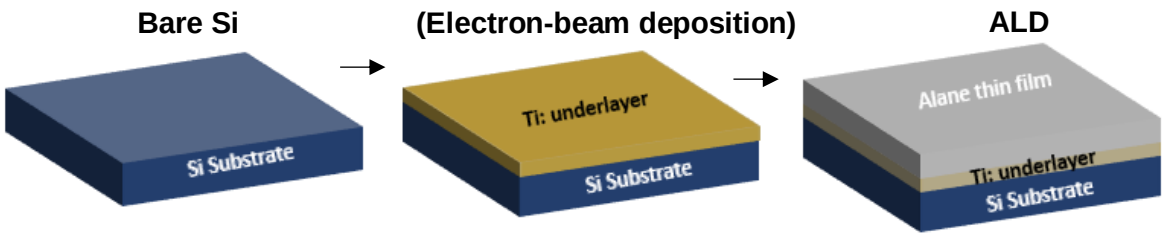

Figure 34*:* Underlayer deposition process.

-Precise Control: Electron beam evaporation allows for fine control over deposition rates, thicknesses, and material properties, making it suitable for creating underlayer films.

-Uniformity: With proper chamber design and control, electron beam evaporation can result in highly uniform film deposition across large substrate areas.

3.4. Characterizations of aluminum thin films

Field emission scanning electron microscopy (FESEM, JEOL JSM-6340F) was employed to analyze the surface morphology and thickness of the alane thin films. The FESEM instrument is capable of capturing images with a resolution of 3 nm. By analyzing a 45° tilted view of a cross-section SEM image of the grown thin film, an estimate of the surface roughness is obtained. No signal filtering is applied, and the data is appropriately adjusted to compensate for the tilted geometry. The evaluation involves determining the average distance between the edges of the titanium layer and along the lumen. Furthermore, using the Gatan digital micrograph ver. 3.4 software, estimations are made for the maximum peak-to-valley (PV) distance and the root mean square (RMS) roughness of the alane film's edge in relation to the lumen. To ascertain the composition and crystal orientation of the two samples, X-ray diffraction (XRD) measurements are conducted using a Rigaku TTR-III apparatus. The XRD analysis utilizes a Cu Kα x-ray source with a wavelength of 1.5406 Å, along with the software package provided by the apparatus manufacturer.

- **Scanning electron microscope (SEM)**

It is a powerful imaging instrument used for detailed analysis and imaging of various materials at high magnifications and resolutions. SEMs can achieve high levels of magnification, ranging from tens to hundreds of thousands of times. This allows for the observation of fine details and surface structures at nanometer scales.

SEM is widely used in various fields, including materials science, nanotechnology, biology, geology, forensics, and more. It provides valuable information about the surface morphology, topography, composition, and structure of samples. SEM images can reveal details that are often not visible using optical microscopes, making it an essential tool for scientific research and industrial applications.

SEMs provide a three-dimensional view of the surface of a sample by using a focused electron beam to scan the sample's surface and generate images based on interactions between the electrons and the sample.

It consists of following:

-Electron Source: SEMs use an electron gun to generate a focused beam of high-energy electrons. These electrons are typically emitted from a heated filament or a field-emission source.

-Sample Preparation: The sample is prepared for imaging by being coated with a thin layer of conductive material (e.g., gold, gold-palladium alloy) to prevent charging effects and enhance conductivity. The sample should also be vacuum-compatible to ensure optimal performance within the SEM's vacuum chamber.

-Electron Beam Interaction: The focused electron beam is directed onto the surface of the sample. When the electrons strike the sample, various interactions occur, including:

-Backscattered Electrons (BSE): Some electrons are backscattered from the sample's surface. BSE detection is used to gather compositional information and create contrast in images.

-Secondary Electrons (SE): These low-energy electrons are emitted from the sample's surface due to the impact of the primary electron beam. SEs provide topographical information and form the basis for creating high-resolution images.

The emitted secondary electrons and backscattered electrons are detected by specialized detectors. These signals are used to create images of the sample's surface. The SEM can produce images with various contrasts, such as secondary electron images, and backscattered electron images.

-Sample Stage: The sample is mounted on a movable stage that allows for precise positioning and movement. This enables imaging different areas of the sample and capturing images at different angles.

- **X-ray diffraction (XRD)**

X-ray diffraction (XRD) is an essential tool in materials science, chemistry, geology, and various industries such as pharmaceuticals, metallurgy, ceramics, and electronics, where understanding the atomic arrangement and crystallography of materials is crucial for developing new materials or improving existing ones. This technique provides information about the crystallography, phase composition, crystal size, lattice parameters, and other structural characteristics of a material.

-Principle of Diffraction: X-rays are electromagnetic waves with wavelengths on the order of angstroms (10^{-10} meters), which is comparable to the interatomic distances in crystalline materials. When X-rays strike a crystalline sample, they interact with the regularly spaced atoms in the crystal lattice.

-Diffraction Pattern: The X-rays are scattered in different directions by the crystal lattice's atoms. This scattering causes constructive interference when the scattered waves are in phase and destructive interference when they are out of phase. The resulting pattern of constructive and destructive interference forms a diffraction pattern.

-Detector: A detector is used to capture the diffraction pattern produced by the X-rays that have interacted with the crystal. The diffraction pattern contains information about the arrangement of atoms in the crystal lattice.

-Analysis: The obtained diffraction pattern is then analyzed using mathematical techniques to determine the angles and intensities of the diffraction peaks. These peaks correspond to the specific crystal planes within the lattice and provide information about the crystal's structure.

-Crystallography: By analyzing the diffraction pattern and comparing it to known patterns from databases, researchers can deduce the crystal structure, lattice parameters, and orientation of the crystalline material. This information helps in identifying the type of crystal, its symmetry, and the presence of different phases.

X-ray diffraction has numerous applications such as material identification, phase Analysis, quantitative Analysis, and crystallite Size and Strain.

- **Four-probe magnetoresistance measurement**

Measuring the relationship between magnetic field and resistance of a thin film involves a technique called magnetoresistance measurement. Magnetoresistance is the change in electrical resistance of a material in response to an applied magnetic field. There are several methods you can use to perform magnetoresistance measurements on thin films. One of the most common techniques is the "Four-Probe" method.

The measurement method is gradually applying a magnetic field to the thin film sample. The field strength can be varied as needed. while maintaining the constant current, measuring the voltage across the sample as the magnetic field strength is changed. This can be done by varying the current or the magnetic field and recording the corresponding voltage.

A graph of magnetic field strength versus resistance can be plotted through Calculate the resistance (R) at each magnetic field strength using Ohm's law: R = V/I. This graph is the magnetoresistance curve, which shows how the resistance of the thin film changes as the magnetic field is varied.

It's important to note that the accuracy and precision of magnetoresistance measurements depend on factors such as the quality of electrical contacts. Therefore, gold wires are used to avoid creating any gold-aluminum alloys that could potentially become insulators. using four-point measurements rather than two-point measurements is to avoid encountering contact resistance into measurements results. The reason is that two-point measurements can be influenced by the resistance of the contacts, which could result in inaccurate results for the grown thin film. In contrast, four-point measurements provide accurate readings of the

sample's resistance by eliminating the impact of contact resistance. Additionally, they are more sensitive to low resistance values as well.

- **Results and Discussion**

Figure 35 (a) and (b) show the SEM images of the grown thin film of aluminum on a silicon substrate without and with a titanium underlayer, respectively. We grow aluminum thin films onto the bare silicon substrates at various growth conditions. However, in the absence of a Ti underlayer, only aluminum nano-grains were obtained on the Si substrate as shown in figure 35 (a). On the other hand, as shown in figure 35 (b), aluminum thin film with the Ti underlayer shows a mirror-like smooth surface. We speculate that Ti removes hydrogen ions from alane (AlH_3) in a similar mechanism of the decomposition of alane by titanium (IV) isopropoxide [103]. Indeed, aluminum films can't be obtained when a 1.5 nm thick Ti underlayer is exposed into the ambient atmosphere for more than half an hour due to the surface oxidation of a Ti film. The average thickness and standard deviation of the aluminum film grown for 300 ALD cycles with a GPC of 3ML/cycle are 220 ± 33 nm, and estimates of the RMS roughness and maximum observed peak-to-valley of the cleaved edge of the sample are 16 nm and 150 nm, respectively. The material choice of the underlayer is also considered.

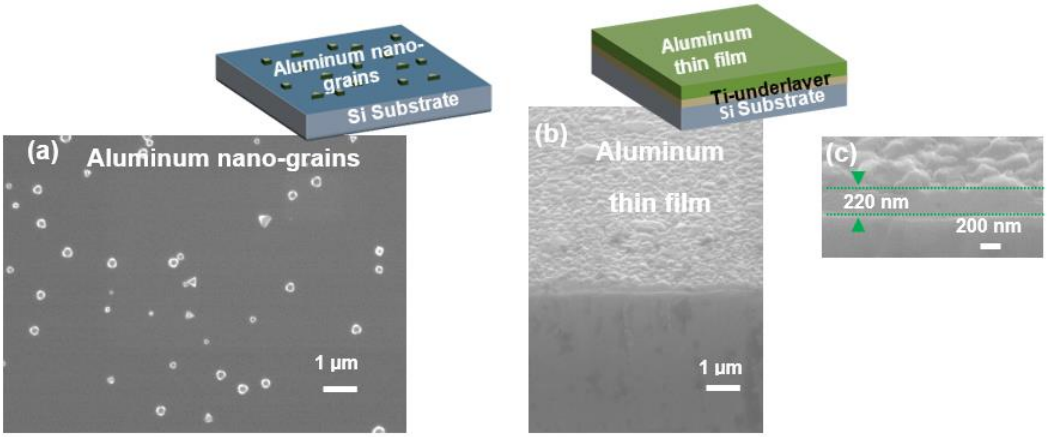

Figure 35: SEM images with respective illustrative drawings of (a) Top view of aluminum nano-grains grown on the bare Si substrate, (b) tilted-view (45°) of the aluminum thin film on the Si substrate with a titanium underlayer, and (c) cross section image of average-thickness of aluminum thin film. Excerpt from the reference [104].

We found gold sometimes produces intermetallic compounds with aluminum [105], moreover Al on gold thin film sometimes creates an insulating film. We choose a very thin titanium film as the underlayer in this work. XRD measurements indicate that an aluminum film with the Ti seed layer on the Si substrate has (111) orientation with a peak of $2\Theta = 38.5$ degrees [106] as shown in figure 36. The peak at $2\Theta = 69$ degrees represents Si (400) orientation of the substrate. Al (111) is an ideal orientation due to the high resistance of stress migration with a longer lifetime as an electrode for device applications [106,107]. We also grew aluminum films on other substrates, such as GaAs and sapphire, with a Ti under layer and found all of the aluminum films show (111) orientation. Our results are coincident with the reference [106].

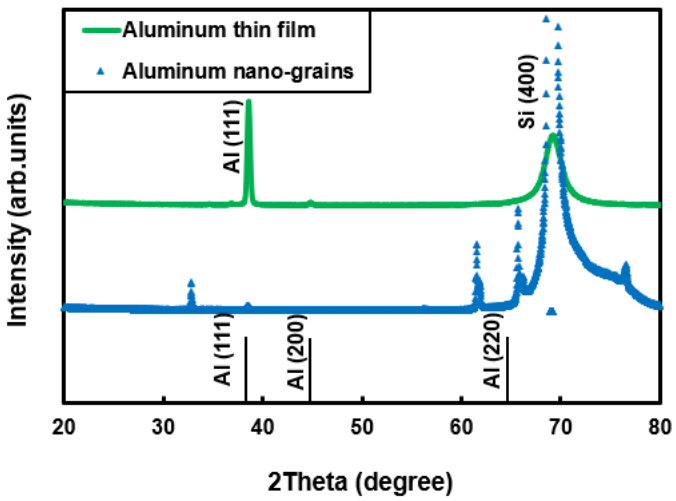

Figure 36: XRD analysis shows the aluminum texture of (111) orientation at 2Θ = 38.5º for both the thin film and nano-grains along with stacked lines of the standard reference at the bottom. The peak at 2Θ = 69 degrees represents Si (400) orientation of the substrate. Excerpt from the reference [104].

Further analysis for the XRD peak of Al (111) at 2Θ = 38.5 degrees is performed to acquire crystal information of the grown thin film. The full width at half maximum (FWHM) value was obtained to be 0.295 degrees. The plane distance of the grown aluminum (111) thin film was derived to be 0.233 nm. The mean grain size of the aluminum thin film was 32 nm calculated from the Scherrer equation as following:

$$Lc = \frac{K_\lambda}{FWHM * Cos\theta} \qquad \textbf{(4-1)}$$

where L_c is crystallite size, and K = 1.

Due to the non-uniformity of gas flow, its surface has a mirror and white parts as shown in figure 37. The mirror part is composed of smaller grains and shows the (111) orientation. However, the white part is composed of larger grains and shows more roughness of same orientation. It is estimated that the average thickness of both mirror and white parts is (228)

nm and (767) nm, respectively. Furthermore, the white part contains beta-alane (β-AlH_3) from the X-ray diffraction (XRD) analysis as shown in figure 38. We observed that the aluminum film has mainly (111) orientation with a small amount of (100) due to chemical bond deposition of chemical reaction. The surface roughness of the white part is related to the existence of alane (AlH_3) which contributes to increasing the size of the gains due to its large cell parameters comparing to aluminum enhancing Stranski–Krastanow growth. An X-ray diffraction (XRD) analysis shows the dominance of beta-alane (β-AlH_3) contamination of (311) orientation. It exits because of incomplete dehydration reaction at 150 degrees Celsius on Si surface.

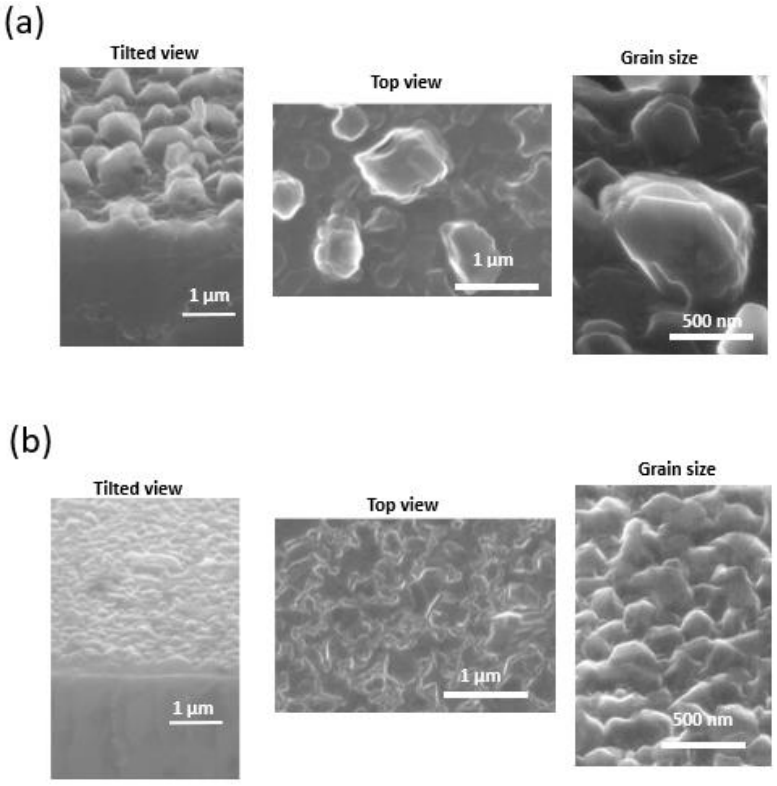

Figure 37: Tilted view, top view, and grain size for (a) white, and (b) mirror parts in the aluminum film.

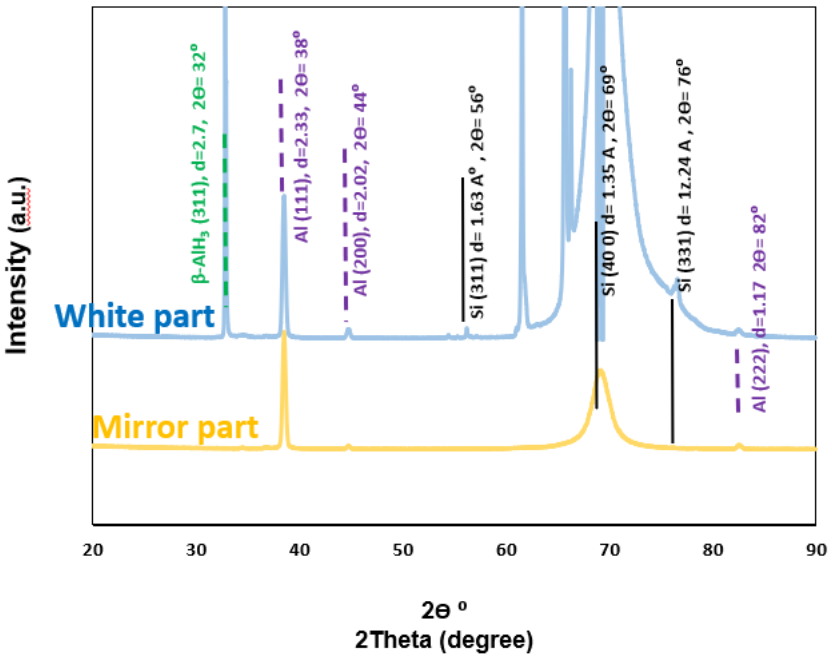

Figure 38: XRD of β-alane thin film in white part.

- **Crystal Structure and Morphology Investigation of white part of thin film**

SEM images as shown in figure 37 the thin film of alane on a silicon substrate, with a top view and tilted view. XRD detected β-alane thin film in white part as shown in figure 38. Figure 39 and 40 illustrates that the alane thin film exhibited a rough, white-like surface. alane thin films were grown on bare silicon substrates under different growth conditions. However, when a conductive underlayer was absent, only alane nano-grains were observed on the silicon substrate.

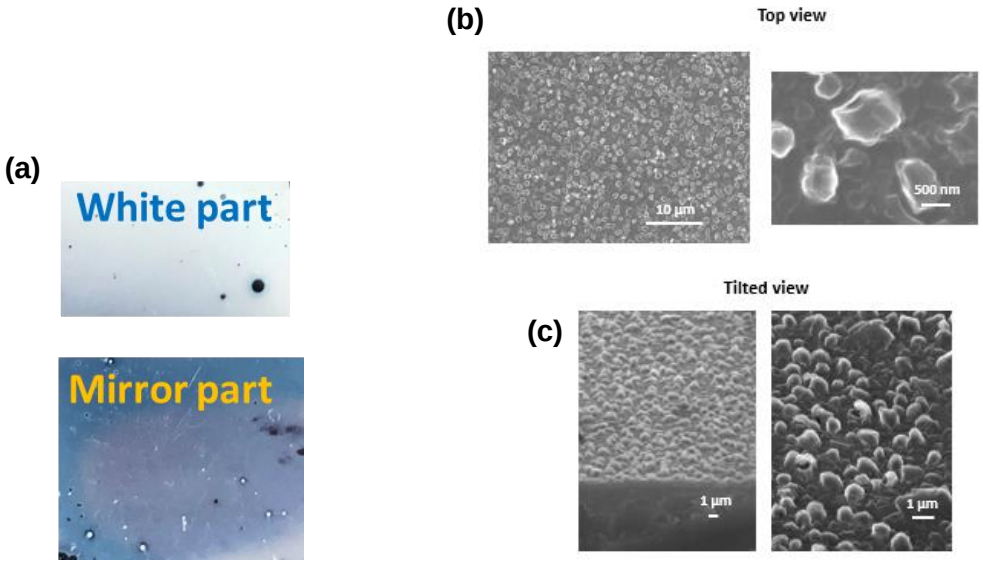

Figure 39: (a) white and mirror thin film, (b) SEM top view of white part thin film, (c) tilted view.

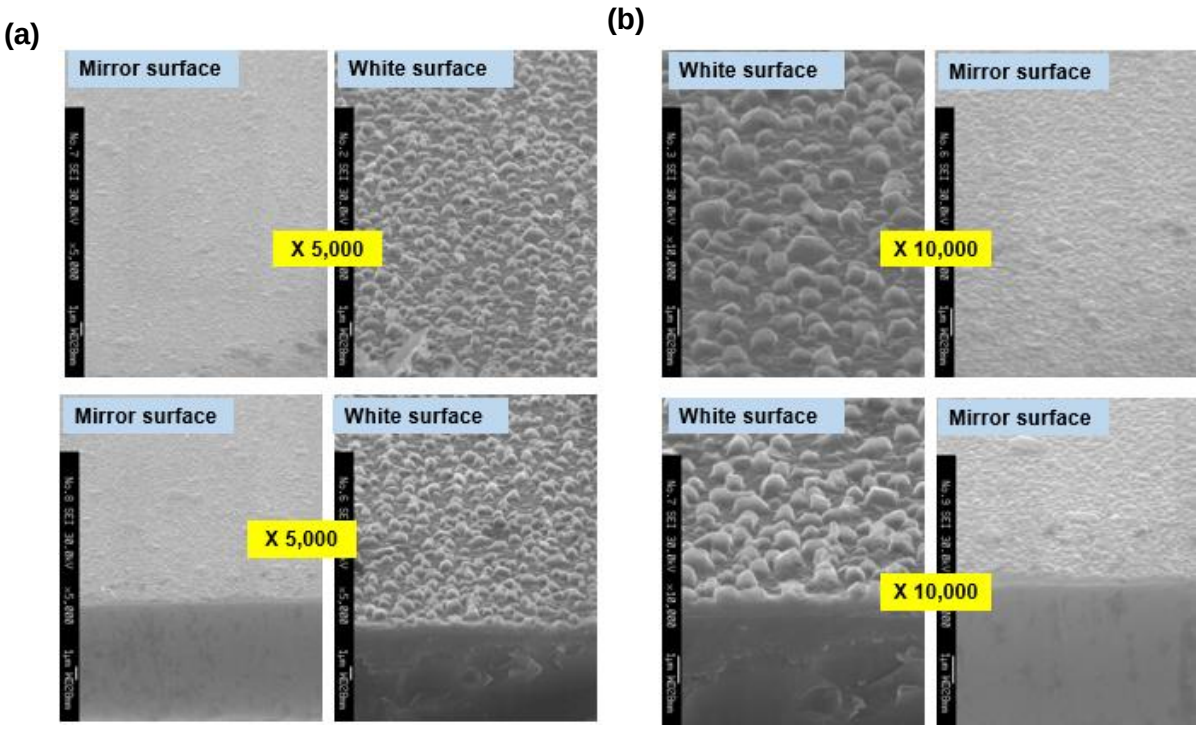

Figure 40: SEM for mirror and white surface at magnification of (a) X 5000, and (b) X 10,000.

Notably, when a 1.5 nm thick titanium underlayer is exposed to the ambient atmosphere for more than half an hour, the oxidation of the titanium film prevents the formation of thin films. For alane films grown using 300 ALD cycles with a growth per cycle (GPC) of 2.6 nm/cycle, the average thickness and standard deviation were measured as 767 ± 174 nm as shown in figure 41, while for the mirror film grown for 300 ALD cycles are 220 ± 33 nm as shown in figure 42. The cleaved edge of the sample exhibited an estimated root mean square (RMS) roughness of 30 nm and a maximum observed peak-to-valley measurement of 757 nm. The selection of the underlayer material was carefully considered because gold has the potential to form intermetallic compounds with other metals [108], and it can make Al on gold thin film sometimes acting as an insulating film. In this study, a very thin titanium film was chosen as the conductive underlayer of the source of the electron.

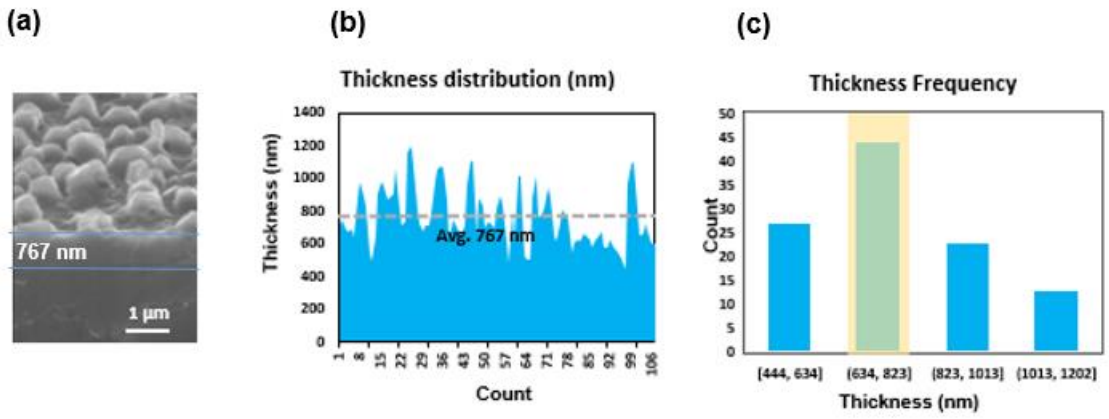

Figure 41: white thin film surface morphology analysis (a) SEM image, (b) average thickness, and (c) thickness frequency.

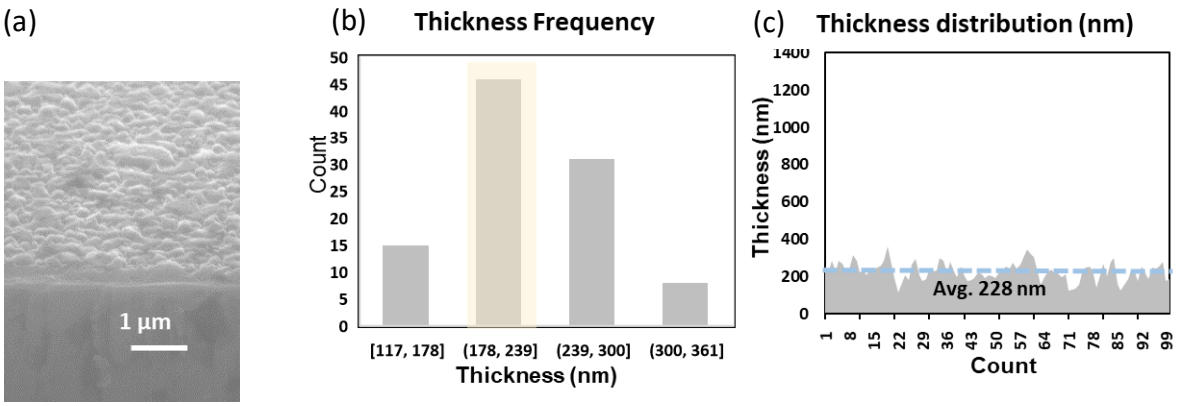

Figure 42: mrrior thin film surface morphology analysis (a) SEM image, and (b) average thickness, (c) thickness frequency.

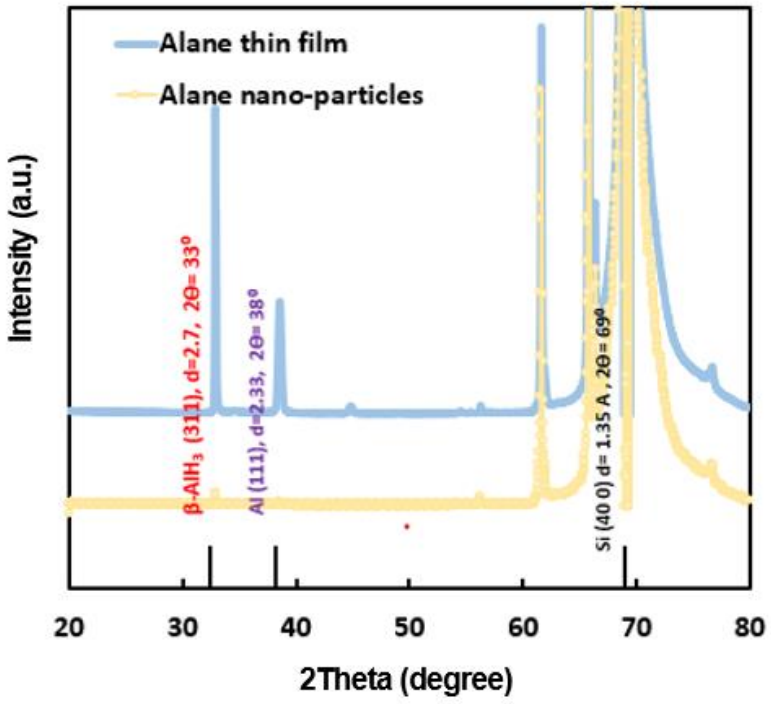

Figure 43: XRD analysis shows the B-alane texture of (311) orientation at 2Θ = 33º for both the thin film and nano-grains along with stacked lines of the standard reference at the bottom, the peak at 2Θ = 69 degrees represents the Si (400) orientation of the substrate.

XRD measurements confirm that the beta phase of the alane film has (311) orientation with a peak of 2Θ = 33◦ [109] as shown in figure 43. The peak observed at 2Θ = 69° corresponds to the Si (400) orientation of the substrate.

Further analysis was conducted to extract crystal structure information about the grown thin film by examining the XRD peak of B-alane (311) at 2Θ = 33°. The full width at half maximum (FWHM) value was determined to be 0.085°, allowing the calculation of the plane distance of the grown alane (311) thin film, which was found to be 0.27 nm. Additionally, the mean grain size of the aluminum thin film was estimated to be 108 nm using the Scherrer equation: (4-1)

Table (2) shows a comprehensive comparison of the crystal structures between the alane thin film and nanoparticles, including details such as the elemental composition of alane/aluminum.

Table 2: XRD peak analysis examining crystal structure information, B-alane thin film, and nanoparticles.

XRD peak analysis	2Θ(deg)		Height (CPS)		Composition		FMHW (degree)		crystallite size (Dc) nm		Lattice distance A^0	
	AlH3	Al	AlH3	Al	Al Ratio	AlH3 Ratio	AlH3	Al	AlH3	Al	AlH3	Al
Alane thin film	33	39	49276	13716	0.2	0.8	0.085	0.3	108	29	2.7	2.3
Alane nanoparticles	33	N/A	2030	N/A	0.0	1.0	0.053	N/A	173	N/A	2.7	N/A

Based on our findings, we propose a hypothesis stating that the presence of a conductive electron source is necessary to initiate the nucleation and growth of B-alane thin film. In the context of our thin film growth experiment, we observed that Titanium served as the initial

electron source. Subsequently, the self-assembled alane atoms on the surface continued to grow by adsorbing additional (DMEAA), which follows the proposed theoretical pathway of the reaction mechanism. The dissociation process of DMEAA initiates by removing the amine ligand, as shown in equation (1), followed by the desorption of the DMEA ligand, as illustrated in equation (2).

The reactions involved in the adsorption pathway can be described as follows:

$$C_2H_5(CH_3)_2NAlH_3\ (g) \longrightarrow AlH_3(ads) + C_2H_5(CH_3)_2N\ (ads) \quad \textbf{(1)}$$

$$C_2H_5(CH_3)_2\ N\ (ads) \longrightarrow C_2H_5(CH_3)_2N\ (g) \quad \textbf{(2)}$$

The described reaction mechanism is concluded from the analysis of the reactant gases supplied and the examination of the resulting products, as observed through XRD analysis.

The findings presented in this study provide an opportunity for the controlled growth of a well-oriented thin film of alane, specifically in the (311) orientation, which holds significant promise for various applications. This selective area growth of alane thin films holds particular relevance for energy-related applications technologies, where high hydrogen storage capacity and energy efficiency are crucial factors.

3.5. Conclusions

The results and discussion presented in this chapter are summarized as follows. Growth of aluminum films by DMEAA needs to have a metallic underlayer and we used very thin. Without a metallic underlayer, only Al nano-grains were obtained on the Si substrate, while the presence of a Ti underlayer resulted in a mirror-like smooth surface of the Al thin film. It is speculated that Ti provides electrons to AIH_3 in a mechanism similar to the

decomposition of AlH_3 by titanium (IV) isopropoxide. XRD measurements indicate that the Al film with a Ti seed layer on the Si substrate exhibits a preferred (111) orientation, which is ideal for high resistance to stress migration and longer lifetime as an electrode in device applications. Further analysis of the XRD peak of Al (111) revealed a mean grain size of 32 nm. However, non-uniform gas flow during the growth process resulted in surface roughness with mirror and white parts, with the white part containing beta-alane (β-AlH_3) contamination. The existence of AlH_3 on the surface contributed to the increased grain size and roughness, potentially due to Stranski-Krastanow growth mechanism. Additional XRD analysis showed the dominance of β-AlH_3 contamination with (311) orientation. The choice of a thin Ti film as the underlayer was preferred over gold due to potential intermetallic compound formation with Al. Overall, these findings provide insights into the growth behavior and crystal structure of Al thin films on Si substrates with a Ti underlayer, which could be relevant for various device applications.

We were able to grow alane (AlH_3) of beta phase with (311) orientation using ALD technology, with DMEAA as the main precursor, on a conductive layer. Regardless of the substrate materials, a rough alane thin film with a strong (311) texture was obtained by using a titanium underlayer. The growth of B-AlH_3 occurred through the dissociation of the DMEAA precursor. The crystal structure and morphology of the grown thin film were investigated using SEM and XRD. The deposition of an alane thin film plays an innovative role in advancing hydrogen storage technologies and energy-related applications.

4. Superconducting properties of aluminum thin films by ALD

4.1. Introduction

Superconductivity is a phenomenon observed in certain materials where their electrical resistance drops to zero when they are cooled to a certain critical temperature. This critical temperature, also known as the superconducting transition temperature (Tc), varies depending on the material and the conditions under which it is prepared.

In recent years, there has been growing interest in the use of thin films of superconducting materials for various applications, such as in the development of high-performance electronic devices, quantum computing, and energy storage. One material that has shown promise as a superconductor in thin film form is aluminum (Al).

Atomic layer deposition (ALD) is a thin-film deposition technique that allows for precise control over the thickness and composition of the deposited films. Aluminum films are deposited by various method s, and its Tc values ranging from about 1.2 to 1.7 Kelvin.

One of the key properties of superconducting aluminum thin films prepared by ALD is their crystal structure or grain boundaries. The ALD process using DMEAA precursor can produce films with extremely low impurity levels.

Another important property of superconducting aluminum thin films is their surface morphology and flatness, which is necessary for their integration into devices and for their long-term performance. ALD-grown aluminum oxide films have been shown to exhibit good mechanical stability, with low levels of strain and defects [110, 111].

Superconducting thin films prepared by ALD also exhibit high surface-to-volume ratios, which can be advantageous for applications such as sensors and catalysis. The high surface area of the films can enhance their sensitivity and reactivity, making them useful for a wide range of applications beyond superconductivity. One of the main advantages of using ALD for fabricating superconducting aluminum thin films is that the deposition process can be precisely controlled, enabling researchers to fine-tune the growth conditions to achieve the desired superconducting properties.

Other studies have focused on optimizing the ALD process parameters to achieve high-quality superconducting thin films. For example, one study investigated the effect of the precursor exposure time and pulse duration on the superconducting properties of thin films deposited by ALD [112].

In summary, the literature suggests that superconducting aluminum thin films can be successfully fabricated using ALD. The superconducting properties of these films can be optimized by controlling the deposition temperature, precursor choice, substrate temperature, and post-deposition annealing conditions. Further optimization of the ALD process parameters could lead to the fabrication of even higher-quality aluminum thin films with improved superconducting properties.

4.2. Experimental properties of aluminum thin films

The superconducting properties of aluminum thin films by ALD growth with DMEAA, can gives the ideal aluminum films as the same as the bulk aluminum. Figure 44 shows the temperature and magnetic field dependence of the aluminum film with the thickness of 110 nm. The onset of the superconducting transition temperature is 1.18 K which is very close to the bulk value, 1.19 K [113]. It is well known that thin aluminum films show the enhancement of superconductivity due to either impurity effects [114] or phonon softening [115, 116].

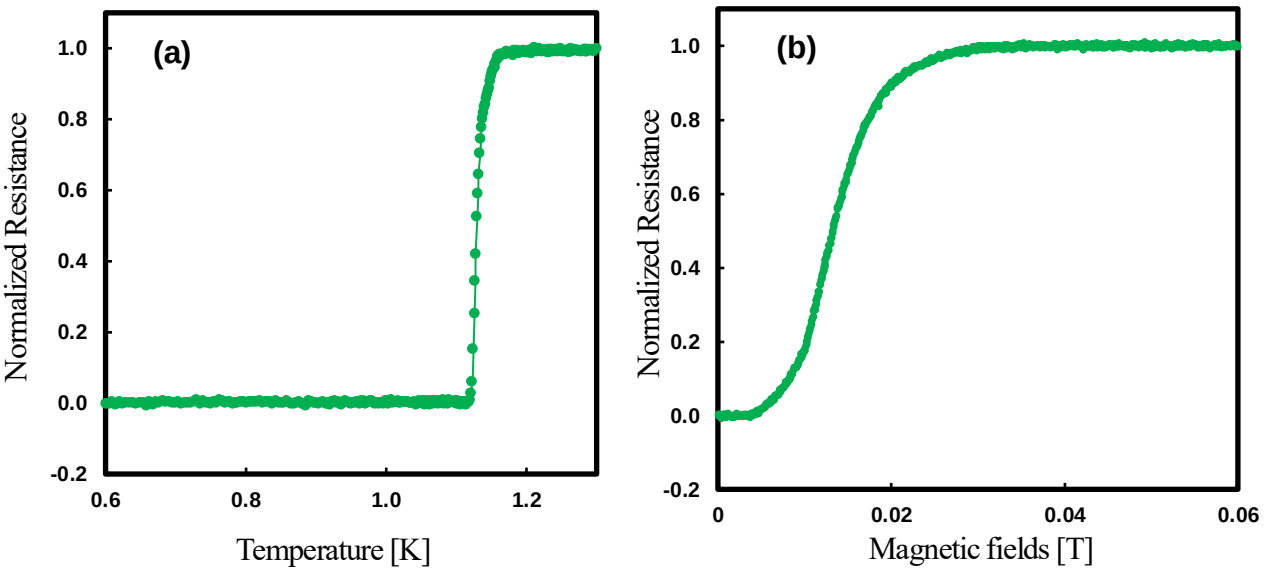

Figure 44: (a) The temperature dependence with zero magnetic fields and (b) the magnetic field dependence with T= 0.3 K of the aluminum film with the thickness of 110 nm, the resistance is normalized. Excerpt from the reference [104].

As measured by XRD, the (111) plane distance of 0.233 nm for the grown aluminum thin film Al (111) plane distance of the Al thin film is almost same as that of 0.234 nm for bulk aluminum [117]. These suggest that grown Al films are expected to be pure and ideal for device. However, the magnetic field dependence of the aluminum film at 0.3 K shows rather a broad transition although aluminum is a type I superconductor, which implies that the distribution of aluminum grains may play a role [118].

4.3. Possible applications to superconducting qubits

As we already pointed out, aluminum film only grows onto the metallic layer, not on the bare silicon substrate. This gives the area-selective growth of aluminum thin film defined by a Ti seed layer and it is very useful for fabricating superconducting small Josephson tunnel junctions, which have the nominal area less than 100 x 100 nm^2. Current standard fabrication of small Josephson tunnel junctions uses the shadow evaporation technique with a suspended bridge [119]. In current available technologies to fabricate stacked small Josephson, the suspended bridge technique is only the way to fabricate small Josephson tunnel junctions, there are no way to make such junctions without any damages and the suspended bridge technique leaves unnecessary patterns due to the pattern shift [120] and it makes difficult to fabricate large integrated circuits of small tunnel JJs. Our findings of the area-selective growth of aluminum thin films may enable us to fabricate the self-aligned vertical type of small Josephson tunnel junctions and contribute to a way of making superconducting quantum circuits, such as superconducting quantum bits.

Our research indicates that utilizing atomic layer deposition (ALD) growth using DMEAA results in aluminum thin films that possess superconducting characteristics closely mirroring

those found in bulk aluminum. These findings carry significant implications for the creation of superconducting devices and quantum circuits, potentially propelling the advancement of the realm of superconducting electronics and quantum computing. The quantum bits (qubits) composed of Josephson junctions play a pivotal role in the progress of quantum computing and the processing of quantum information. They facilitate the achievement of quantum coherence, a crucial element for constructing a quantum computer capable of surpassing classical binary computers. Technologies centered around Josephson junctions (JJ), such as Superconducting Quantum Interference Devices (SQUIDs) and single Cooper boxes, have been employed to investigate large-scale quantum tunneling and coherence phenomena at the macroscopic level.

Despite successfully demonstrating small JJ-based quantum computers, the realization of extensive quantum computing involving hundreds of qubits remains a formidable challenge, largely due to complications related to qubit entanglement and fabrication. Nevertheless, substantial strides have been taken in JJ-based technologies, and ongoing research in this domain is progressing rapidly. Superconducting qubits boast distinct attributes like macroscopic quantum effects, versatile fabrication options, and prolonged coherence periods, rendering them highly appealing for various qubit applications. As materials science, device engineering, and quantum error correction techniques continue to advance, qubits based on Josephson junctions hold the potential to fulfill the vision of achieving scalable and fault-tolerant quantum computers.

4.4. Conclusions

Superconductivity is a fascinating phenomenon characterized by zero electrical resistance at low temperatures, has garnered significant attention in recent years due to its potential applications in various fields. Thin films of superconducting materials, particularly aluminum, have emerged as promising candidates for a wide range of technologies, from high-performance electronics to quantum computing and energy storage.

The use of ALD has proven instrumental in the precise fabrication of these superconducting aluminum thin films. ALD enables control the film thickness, composition, and crystal structure, which are essential factors in achieving high superconducting critical current densities and minimal electrical energy dissipation. Furthermore, the utilization of the DMEAA precursor in the ALD process has demonstrated the ability to produce films with exceptionally low impurity levels, preserving the material's superconducting properties. The superconducting properties of aluminum thin films grown using ALD with the DMEAA precursor have been found to match the characteristics of bulk aluminum. The onset of the superconducting transition temperature for these films is remarkably to the bulk value, indicating their high purity and ideal thin film quality. This suggests that ALD-grown aluminum films exhibit enhanced superconductivity, potentially attributed to factors like impurity effects or phonon softening. This has significant implications for superconducting devices and quantum circuits, driving progress in superconducting electronics and quantum computing.

Josephson junctions (JJs) are pivotal for quantum computing, enabling quantum bits (qubits) and quantum coherence. While challenges remain for large-scale quantum computing, JJ-

based technologies are advancing rapidly, offering macroscopic quantum effects, versatile fabrication, and extended coherence periods. As materials and techniques improve, Josephson junction-based qubits hold promise for scalable and fault-tolerant quantum computers. Our research contributes to this evolving field, fostering the development of transformative quantum technologies.

5. Aluminum nanoparticles by ALD

5.1. Introduction

Atomic layer deposition (ALD) is a technology to deposit conformal oxide and nitride thin films with the film's thickness being determined by the number of reaction cycles due to its self-limiting reaction growth mechanism. Therefore, the main advantage of ALD processes is that it gives atomic-scale control of the growth[1,89,90]. This technique can also be used to produce thin metallic films. In most cases, metal film growth by ALD does not have a self-limiting mechanism, but the growth conditions can be tuned in order to obtain a single atomic layer of metal per cycle [1, 87, 88]

Dimethylethylamine alane [DMEAA; AlH_3: $N(CH_3)_2(CH_2CH_3)$] has been used successfully as an aluminum source and we produced the aluminum (111) thin film on a silicon (Si) substrate [104]. A conductive layer on a (Si) substrate is needed as a surface modification to produce aluminum thin films by DMEAA, however, there is no such ALD process to produce aluminum nanoparticles. There is a significant interest in the growth of plasmonic metal nanoparticles [121–127], and in particular, aluminum nanoparticles, as they have many applications such as high-performance energy materials [128], chromaticity devices such as flat panel displays [129], and nanosensing applications [130–134].

In this study, we produce and control the growth of aluminum nanoparticles by passivating and introducing trimethylaluminum (TMA) as an initiator before the main ALD growth process. DMEAA remains the main precursor of aluminum for the process

under conditions that imitate a self-limiting growth mechanism per cycle. We designed three different experiments with different cycles of TMA and DMEAA to investigate the particle size distribution, orientation on the substrate, and morphology. The orientation of aluminum nanoparticles was characterized by X-ray diffraction (XRD), while the crystallinity information was calculated using the integrated XRD apparatus software. A field emission scanning electron microscope (FESEM) was used to characterize the surface morphology and size of the grown nanoparticles [19–21]. Particle size image processing was analyzed using both GATAN and ImageJ software, which later is popular tool for SEM image analysis with common features for contrast adjustments and noise reduction techniques. This approach allowed the confirmation of results obtained from each software tool, as both enable users to extract valuable information from SEM images, including thickness and particle size analysis. The resulting SEM images showed the self-assembling of the aluminum atoms from tetrahedrons to octahedrons.

5.2. Growth methods

Materials and the growth process as follows: The atomic layer deposition chamber (SUNALE R-150, Picosun Oy.) was integrated with the glovebox covering the top of the chamber was used to grow aluminum as shown in figure 45(a). The glovebox is filled with pure nitrogen to prevent the oxidation of the samples before loading them into the ALD chamber. The concentration of the residual oxygen in the glovebox was controlled to be less than 0.1 ppm.

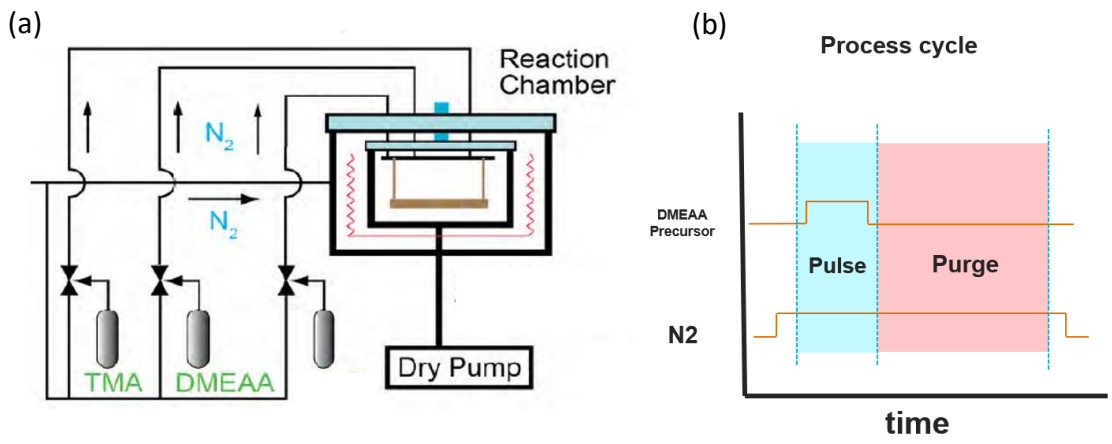

Figure 45: (a) schematic illustration of the atomic layer deposition chamber, and (b) process cycle of aluminum nanoparticles growth. Excerpt from the reference [135].

DMEAA precursor is decomposed into alane (AlH_3) at about 150 degrees Celsius [10–12], and it can be absorbed onto the Si substrate. Hydrogen reduction from alane occurs to initiate aluminum growth on the Si substrate. ALD growth process is based on surface reaction, which is the main difference from the gas-phase reaction in CVD. Our strategy to control the morphology growth is through modifying surface conditions. So, we used TMA as a passivation agent on the Si surface that was absorbed by OH^- groups, then we start pulsing the main precursor (DMEAA) to the ALD chamber, which led to obtaining aluminum nanoparticles with a well-defined orientation.

Si substrates are prepared and cleaned by wet processes. The first step is a standard degreasing process using acetone and isopropanol. In the second step, Si substrates are dipped into SEMICO Clean 23 for two minutes [101] containing tetramethylammonium hydroxide aqueous solution to eliminate the contaminations and then rinsed in pure water. Finally, as a hydroxyl group (-OH) source, ethanol is sprayed onto Si substrates and dried

up by a nitrogen blow gun. Then, the cleaned Si substrates are immediately loaded into the glovebox.

For our process, we demonstrate the capability to grow the aluminum nanoparticles by utilizing specific machine and experimental parameters. We defined the process parameters of the deposition cycle as the total time of pulse and purge as follows: the valve pulse time(t_{pulse}) and purging time (t_{purge}) as shown in figure 45(b), which were used to manage the cycles of the TMA and DMEAA. While the chamber temperature (T) was used as the growth temperature. The cycles of TMA, and DMEAA, were used to control the number of monolayers (ML) instead of the convenient self-limiting process of ALD. The hot wall, equipped with the ALD chamber, maintained a growth temperature of 150 °C. We designed three experiments to study the effects of the TMA and DMEAA cycles and they are as follows:

1. Experiment (A) TMA had 20 cycles, while DMEAA has 200 cycles
2. Experiment (B) H_2O had 20 cycles, while DMEAA has 200 cycles
3. Experiment (C) TMA had 20 cycles, while DMEAA has 400 cycles
4. Experiment (D) TMA had 10 cycles, while DMEAA has 300 cycles

The initial stage's growth parameters of TMA, t_{pulse} and t_{purge} are 0.1 seconds and 3.0 seconds, respectively. Simultaneously, t_{pulse} and t_{purge} at the second stage of DMEAA were 0.3 and 3.0 seconds, respectively. The flow rate of the carrier gas, N_2 for TMA and DMEAA is set to be 150 and 100 sccm, respectively.

5.3. Characterizations of aluminum nanoparticles

The characterizations of the nanoparticles' crystallinity were carried out by an XRD machine (Rigaku TTR-II), which is equipped with an X-ray source of Cu Kα=1.5406 Å. The scan step and scan time are selected carefully as 0.02 degree and 2 degree/min., respectively, using the continuous mode with machine power of 50 kV and 300 mA to maximize the XRD peaks of the nanoparticles. The crystallinity information was calculated using the integrated XRD apparatus software. FESEM (JEOL JSM-6340F) was used to characterize the surface morphology of the grown nanoparticles and the particle size is measured by using a microscope image processing of GATAN software [136–138].

- **Results & Discussion**

Nanoparticles were self-assembled on the Si substrate after surface modifications explained in the last section. SEM images show the morphology of the isolated nanoparticle, as shown in figure 46 (a), (b), (c), and (d) as a tetrahedron, polyhedron, and octahedron, respectively.

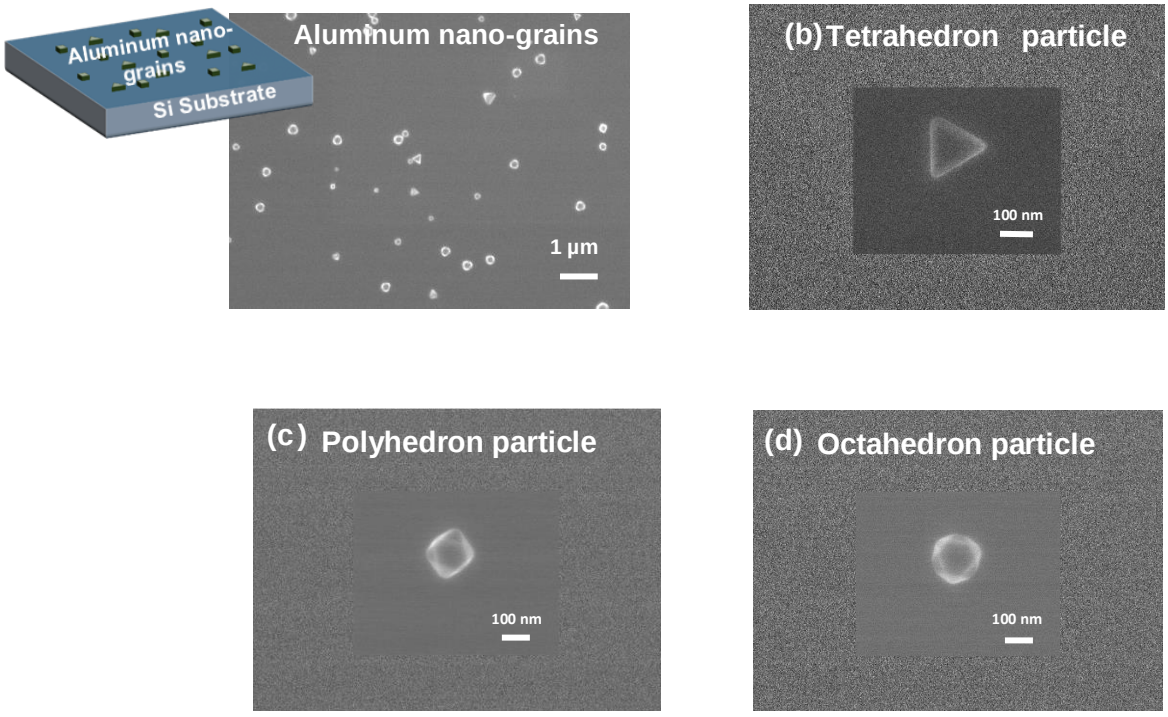

Figure 46: SEM images of (a) aluminum nanoparticles, (b) single-particle of tetrahedron morphology, (c) single-particle of polyhedron morphology, and (d) single-particle of octahedron morphology. Excerpt from the reference [104, 135].

XRD measurements show that aluminum nanoparticles produced by (a), (c), and (d) conditions have a peak of $2\Theta = 38.5°$ as shown in figure 47, which indicates (111) orientation [106, 139].

Besides, the substrate's Si (100) orientation has a peak of $2\Theta = 69°$ with their derived characteristic peaks in between 60 ° – 70 °. It was found that the highest peak of aluminum particles of (111) among our experiments required TMA 20 cycles at the first stage and DMEAA 400 cycles at the second stage as shown in experiment (c).

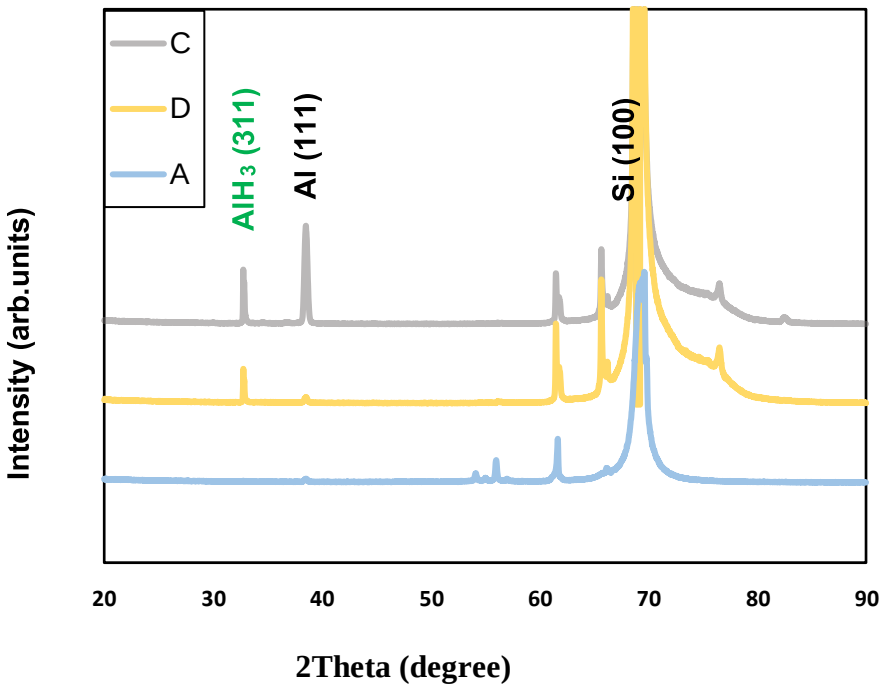

Figure 47: XRD analysis shows the aluminum nanoparticles of (111) orientation at 2Θ =38.5 º, the peak at 2Θ =69 ° represents the substrate's Si (100) orientation. Excerpt from the reference [135].

That gives the impression that (C) was the most efficient method to fabricate Al nanoparticles. alane (311) was also detected in samples (C) and (D) at the peak of 2Θ = 32 ° [140]. Further detailed analysis of the XRD peak of Al (111) at 2Θ =38.5 ° was performed to acquire the crystal information of the grown particles. The full width at half maximum (FWHM) values of the nanoparticles from experiments (A), (C), and (D) were 0.275, 0.303, and 0.261 °, respectively. The difference in the FWHM values could reflect the purity of the aluminum (111) nanoparticles. The plane distance of the grown aluminum (111) was 0.233 nm. The mean crystallite sizes of the aluminum nanoparticles of (A) and (C)&(D) were estimated to be 34, 31, and 36 nm, respectively, calculated from the Scherrer equation (4-1). Thus, the XRD peaks angles analysis confirmed the nanoparticles that appeared in the SEM images shown in Figure 46 are aluminum

nanoparticles (111). Our results lead us to theorize that to enable initiating the nucleation and the growth of aluminum nanoparticles, a conductive source of electrons is required. In our case of the aluminum nanoparticles growth, TMA associated with OH-groups were the initial source of the electron, then the self-assembled aluminum atoms on the surface keep growing by adsorbing more DMEAA in the following theoretical pathway of reaction mechanism: the chemisorption of the TMA due to the dihydrogen-bonded (DHB) [141] of the proton-transfer or H-elimination by the surface chemisorption of the TMA with (-OH) groups as shown in equation (1), So we intentionally introduced it during the cleaning process of Si-substrates as part of Lewis's acid-base complex pathway [142]. The adsorption (ads) pathway reactions are as follows:

$$(CH_4)_3Al\,(g) + OH^-(ads) \longrightarrow (CH_3)_2AlOH\,(ads) + CH_4\,(g) \qquad (1)$$

The dissociation of DMEAA starts with removing the amine ligand as in equation (2), then the ligand of DMEA desorbing in equation (3). Finally, the adsorbed molecule of TMA reacts with the adsorbed molecule of alane forming aluminum atoms and releasing methane and water from equation (4) by removing hydrogen ions from alane (AlH_3) itself. The last reaction is similar to the decomposition mechanism of alane by titanium [103,104] turning to methane [143].:

$$C_2H_5(CH_3)_2NAlH_3\,(g) \longrightarrow AlH_3(ads) + C_2H_5(CH_3)_2N\,(ads) \qquad (2)$$

$$C_2H_5(CH_3)_2\,N\,(ads) \longrightarrow C_2H_5(CH_3)_2N\,(g) \qquad (3)$$

$$AlH_3\,(ads) + (CH_3)_2AlOH\,(ads) \longrightarrow 2Al\,(s) + 2CH_4\,(g) + H_2O\,(g) \qquad (4)$$

With more cycles of DMEAA, the Ligand of the amine group keep desorbing in form of DMEA, and aluminum keeps growing as nanoparticles without oxidation [132]. That reaction mechanism is revealed from the reactant gases that we fed, and products that we analyzed by XRD.

To study the effects of TMA cycles on particle size, we measured results from the three designed experiments. The average size of the aluminum nanoparticles of (A), (C)& (D) is 130, 180 & 120 nm, respectively. From the statistical comparison of experiments (A), and (D), in the case of a high number of cycles of TMA in experiment (A), we obtained a bigger size of nanoparticle of aluminum in (A) than in (D), even though we have a higher number of the cycles of DMEAA in (D). That shows clearly the initial cycle of TMA is more crucial to controlling the size growth of the nanoparticles. After that, the cycles of DMEAA are secondary to increasing the particle size, as concluded from the experiments comparison between (A) &(C). From our investigation of particles morphology growth, we found the initial aluminum particles coalesce as tetrahedrons, as shown in figure 48(a), then grow to octahedrons in figure 48(b) then keep growing in figure 48(c), (d), and (e). The SEM images indicate that the initial texture growth of aluminum is an orientation-independent process that comes from self-nucleated crystallites during the deposition process of ALD.

The geometry of the particles changes with the accumulative deposition during aluminum growth. The reasons for polyhedron structures could be due to the atomic binding energy, fragmentation energy [144], and geometry shape stability [145]. Stating the fact that aluminum is a metal with face-centered cubic (FCC), that makes (111) planes have the most stable surface energy and preferable to be grown rather than (100) [145,146].

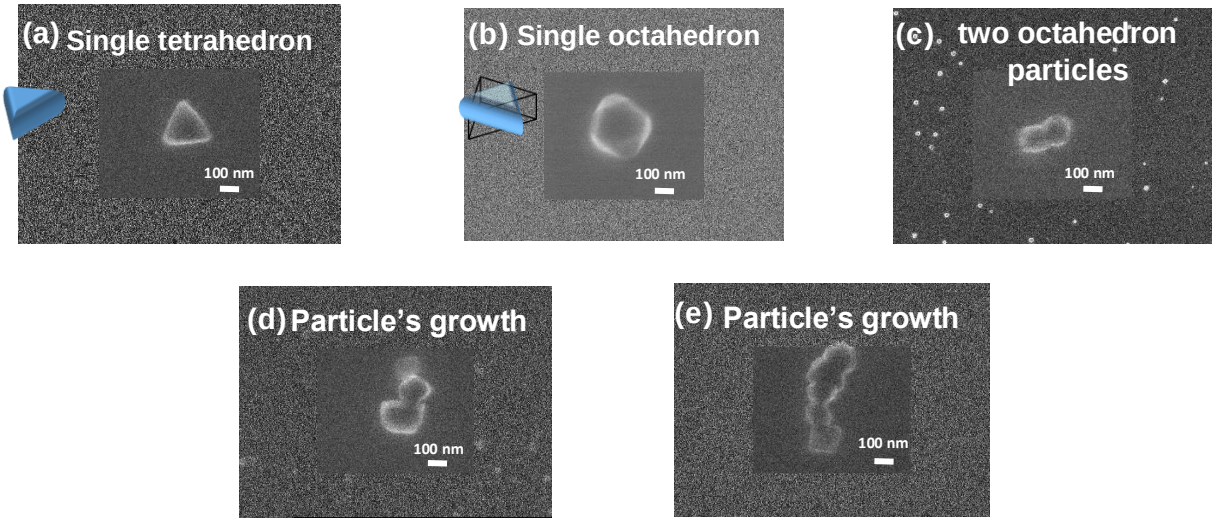

Figure 48: SEM images of aluminum crystallites growth on the bare Si substrate (a) isolated tetrahedron crystallite, (b) isolated octahedron crystallite, (c) two octahedron particles, (d), and (e) particles growth. Excerpt from the reference [135].

Our work proposes TMA is essential as an initiator to grow aluminum nanoparticles on Si-substrate in (111) orientation when using DEMAA precursor for the ALD process. The results open the door to growing plasmonic nanoparticles of aluminum in a well-defined orientation of (111) for their applications.

- **Nanoparticle Size Analysis**

nanoparticle size analysis in the context of ALD is crucial for achieving precise control over thin film properties and performance. It impacts film thickness, nucleation, growth, uniformity, surface characteristics, and interface properties. By understanding and manipulating nanoparticle sizes, researchers and engineers can optimize ALD processes and create tailored thin films for a wide range of applications in nanotechnology, electronics, optics, and beyond.

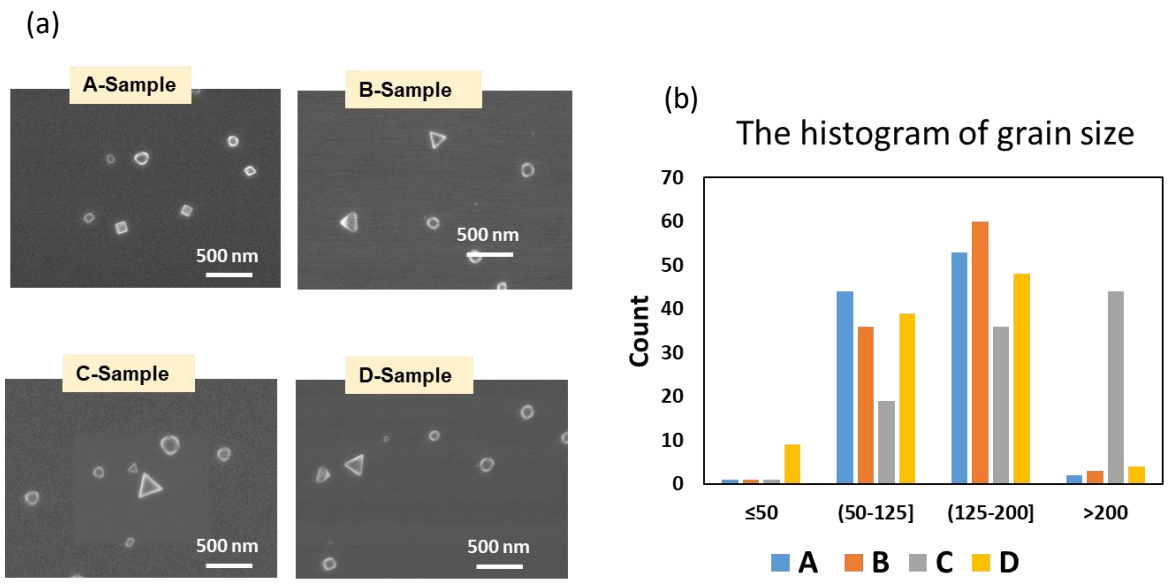

Figure 49: aluminum nanoparticles growth by the seed layer of TMA and water of samples (a) SEM images, and (b) histogram.

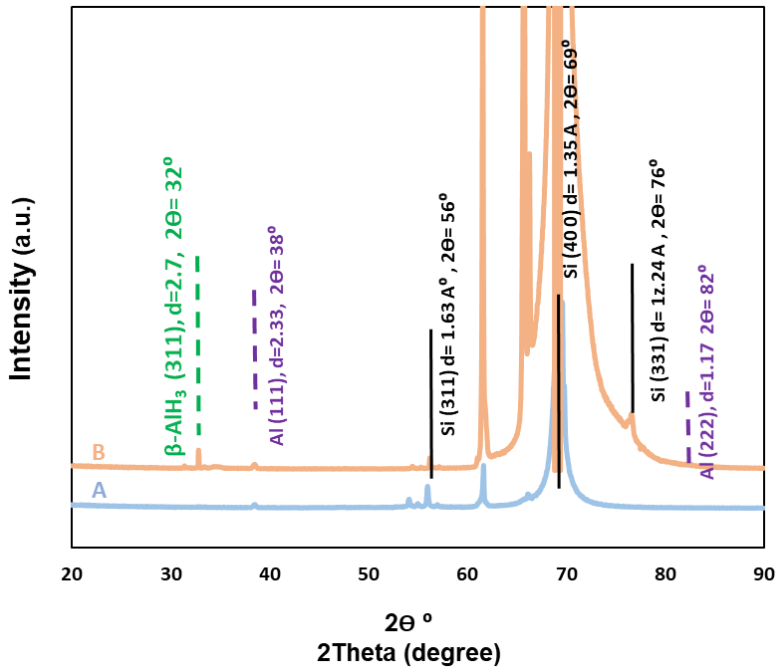

Figure 50: XRD measurements of aluminum nanoparticles A, and B samples.

It has been found that C- Sample has the biggest grain-size while D-sample has the smallest as shown in the figure 49. The average nanoparticles sizes for sample A, B, C, and D are 129, 133, 186, and 122 nm respectively. XRD measurements show that aluminum nanoparticles produced by H2O has more intensive peaks as shown in XRD figure 50 of samples A, and B.

5.4. Conclusions

Using TMA as a passivation agent, we were able to grow aluminum nanoparticles (111) by ALD technology using a DMEAA as the main precursor. The SEM images show aluminum nanoparticles have morphologies of tetrahedrons and octahedrons. The Orientation of aluminum nanoparticles of (111) is confirmed by XRD. TMA chemisorbed by OH^- groups on Si substrate surface as Lewis complex, initiates the dehydration of AlH_3 in DMEAA, enabling the assembly of aluminum nanoparticles in the (111) orientation and liberating methane. The tetrahedron (111) growth can be linked to the geometric shape and surface stability. As the growth continues, the tetrahedron aluminum nanoparticles grow to octahedrons. From our experiments and particle size analysis, the TMA cycles are more essential for growing aluminum nanoparticles and achieving bigger particle sizes than DMEAA cycles. Our well-defined orientation of plasmonic aluminum nanoparticles can be used in energy, nanosensing applications, and chromaticity devices.

6. Concluding remarks

During the research project, we obtained important findings and generated several ideas for potential applications. These findings and ideas provide valuable insights for further exploration and development in the field of aluminum thin films and nanoparticles. Here is a summary of findings:

- **The successful growth of aluminum (111) thin film by ALD**

Atomic layer deposition (ALD) is a thin-film deposition technique that offers unique advantages over other growth methods, such as the growth of conformal, uniform, and precise thickness of materials on substrates with an excellent film quality. ALD growth mechanism enables precise control over film thickness and uniformity, and it allows for the deposition of a wide range of materials, making it versatile for various applications. Surface chemistry plays a crucial role in understanding and controlling the growth of deposited thickness in ALD. Self-termination is an important requirement for optimal ALD growth, and the kinetics of adsorption and desorption reactions also affect ALD growth. The saturation of monolayer per cycle in gas-solid self-termination reactions is influenced by steric hindrance and the number of reactive sites. The steric hindrance effect is accounted for by three models, taking into account factors such as molecule size, geometry, and ligand

concentration. Understanding the surface chemistry and kinetics of ALD reactions is crucial for controlling and optimizing the growth of deposited thickness in ALD processes. Further research and experimentation are needed to fully understand and manipulate these factors for precise ALD growth in various applications.

Our work describes the process of growing aluminum thin films in a thermal atomic layer deposition (ALD) chamber equipped with a glovebox to prevent exposure to oxygen. DMEAA is used as the precursor for aluminum growth due to its stable viscosity, while silicon substrates are used with a metallic underlayer of titanium for smooth surface deposition. The growth of aluminum from DMEAA is not self-limited, and the thickness of the aluminum film can be controlled by adjusting the valve opening time, purging time, and growth temperature. The thickness and surface morphology of the aluminum film are characterized using field emission scanning electron microscopy (SEM), and X-ray diffraction (XRD) is used to determine composition and crystal orientation. Finally, resistance measurements are performed in a 0.3 K refrigerator with a 3T superconducting magnet, with temperature measured by a ruthenium oxide thermometer located at the sample stage. The study investigated the growth and morphology of aluminum (Al) thin films on a silicon (Si) substrate with and without a titanium (Ti) underlayer. The results showed that the presence of a Ti underlayer resulted in a mirror-like smooth surface of the Al thin film with a preferred (111) orientation, which is ideal for high resistance to stress migration and longer

lifetime as an electrode in device applications. However, non-uniform gas flow during the growth process resulted in surface roughness with mirror and white parts, with the white part containing beta-alane (β-AlH_3) contamination. The existence of AlH_3 on the surface contributed to the increased grain size and roughness. Additional XRD analysis showed the dominance of β-AlH_3 contamination with (311) orientation. The study concludes that the use of a thin Ti film as the underlayer could be relevant for various device applications, providing insights into the growth behavior and crystal structure of Al thin films on Si substrates.

- **The successful growth of aluminum (111) nanoparticles by ALD**

Our study demonstrates the successful growth of aluminum nanoparticles (111) using atomic layer deposition (ALD) technology with dimethylethylamine alane (DMEAA) as the main precursor and trimethylaluminum (TMA) as a passivation agent. The SEM images reveal that the aluminum nanoparticles have tetrahedral and octahedral morphologies, and XRD confirms their (111) orientation. The use of TMA as a Lewis complex on the Si substrate surface initiates the dehydration of AlH_3 in DMEAA, enabling the assembly of aluminum nanoparticles in the (111) orientation and releasing methane. The growth of tetrahedral aluminum nanoparticles is linked to their geometric shape and surface stability, and they

subsequently grow into octahedral nanoparticles as the growth continues. The particle size analysis indicates that the TMA cycles are more crucial for achieving bigger particle sizes than the DMEAA cycles. The results of this study suggest that the well-defined orientation of plasmonic aluminum nanoparticles could be useful in energy, nanosensing applications, and chromaticity devices.

- **Unique superconducting properties of ALD aluminum thin films**

Our study examines the superconducting properties of aluminum thin films grown using atomic layer deposition (ALD) with dimethylethylamine alane (DMEAA) as compared to films grown by electron beam evaporation (E-gun) and sputtering techniques. The results find that ALD growth produces aluminum films with superconducting properties comparable to bulk aluminum.

The experimental results, as depicted in Figure 54, demonstrate the temperature and magnetic field dependence of an ALD-grown aluminum film with a thickness of 110 nm. The onset of the superconducting transition temperature for the film is measured to be 1.18 K, which closely aligns with the bulk value of 1.19 K. This indicates that the ALD-grown aluminum film retains the desired superconducting characteristics.

The work also investigates the purity and crystalline structure of the ALD-grown aluminum films. X-ray diffraction (XRD) analysis reveals that the (111) plane distance of the aluminum film is almost identical to that of bulk aluminum, indicating a high level of purity. These findings suggest that the ALD process enables the production of very pure and ideal aluminum thin films.

However, the magnetic field dependence of the aluminum film at 0.3 K exhibits a relatively broad transition, despite aluminum being classified as a type I superconductor. This broadening suggests that the distribution of aluminum grains in the film may have an influence on the superconducting behavior.

One notable advantage of ALD growth is the selective deposition of aluminum onto a metallic layer, rather than directly onto the silicon substrate. This selectivity allows for the fabrication of superconducting small Josephson tunnel junctions with areas smaller than 100 x 100 nm^2. Traditionally, the shadow evaporation technique with a suspended bridge has been employed for fabricating such junctions. However, this technique can result in pattern shift issues and limitations in scaling up the fabrication process. The selective area growth of aluminum thin films using ALD presents a promising alternative, enabling the fabrication of self-aligned vertical small Josephson tunnel junctions and facilitating the development of superconducting quantum circuits, including superconducting quantum bits.

- **Potential application of aluminum thin films as a component for qubits**

The study suggests that ALD growth with DMEAA yields aluminum thin films with superconducting properties closely resembling those of bulk aluminum. These findings have implications for the fabrication of superconducting devices and quantum circuits, potentially advancing the field of superconducting electronics and quantum computing. The quantum bit of Josephson junctions are critical components in the development of quantum computing and quantum information processing. They enable the realization of quantum coherence, which is essential for building a quantum computer that can outperform classical binary

computers. JJ-based technologies, such as single Cooper box and Superconducting Quantum Interference Devices (SQUIDs), have been used to study macroscopic quantum tunneling and macroscopic quantum coherence. Despite the successful demonstration of small-scale JJ-based quantum computers, achieving large-scale quantum computing with hundreds of qubits remains challenging due to issues such as qubit entanglement. However, significant progress has been made in JJ-based technologies, and research in this field continues to grow rapidly. JJ-based qubits have unique properties, such as macroscopic quantum phenomena, fabrication flexibility, and long coherence times, which make them attractive for qubit applications. To overcome challenges related to qubit coherence time and two-qubit gate fidelity, researchers are exploring various techniques, such as advanced fabrication methods, error-correction codes, and novel qubit designs. With continued advancements in materials science, device engineering, and quantum error correction techniques, Josephson junction-based qubits hold promise for the realization of scalable and fault-tolerant quantum computers.

- **Potential application of aluminum nanoparticles**

Aluminum nanoparticles have various potential applications across different fields. Some of the possible applications of Al nanoparticles include catalysis, energy storage, aerospace industry, electronics, photovoltaics, and surface coatings as following:

- Catalysis: Aluminum nanoparticles can act as catalysts in various chemical reactions due to their high surface area and reactivity. They can be used in hydrogenation reactions, organic synthesis, and pollutant degradation processes.

- Energy storage: Aluminum nanoparticles can be utilized in energy storage devices, such as batteries and supercapacitors. They can enhance the performance and efficiency of these systems by improving charge/discharge rates and increasing energy density.
- Aerospace industry: Aluminum nanoparticles can be incorporated into aerospace materials, such as coatings and composites, to enhance their mechanical and thermal properties. They can improve the strength, toughness, and heat resistance of aircraft components.
- Electronics: Aluminum nanoparticles can be employed in electronic devices and circuitry. They can be used in conductive inks, transparent conductive films, and as additives in electronic pastes to enhance electrical conductivity and performance.
- Photovoltaics: Aluminum nanoparticles can be utilized in solar cells and photovoltaic devices. They can improve light absorption, increase the efficiency of energy conversion, and enhance the stability of solar cell materials.
- Surface coatings: Aluminum nanoparticles can be incorporated into coatings for various purposes, including corrosion protection, antimicrobial properties, and UV protection. They can enhance the durability and functionality of coatings in different industries.

Acknowledgements

I want to express my sincere gratitude to my supervisor at Kyushu University, Prof. Yuichi Harada, for his kind support, encouragement, guidance, and for affording me the opportunity to pursue my Ph.D. degree in his laboratory at the Molecular and Material Science Department, Interdisciplinary Graduate School of Engineering Sciences faculty.

I extend my gratitude to the staff Ms. Kanako Shibata, Ms. Kano, and teachers of the Green Asia program office for their valuable advice and financial support, which greatly aided me in meeting the requirements of my doctoral course.

I am appreciative of the researchers at Nippon Telegraph and Telephone Basic Research Laboratories (NTT-BRL) – Dr. Satoshi Sasaki and Dr. Yoshiaki Sekine – for granting an access to NTT facilities and for their support in the publication of my research.

Last but certainly not least, I would like to express my heartfelt thanks to my family and friends for their understanding throughout this journey.

The doctoral course is comprised of the master's course. Prof. Harada's lab extends gratitude to Prof. Tsuyoshi Yanagida and others. Also, we express gratitude to Prof. Eljamal and Prof. Kazuki Nagashima, who is now a professor at Hoddaido University.

Sameh Okasha

References

[1] R.L. Puurunen, Surface chemistry of atomic layer deposition: A case study for the trimethylaluminum/water process, J. Appl. Phys. 97 (2005) 1–52. https://doi.org/10.1063/1.1940727.

[2] S.A. Rackley, Adsorption Capture Systems, Carbon Capture and Storage. (2010) 133–157. https://doi.org/10.1016/B978-1-85617-636-1.00007-9.

[3] O. Sneh, R.B. Clark-Phelps, A.R. Londergan, J. Winkler, T.E. Seidel, Thin film atomic layer deposition equipment for semiconductor processing, 2002.

[4] H. Kumagai, M. Matsumoto, Y. Kawamura, K. Toyoda, M. Obara, Fabrication of multilayers with growth controlled by sequential surface chemical reactions, Jpn J. Appl. Phys. 33 (1994) 708–709. https://doi.org/10.1143/JJAP.33.7086.

[5] H.C. Guo, E. Ye, Z. Li, M.Y. Han, X.J. Loh, Recent progress of atomic layer deposition on polymeric materials, Materials Science and Engineering C. 70 (2017) 1182–1191. https://doi.org/10.1016/j.msec.2016.01.093.

[6] M. Ritala', M. Leskela, E. Rauhala, Atomic Layer Epitaxy Growth of Titanium Dioxide Thin Films from Titanium Ethoxide, 1994.

[7] M. Ritala', M. Leskelii, L. Niinist6, P. Haussalo, Titanium Isopropoxide as a Precursor in Atomic Layer Epitaxy of Titanium Dioxide Thin Films, 1993.

[8] M. Ylilammi, Monolayer thickness in atomic layer deposition, 1996.

[9] H. Siimon, J. Aarik, Thickness profiles of thin films caused by secondary reactions in flow-type atomic layer deposition reactors, J. Phys. D. Appl. Phys. 30 (1997) 1725–1728. https://doi.org/10.1088/0022-3727/30/12/006.

[10] R.L. Puurunen, Growth Per Cycle in Atomic Layer Deposition: A Theoretical Model, Chemical Vapor Deposition. 9 (2003) 249–257. https://doi.org/10.1002/CVDE.200306265.

[11] R.L. Puurunen, W. Vandervorst, Island growth as a growth mode in atomic layer deposition: A phenomenological model, J. Appl. Phys. 96 (2004) 7686–7695. https://doi.org/10.1063/1.1810193.

[12] X. pan Qiu, X. Liu, S. ming Jiang, G. rui Jiang, Q. fu Zhang, Growth mechanism for zinc coatings deposited by vacuum thermal evaporation, Journal of Iron and Steel Research International. 28 (2021) 1047–1053. https://doi.org/10.1007/S42243-020-00519-5/METRICS.

[13] K.J. Bachmann, Epitaxy, in: Encyclopedia of Materials: Science and Technology, Elsevier, 2001: pp. 2791–2799. https://doi.org/10.1016/b0-08-043152-6/00496-4.

[14] Epitaxy Deposition Market | Growth Factor with Key Drivers Analysis till 2027 Tokyo Electron, IQE, Applied Materials, Hitachi Kokusai Electric | Brandessence Market Research

and Consulting Pvt ltd., (n.d.). https://www.mynewsdesk.com/us/brandessence/pressreleases/epitaxy-deposition-market-growth-factor-with-key-drivers-analysis-till-2027-tokyo-electron-iqe-applied-materials-hitachi-kokusai-electric-3115560 (accessed May 26, 2022).

[15] B. Lotz, A. Thierry, Polymer Crystals: Epitaxial Growth, in: Encyclopedia of Materials: Science and Technology, Elsevier, 2001: pp. 7267–7272. https://doi.org/10.1016/b0-08-043152-6/01293-6.

[16] D.M. Mattox, Atomistic Film Growth and Some Growth-Related Film Properties, in: Handbook of Physical Vapor Deposition (PVD) Processing, Elsevier, 2010: pp. 333–398. https://doi.org/10.1016/b978-0-8155-2037-5.00010-1.

[17] S. Nishino, J.A. Powell, H.A. Will, Production of large-area single-crystal wafers of cubic SiC for semiconductor devices, Appl. Phys. Lett. 42 (1983) 460–462. https://doi.org/10.1063/1.93970.

[18] D.W. Greve, F.T. Mahi, Chemical Vapor Deposition of Group IV Alloys on Silicon, in: Reference Module in Materials Science and Materials Engineering, Elsevier, 2016. https://doi.org/10.1016/b978-0-12-803581-8.03700-0.

[19] M. Juppo, A. Rahtu, M. Ritala, M. Leskelä, In Situ Mass Spectrometry Study on Surface Reactions in Atomic Layer Deposition of Al 2 O 3 Thin Films from Trimethylaluminum and Water, (2000). https://doi.org/10.1021/la991183.

[20] A. Rahtu, T. Alaranta, M. Ritala, In situ quartz crystal microbalance and quadrupole mass spectrometry studies of atomic layer deposition of aluminum oxide from trimethylaluminum and water, Langmuir. 17 (2001) 6506–6509. https://doi.org/10.1021/la010103a.

[21] R.L. Puurunen, M. Lindblad, A. Rootc, A.O.I. Krausea, Successive reactions of gaseous trimethylaluminium and ammonia on porous alumina, Physical Chemistry Chemical Physics. 3 (2001) 1093–1102. https://doi.org/10.1039/b007249o.

[22] S.K. Lee, H.C. Oh, D.H. Kim, Y.C. Jeong, S. Bin Baek, Y.C. Kim, Regular distribution of -OH fragments on a Si (001)-c(4 × 2) surface by dissociation of water molecules, Korean Journal of Materials Research. 20 (2010) 457–462. https://doi.org/10.3740/MRSK.2010.20.9.457.

[23] Y.P. Barry Arkles, Hydrophobicity, Hydrophilicity and Silane Surface Modification, 2011.

[24] K. Shirai, Y. Yoshida, Y. Nakayama, M. Fujitani, H. Shintani, K. Wakasa, M. Okazaki, J. Snauwaert, B. Van Meerbeek, Assessment of Decontamination Methods as Pretreatment of Silanization of Composite Glass Fillers, 2000. https://doi.org/10.1002/(SICI)1097-4636(2000)53:3.

[25] N.A. Alcantar, E.S. Aydil, J. Israelachvili, EFFECT OF WATER PLASMA ON SILICA SURFACES: SYNTHESIS, CHARACTERIZATION AND APPLICATIONS, in: Fundamental and Applied Aspects of Chemically Modified Surfaces, Elsevier, 1999: pp. 212–222. https://doi.org/10.1533/9781845698591.212.

[26] H.C.M. Knoops, S.E. Potts, A.A. Bol, W.M.M. Kessels, Atomic Layer Deposition, in: Handbook of Crystal Growth: Thin Films and Epitaxy: Second Edition, Elsevier Inc., 2015: pp. 1101–1134. https://doi.org/10.1016/B978-0-444-63304-0.00027-5.

[27] G.N. Parsons, J.W. Elam, S.M. George, S. Haukka, H. Jeon, W.M.M. (Erwin) Kessels, M. Leskelä, P. Poodt, M. Ritala, S.M. Rossnagel, History of atomic layer deposition and its relationship with the American Vacuum Society, Journal of Vacuum Science & Technology A: Vacuum, Surfaces, and Films. 31 (2013) 050818. https://doi.org/10.1116/1.4816548.

[28] T. Suntola, Atomic layer epitaxy, Materials Science Reports. 4 (1989) 261–312. https://doi.org/10.1016/S0920-2307(89)80006-4.

[29] M. Ritala, M. Leskelä, Handbook of Thin Film Materials, 2002.

[30] H.B. Profijt, S.E. Potts, M.C.M. van de Sanden, W.M.M. Kessels, Plasma-Assisted Atomic Layer Deposition: Basics, Opportunities, and Challenges, Journal of Vacuum Science & Technology A: Vacuum, Surfaces, and Films. 29 (2011) 050801. https://doi.org/10.1116/1.3609974.

[31] H.C.M. Knoops, J.W. Elam, J.A. Libera, W.M.M. Kessels, Surface loss in ozone-based atomic layer deposition processes, Chemistry of Materials. 23 (2011) 2381–2387. https://doi.org/10.1021/cm2001144.

[32] 2D Materials: An Introduction to Two-Dimensional Materials | Ossila, (n.d.). https://www.ossila.com/pages/introduction-2d-materials (accessed July 5, 2021).

[33] ZELDOVICH, Ya. B., On the Theory of New Phase Formation : Cavitation, Acta Physicochem., USSR. 18 (1943) 1. https://ci.nii.ac.jp/naid/10011326745 (accessed July 7, 2021).

[34] V. Ruth, J.P. Hirth, G.M. Pound, On the theory of homogeneous nucleation and spinodal decomposition in condensation from the vapor phase, J. Chem. Phys. 88 (1998) 7079. https://doi.org/10.1063/1.454358.

[35] S.L. Girshick, Comment on: '"Self-consistency correction to homogeneous nucleation theory,"' J Chem Phys. 94 (1998) 826. https://doi.org/10.1063/1.460309.

[36] I.J. Ford, A. Laaksonen, M. Kulmala, Modification of the Dillmann–Meier theory of homogeneous nucleation, J. Chem. Phys. 99 (1998) 764. https://doi.org/10.1063/1.465756.

[37] J.W. Cahn, J.E. Hilliard, Free Energy of a Nonuniform System. III. Nucleation in a Two-Component Incompressible Fluid, J. Chem. Phys. 31 (2004) 688. https://doi.org/10.1063/1.1730447.

[38] R. Wu, Q. Tao, W. Dang, Y. Liu, B. Li, J. Li, B. Zhao, Z. Zhang, H. Ma, G. Sun, X. Duan, X. Duan, van der Waals Epitaxial Growth of Atomically Thin 2D Metals on Dangling-Bond-Free WSe2 and WS2, Adv. Funct. Mater. 29 (2019) 1806611. https://doi.org/10.1002/ADFM.201806611.

[39] Y. Wang, Y. Shi, G. Xin, J. Lian, J. Shi, Two-Dimensional van der Waals Epitaxy Kinetics in a Three-Dimensional Perovskite Halide, Cryst Growth Des. 15 (2015) 4741–4749. https://doi.org/10.1021/ACS.CGD.5B00949.

[40] M. Aliofkhazraei, N. Ali, Fabrication and Properties of Micro- and Nanostructured Coatings Using Electrochemical Depositions, Comprehensive Materials Processing. 7 (2014) 119–156. https://doi.org/10.1016/B978-0-08-096532-1.00707-X.

[41] H. Liu, D.S. Dandy, Effects of Surface Conditions on Diamond Nucleation, Diamond Chemical Vapor Deposition. (1995) 92–130. https://doi.org/10.1016/B978-081551380-3.50007-4.

[42] B.A. Morris, Converting Processes, The Science and Technology of Flexible Packaging. (2017) 25–49. https://doi.org/10.1016/B978-0-323-24273-8.00002-2.

[43] T. Hasegawa, Advances in device fabrication scale-up methods, Handbook of Organic Materials for Electronic and Photonic Devices, Second Edition. (2018) 579–597. https://doi.org/10.1016/B978-0-08-102284-9.00018-8.

[44] M. Leskelä, J. Niinistö, M. Ritala, Atomic Layer Deposition, in: Comprehensive Materials Processing, Elsevier Ltd, 2014: pp. 101–123. https://doi.org/10.1016/B978-0-08-096532-1.00401-5.

[45] M. Ritala, M. Leskelä, Atomic layer deposition, in: Handbook of Thin Films, Elsevier, 2002: pp. 103–159. https://doi.org/10.1016/B978-012512908-4/50005-9.

[46] M. Ritala, M. Leskelä, J.-P. Dekker, C. Mutsaers, P.J. Soininen, J. Skarp, Communications Perfectly Conformal TiN and Al 2 O 3 Films Deposited by Atomic Layer Deposition**, n.d.

[47] O. Sneh, R.B. Clark-Phelps, A.R. Londergan, J. Winkler, T.E. Seidel, Thin film atomic layer deposition equipment for semiconductor processing, Thin Solid Films. 402 (2002) 248–261. https://doi.org/10.1016/S0040-6090(01)01678-9.

[48] J. E. Green, in: R. F. Bunshah (Ed), in: Handbook of Deposition Technologies for Films and Coatings, 2nd Edition, 2nd ed., 1994: p. 681.

[49] S.S. Dana, M. Liehr, M. Anderle, G.W. Rubloff, Kinetics of nucleation and growth of Si on SiO2 in very low pressure SiH4 chemical vapor deposition, Appl. Phys. Lett. 61 (1992) 3035–3037. https://doi.org/10.1063/1.108001.

[50] L. TD, J. F, L. R, N. Y, M. C, O. JL, Quantum computers, Nature. 464 (2010) 45–53. https://doi.org/10.1038/NATURE08812.

[51] K.K. Likharev, J. Lukens, K.K. Likharev, J. Lukens, Dynamics of Josephson Junctions and Circuits, PhT. 41 (1988) 122. https://doi.org/10.1063/1.2811641.

[52] J. Weber, Quantum Theory of a Damped Electrical Oscillator and Noise, Physical Review. 90 (1953) 977. https://doi.org/10.1103/PhysRev.90.977.

[53] R.F. Voss, R.A. Webb, Macroscopic Quantum Tunneling in 1-μm Nb Josephson Junctions, Phys Rev Lett. 47 (1981) 265. https://doi.org/10.1103/PhysRevLett.47.265.

[54] A.O. Caldeira, A.J. Leggett, Influence of Dissipation on Quantum Tunneling in Macroscopic Systems, Phys. Rev. Lett. 46 (1981) 211. https://doi.org/10.1103/PhysRevLett.46.211.

[55] L.D. LANDAU, E.M. LIFSHITZ, PERTURBATION THEORY, Quantum Mechanics. (1977) 133–163. https://doi.org/10.1016/B978-0-08-020940-1.50013-X.

[56] J.M. Martinis, M.H. Devoret, J. Clarke, Experimental tests for the quantum behavior of a macroscopic degree of freedom: The phase difference across a Josephson junction, Phys Rev B. 35 (1987) 4682. https://doi.org/10.1103/PhysRevB.35.4682.

[57] G. Wendin, V.S. Shumeiko, Quantum bits with Josephson junctions (Review Article), Low Temperature Physics. 33 (2007) 724. https://doi.org/10.1063/1.2780165.

[58] B. Yurke, J.S. Denker, Quantum network theory, Phys Rev A (Coll Park). 29 (1984) 1419. https://doi.org/10.1103/PhysRevA.29.1419.

[59] S. (Serge) Reynaud, E. (Elisabeth) Giacobino, Jean. Zinn-Justin, Fluctuations quantiques : Les Houches, Session LXIII, 27 juin-28 juillet 1995 = Quantum fluctuations, (1997) 606.

[60] G. Burkard, R.H. Koch, D.P. DiVincenzo, Multilevel quantum description of decoherence in superconducting qubits, Phys Rev B. 69 (2004) 064503. https://doi.org/10.1103/PhysRevB.69.064503.

[61] N. Materise, An Introduction to Superconducting Qubits and Circuit Quantum Electrodynamics, Springer Proceedings in Physics. 211 (2018) 87–95. https://doi.org/10.1007/978-3-319-92726-8_10/COVER.

[62] M.A. Nielsen, I. Chuang, Quantum Computation and Quantum Information, Am J Phys. 70 (2002) 558. https://doi.org/10.1119/1.1463744.

[63] R.P. Feynman, Feynman Lectures on Computation, Feynman Lectures on Computation. (2018). https://doi.org/10.1201/9780429500442.

[64] A.J. Leggett, Macroscopic Quantum Tunnelling and Related Effects in Josephson Systems, Percolation, Localization, and Superconductivity. (1984) 1–41. https://doi.org/10.1007/978-1-4615-9394-2_1.

[65] A.J. Leggett, Macroscopic Quantum Systems and the Quantum Theory of Measurement, Progress of Theoretical Physics Supplement. 69 (1980) 80–100. https://doi.org/10.1143/PTP.69.80.

[66] A.J. Leggett, A. Garg, Quantum mechanics versus macroscopic realism: Is the flux there when nobody looks?, Phys. Rev. Lett. 54 (1985) 857. https://doi.org/10.1103/PhysRevLett.54.857.

[67] Y. Nakamura, Yu.A. Pashkin, J.S. Tsai, Coherent control of macroscopic quantum states in a single-Cooper-pair box, Nature 1999 398:6730. 398 (1999) 786–788. https://doi.org/10.1038/19718.

[68] A.J. Leggett, S. Chakravarty, A.T. Dorsey, M.P.A. Fisher, A. Garg, W. Zwerger, Dynamics of the dissipative two-state system, Rev. Mod. Phys. 59 (1987) 1. https://doi.org/10.1103/RevModPhys.59.1.

[69] J.M. Martinis, S. Nam, J. Aumentado, K.M. Lang, C. Urbina, Decoherence of a superconducting qubit due to bias noise, Phys. Rev. B. 67 (2003) 094510. https://doi.org/10.1103/PhysRevB.67.094510.

[70] J. CLARKE, A.N. CLELAND, M.H. DEVORET, D. ESTEVE, J.M. MARTINIS, Quantum Mechanics of a Macroscopic Variable: The Phase Difference of a Josephson Junction, Science (1979). 239 (1988) 992–997. https://doi.org/10.1126/SCIENCE.239.4843.992.

[71] J.E. Mooij, T.P. Orlando, L. Levitov, L. Tian, C.H. van der Wal, S. Lloyd, Josephson Persistent-Current Qubit, Science (1979). 285 (1999) 1036–1039. https://doi.org/10.1126/SCIENCE.285.5430.1036.

[72] C.H. van der Wal, A.C.J. ter Haar, F.K. Wilhelm, R.N. Schouten, C.J.P.M. Harmans, T.P. Orlando, S. Lloyd, J.E. Mooij, Quantum Superposition of Macroscopic Persistent-Current States, Science (1979). 290 (2000) 773–777. https://doi.org/10.1126/SCIENCE.290.5492.773.

[73] M.H. Devoret, J.M. Martinis, J. Clarke, Measurements of Macroscopic Quantum Tunneling out of the Zero-Voltage State of a Current-Biased Josephson Junction, Phys. Rev. Lett. 55 (1985) 1908. https://doi.org/10.1103/PhysRevLett.55.1908.

[74] J.R. Friedman, V. Patel, W. Chen, S.K. Tolpygo, J.E. Lukens, Quantum superposition of distinct macroscopic states, Nature 2000 406:6791. 406 (2000) 43–46. https://doi.org/10.1038/35017505.

[75] J. Claudon, F. Balestro, F.W.J. Hekking, O. Buisson, Coherent Oscillations in a Superconducting Multilevel Quantum System, Phys. Rev. Lett. 93 (2004) 187003. https://doi.org/10.1103/PhysRevLett.93.187003.

[76] Yu.A. Pashkin, T. Yamamoto, O. Astafiev, Y. Nakamura, D. V. Averin, J.S. Tsai, Quantum oscillations in two coupled charge qubits, Nature 2003 421:6925. 421 (2003) 823–826. https://doi.org/10.1038/nature01365.

[77] J.B. Majer, Superconducting Quantum Circuits, (2002). https://repository.tudelft.nl/islandora/object/uuid%3Ad326d146-73a8-4484-97de-548241b072ff (accessed July 7, 2021).

[78] A. Izmalkov, M. Grajcar, E. Il'ichev, Th. Wagner, H.-G. Meyer, A.Yu. Smirnov, M.H.S. Amin, A.M. van den Brink, A.M. Zagoskin, Evidence for Entangled States of Two Coupled Flux Qubits, Phys. Rev. Lett. 93 (2004) 037003. https://doi.org/10.1103/PhysRevLett.93.037003.

[79] J.B. Majer, F.G. Paauw, A.C.J. ter Haar, C.J.P.M. Harmans, J.E. Mooij, Spectroscopy on Two Coupled Superconducting Flux Qubits, Phys. Rev. Lett. 94 (2005) 090501. https://doi.org/10.1103/PhysRevLett.94.090501.

[80] B. AJ, X. H, R. RC, G. MA, S. FW, J. PR, A. JR, D. AJ, L. CJ, W. FC, Entangled macroscopic quantum States in two superconducting qubits, Science. 300 (2003) 1548–1550. https://doi.org/10.1126/SCIENCE.1084528.

[81] T. Yamamoto, Yu.A. Pashkin, O. Astafiev, Y. Nakamura, J.S. Tsai, Demonstration of conditional gate operation using superconducting charge qubits, Nature 2003 425:6961. 425 (2003) 941–944. https://doi.org/10.1038/nature02015.

[82] Michael. Tinkham, Introduction to superconductivity, (2004) 196–210.

[83] Y.-L. Wu, 吴玉林, H. Deng, 邓辉, H.-F. Yu, 于海峰, G.-M. Xue, 薛光明, Y. Tian, 田野, J. Li, 李洁, Y.-F. Chen, 陈莺飞, S.-P. Zhao, 赵士平, D.-N. Zheng, 郑东宁, Fabrication of Al/AlOx/Al Josephson junctions and superconducting quantum circuits by shadow evaporation and a dynamic oxidation process, Chinese Physics B. 22 (2013) 060309. https://doi.org/10.1088/1674-1056/22/6/060309.

[84] J.-P. Cleuziou, W. Wernsdorfer, V. Bouchiat, T. Ondarçuhu, M. Monthioux, Carbon nanotube superconducting quantum interference device, Nature Nanotechnology 2006 1:1. 1 (2006) 53–59. https://doi.org/10.1038/nnano.2006.54.

[85] SQUID Magnetometer and Josephson Junctions, (n.d.). http://hyperphysics.phy-astr.gsu.edu/hbase/Solids/Squid.html (accessed July 7, 2021).

[86] T.E. Roth, R. Ma, W.C. Chew, An Introduction to the Transmon Qubit for Electromagnetic Engineers, (2021). http://arxiv.org/abs/2106.11352.

[87] S. Sasaki, K. Tateno, G. Zhang, H. Pigot, Y. Harada, S. Saito, A. Fujiwara, T. Sogawa, K. Muraki, Self-aligned gate-all-around InAs/InP core-shell nanowire field-effect transistors, in: Jpn J. Appl. Phys, Japan Society of Applied Physics, 2015: p. 04DN04. https://doi.org/10.7567/JJAP.54.04DN04.

[88] H. Irie, Y. Harada, H. Sugiyama, T. Akazaki, Josephson coupling through one-dimensional ballistic channel in semiconductor-superconductor hybrid quantum point contacts, Phys Rev B Condens Matter Mater Phys. 89 (2014) 165415. https://doi.org/10.1103/PhysRevB.89.165415.

[89] K. Hirama, H. Sato, Y. Harada, H. Yamamoto, M. Kasu, Thermally stable operation of h-terminated diamond FETs by NO 2 adsorption and Al 2O 3 passivation, IEEE Electron Device Letters. 33 (2012) 1111–1113. https://doi.org/10.1109/LED.2012.2200230.

[90] S.M. George, Atomic layer deposition: An overview, Chem Rev. 110 (2010) 111–131. https://doi.org/10.1021/cr900056b.

[91] Y.J. Lee, S.-W. Kang, Study on the characteristics of alumdinum thin films prepared by atomic layer deposition, Journal of Vacuum Science & Technology A: Vacuum, Surfaces, and Films. 20 (2002) 1983. https://doi.org/10.1116/1.1513636.

[92] H. Matsuhashi, C.H. Lee, T. Nishimura, K. Masu, K. Tsubouchi, Superiority of DMAH to DMEAA for al CVD technology, Mater Sci Semicond Process. 2 (1999) 303–308. https://doi.org/10.1016/S1369-8001(99)00032-3.

[93] K. Tsubouchi, K. Masu, Area-selective CVD of metals, Thin Solid Films. 228 (1993) 312–318. https://doi.org/10.1016/0040-6090(93)90624-X.

[94] S.P. Douglas, C.E. Knapp, Low-Temperature Deposition of Highly Conductive Aluminum Metal Films on Flexible Substrates Using Liquid Alane MOD Precursors, ACS Appl. Mater Interfaces. 12 (2020) 26193–26199. https://doi.org/10.1021/acsami.0c05429.

[95] H.M. Lee, J.Y. Seo, A. Jung, S.Y. Choi, S.H. Ko, J. Jo, S. Bin Park, D. Park, Long-term sustainable aluminum precursor solution for highly conductive thin films on rigid and flexible substrates, ACS Appl. Mater Interfaces. 6 (2014) 15480–15487. https://doi.org/10.1021/am504134f.

[96] W.L. Gladfelter, D.C. Boyd, K.F. Jensen, Trimethylamine Complexes of Alane as Precursors for the Low-Pressure Chemical Vapor Deposition of Aluminum, Chemistry of Materials. 1 (1989) 339–343. https://doi.org/10.1021/cm00003a013.

[97] V. Shashkin, S. Rushworth, V. Danil'tsev, A. Murel, Y. Drozdov, S. Gusev, O. Khrykin, N. Vostokov, Microstructure and properties of aluminum contacts formed on GaAs(100) by low pressure chemical vapor deposition with dimethylethylamine alane source, J. Electron Mater. 30 (2001) 980–986. https://doi.org/10.1007/BF02657721.

[98] B.M. Wong, D. Lacina, I.M.B. Nielsen, J. Graetz, M.D. Allendorf, Thermochemistry of alane complexes for hydrogen storage: A theoretical and experimental investigation, Journal of Physical Chemistry C. 115 (2011) 7778–7786. https://doi.org/10.1021/JP112258S/SUPPL_FILE/JP112258S_SI_001.PDF.

[99] M.J. Krause, F. Orlandi, A.T. Saurage, J.R. Zietz, Aluminum Compounds, Organic, Ullmann's Encyclopedia of Industrial Chemistry. (2000). https://doi.org/10.1002/14356007.A01_543.

[100] Y. Matsumiya, K. Nakajima, Temperature dependence of decomposition pathway of dimethylaluminum hydride, J. Cryst. Growth. 181 (1997) 437–440. https://doi.org/10.1016/S0022-0248(97)00390-4.

[101] P.T. Michaud, D. Babic, A Raman Study of Etching Silicon in Aqueous Tetramethylammonium Hydroxide, J Electrochem Soc. 145 (1998) 4040–4043. https://doi.org/10.1149/1.1838911.

[102] M.G. Simmonds, I. Taupin, W.L. Gladfelter, Selective Area Chemical Vapor Deposition of Aluminum Using Dimethylethylamine Alane, Chemistry of Materials. 6 (1994) 935–942. https://doi.org/10.1021/cm00043a012.

[103] B.D. Clark, C.J. Desantis, G. Wu, D. Renard, M.J. McClain, L. Bursi, A.L. Tsai, P. Nordlander, N.J. Halas, Ligand-Dependent Colloidal Stability Controls the Growth of Aluminum Nanocrystals, J. Am. Chem Soc. 141 (2019) 1716–1724. https://doi.org/10.1021/jacs.8b12255.

[104] S. Okasha, Y. Sekine, S. Sasaki, Y. Harada, Atomic layer deposition of aluminum (111) thin film by dimethylethylaminealane precursor, Thin Solid Films. (2021) 138784. https://doi.org/10.1016/j.tsf.2021.138784.

[105] R.C. Blish, S. Li, H. Kinoshita, S. Morgan, A.F. Myers, Gold - Aluminum intermetallic formation kinetics, in: IEEE Transactions on Device and Materials Reliability, 2007: pp. 51–63. https://doi.org/10.1109/TDMR.2007.891533.

[106] A. Kamijo, T. Mitsuzuka, A highly oriented Al[111] texture developed on ultrathin metal underlayers, J. Appl. Phys. 77 (1995) 3799–3804. https://doi.org/10.1063/1.358555.

[107] H. Shibata, M. Murota, K. Hashimoto, The effects of al(Lll) crystal orientation on electromigration in half-micron layered a1 interconnects, Jpn J. Appl. Phys. 32 (1993) 4479–4484. https://doi.org/10.1143/JJAP.32.4479.

[108] R.C. Blish, S. Li, H. Kinoshita, S. Morgan, A.F. Myers, Gold - Aluminum intermetallic formation kinetics, IEEE Transactions on Device and Materials Reliability. 7 (2007) 51–63. https://doi.org/10.1109/TDMR.2007.891533.

[109] B. Xu, J. Liu, X. Wang, Preparation and thermal properties of aluminum hydride polymorphs, Vacuum. 99 (2014) 127–134. https://doi.org/10.1016/J.VACUUM.2013.05.009.

[110] M.B. Katz, M.E. Twigg, S.M. Prokes, Formation and stability of crystalline and amorphous Al2O3 layers deposited on Ga2O3 nanowires by atomic layer epitaxy, J. Appl. Phys. 120 (2016) 124311. https://doi.org/10.1063/1.4963282.

[111] A. Pugliese, B. Shyam, G.M. Repa, A.H. Nguyen, A. Mehta, E.B. Webb, L.A. Fredin, N.C. Strandwitz, Atomic-Layer-Deposited Aluminum Oxide Thin Films Probed with X-ray Scattering and Compared to Molecular Dynamics and Density Functional Theory Models, ACS Omega. 7 (2022) 41033–41043. https://doi.org/10.1021/ACSOMEGA.2C04402/ASSET/IMAGES/LARGE/AO2C04402_0008.JPEG.

[112] K.M. Niang, G. Bai, J. Robertson, Influence of precursor dose and residence time on the growth rate and uniformity of vanadium dioxide thin films by atomic layer deposition, Journal of Vacuum Science & Technology A. 38 (2020) 042401. https://doi.org/10.1116/6.0000152.

[113] B.T. Matthias, T.H. Geballe, V.B. Compton, Superconductivity, Rev Mod Phys. 35 (1963) 1–22. https://doi.org/10.1103/RevModPhys.35.1.

[114] J.J. Hauser, Enhancement of superconductivity in aluminum films, Phys Rev B. 3 (1971) 1611–1616. https://doi.org/10.1103/PhysRevB.3.1611.

[115] R.B. Pettit, J. Silcox, Film structure and enhanced superconductivity in evaporated aluminum films, Phys Rev B. 13 (1976) 2865–2872. https://doi.org/10.1103/PhysRevB.13.2865.

[116] K. Houben, J.K. Jochum, S. Couet, E. Menéndez, T. Picot, M.Y. Hu, J.Y. Zhao, E.E. Alp, A. Vantomme, K. Temst, M.J. Van Bael, The influence of phonon softening on the superconducting critical temperature of Sn nanostructures, Sci Rep. 10 (2020) 1–9. https://doi.org/10.1038/s41598-020-62617-4.

[117] R.J. Needs, Calculations of the surface stress tensor at aluminum (111) and (110) surfaces, Phys. Rev. Lett. 58 (1987) 53–56. https://doi.org/10.1103/PhysRevLett.58.53.

[118] R.W. Cohen, B. Abeles, Superconductivity in granular aluminum films, Physical Review. 168 (1968) 444–450. https://doi.org/10.1103/PhysRev.168.444.

[119] G.J. Dolan, Offset masks for lift-off photoprocessing, Appl. Phys. Lett. 31 (1977) 337–339. https://doi.org/10.1063/1.89690.

[120] D. Born, T. Wagner, W. Krech, U. Hübner, L. Fritzsch, Fabrication of ultrasmall tunnel junctions by electron beam direct-writing, in: IEEE Transactions on Applied Superconductivity, 2001: pp. 373–376. https://doi.org/10.1109/77.919360.

[121] J.H. Lee, K. Kamada, N. Enomoto, J. Hojo, Morphology-selective synthesis of polyhedral gold nanoparticles: What factors control the size and morphology of gold nanoparticles in a wet-chemical process, J Colloid Interface Sci. 316 (2007) 887–892. https://doi.org/10.1016/J.JCIS.2007.08.053.

[122] J. Henzie, S.C. Andrews, X.Y. Ling, Z. Li, P. Yang, Oriented assembly of polyhedral plasmonic nanoparticle clusters, Proc Natl Acad Sci U S A. 110 (2013) 6640–6645. https://doi.org/10.1073/PNAS.1218616110/SUPPL_FILE/SM04.MP4.

[123] S. Polani, S. Melamed, L. Burlaka, F. De La Vega, D. Zitoun, Large-scale synthesis of polyhedral Ag nanoparticles for printed electronics, RSC Adv. 7 (2017) 54326–54331. https://doi.org/10.1039/C7RA11370F.

[124] J.L. Montaño-Priede, U. Pal, Estimating Near Electric Field of Polyhedral Gold Nanoparticles for Plasmon-Enhanced Spectroscopies, Journal of Physical Chemistry C. 123 (2019) 11833–11839. https://doi.org/10.1021/ACS.JPCC.9B01105/SUPPL_FILE/JP9B01105_SI_001.PDF.

[125] P. Tang, M. Xing, L. Zhong, X. Xing, H. Wang, S. Liu, X. Lu, Y. Qin, Polyhedral-Au@SiO2@Au Core–Shell Nanoparticle Reveals a Broadband and Tunable Strong Local Field Enhancement, The Journal of Physical Chemistry C. 126 (2022) 8165–8176. https://doi.org/10.1021/ACS.JPCC.2C01586.

[126] D. Agarwal, C.O. Aspetti, M. Cargnello, M.L. Ren, J. Yoo, C.B. Murray, R. Agarwal, Engineering Localized Surface Plasmon Interactions in Gold by Silicon Nanowire for Enhanced Heating and Photocatalysis, Nano Lett. 17 (2017) 1839–1845. https://doi.org/10.1021/ACS.NANOLETT.6B05147/ASSET/IMAGES/LARGE/NL-2016-051475_0004.JPEG.

[127] C.R. Jacobson, G. Wu, L.B. Alemany, G.N. Naidu, M. Lou, Y. Yuan, A. Bayles, B.D. Clark, Y. Cheng, A. Ali, A.-L. Tsai, I.A. Tonks, P. Nordlander, N.J. Halas, A Dual Catalyst Strategy for Controlling Aluminum Nanocrystal Growth, Nano Lett. (2022). https://doi.org/10.1021/ACS.NANOLETT.2C01854.

[128] A. Shahravan, T. Desai, T. Matsoukas, Passivation of aluminum nanoparticles by plasma-enhanced chemical vapor deposition for energetic nanomaterials, ACS Appl. Mater. Interfaces. 6 (2014) 7942–7947. https://doi.org/10.1021/AM5012707/SUPPL_FILE/AM5012707_SI_001.PDF.

[129] J. Olson, A. Manjavacas, T. Basu, D. Huang, A.E. Schlather, B. Zheng, N.J. Halas, P. Nordlander, S. Link, High chromaticity aluminum plasmonic pixels for active liquid crystal

displays, ACS Nano. 10 (2016) 1108–1117. https://doi.org/10.1021/ACSNANO.5B06415/SUPPL_FILE/NN5B06415_SI_004.AVI.

[130] S.W. Lin, J.Y. Wu, S. Di Lin, M.C. Lo, M.H. Lin, C. Te Liang, Characterization of single-crystalline aluminum thin film on (100) GaAs substrate, Jpn J. Appl. Phys. 52 (2013) 045801. https://doi.org/10.7567/JJAP.52.045801.

[131] K.K. Miller, J.L. Gottfried, S.D. Walck, M.L. Pantoya, C.C. Wu, Plasma surface treatment of aluminum nanoparticles for energetic material applications, Combust Flame. 206 (2019) 211–213. https://doi.org/10.1016/j.combustflame.2019.04.042.

[132] M.J. Meziani, C.E. Bunker, F. Lu, H. Li, W. Wang, E.A. Guliants, R.A. Quinn, Y.P. Sun, Formation and properties of stabilized aluminum nanoparticles, ACS Appl. Mater Interfaces. 1 (2009) 703–709. https://doi.org/10.1021/am800209m.

[133] J. Katyal, R.K. Soni, Size- and shape-dependent plasmonic properties of aluminum nanoparticles for nanosensing applications, J. Mod. Opt. 60 (2013) 1717–1728. https://doi.org/10.1080/09500340.2013.856483.

[134] R. Schefflan, S. Kovenklioglu, D. Kalyon, M. Mezger, M. Leng, Formation of aluminum nanoparticles upon condensation from vapor phase for energetic applications, Journal of Energetic Materials. 24 (2006) 141–156. https://doi.org/10.1080/07370650600672041.

[135] S. Okasha, Y. Harada, Atomic layer deposition of self-assembled aluminum nanoparticles using dimethylethylamine alane as precursor and trimethylaluminum as an initiator, Journal of Nanoparticle Research. 24 (2022) 1–7. https://doi.org/10.1007/S11051-022-05618-W/METRICS.

[136] A.Z. Hezave, F. Esmaeilzadeh, Investigation of the rapid expansion of supercritical solution parameters effects on size and morphology of cephalexin particles, J. Aerosol Sci. 41 (2010) 1090–1102. https://doi.org/10.1016/j.jaerosci.2010.08.004.

[137] H. Kim, J. Han, T.Y.J. Han, Machine vision-driven automatic recognition of particle size and morphology in SEM images, Nanoscale. 12 (2020) 19461–19469. https://doi.org/10.1039/d0nr04140h.

[138] G.A. Roth, N.M. Neu-Baker, S.A. Brenner, SEM analysis of particle size during conventional treatment of CMP process wastewater, Science of the Total Environment. 508 (2015) 1–6. https://doi.org/10.1016/j.scitotenv.2014.11.075.

[139] X. Xu, Z. Liu, B. Zhang, H. Chen, J. Zhang, T. Wang, K. Zhang, J. Zhang, P. Huang, Effect of Mn content on microstructure and properties of 6000 series aluminum alloy, Appl. Phys. A Mater Sci Process. 125 (2019) 490. https://doi.org/10.1007/s00339-019-2780-9.

[140] B. Xu, J. Liu, X. Wang, Preparation and thermal properties of aluminum hydride polymorphs, Vacuum. 99 (2014) 127–134. https://doi.org/10.1016/j.vacuum.2013.05.009.

[141] O.A. Filippov, V.N. Tsupreva, L.M. Golubinskaya, A.I. Krylova, V.I. Bregadze, A. Lledos, L.M. Epstein, E.S. Shubina, Proton-transfer and H2-elimination reactions of trimethylamine

alane: Role of dihydrogen bonding and lewis acid-base interactions, Inorg Chem. 48 (2009) 3667–3678. https://doi.org/10.1021/IC802262H/SUPPL_FILE/IC802262H_SI_001.PDF.

[142] A. Corma, H. García, Lewis Acids: From Conventional Homogeneous to Green Homogeneous and Heterogeneous Catalysis, Chem. Rev. 103 (2003) 4307–4365. https://doi.org/10.1021/CR030680Z.

[143] G.N. Parsons, S.M. George, M. Knez, Progress and future directions for atomic layer deposition and ALD-based chemistry, MRS Bulletin 2011 36:11. 36 (2011) 865–871. https://doi.org/10.1557/MRS.2011.238.

[144] A. Arab, M. Habibzadeh, Theoretical study of geometry, stability and properties of Al and AlSi nanoclusters, J. Nanostructure Chem. 6 (2016) 111–119. https://doi.org/10.1007/s40097-015-0185-7.

[145] G. Guisbiers, G. Abudukelimu, Influence of nanomorphology on the melting and catalytic properties of convex polyhedral nanoparticles, Journal of Nanoparticle Research. 15 (2013) 1–12. https://doi.org/10.1007/s11051-013-1431-x.

[146] R. Ahlrichs, S.D. Elliott, Clusters of aluminium, a density functional study, Physical Chemistry Chemical Physics. 1 (1999) 13–21. https://doi.org/10.1039/a807713d.

Appendix (A) ALD process descriptions

1. ALD equipment descriptions

Aluminum thin films are grown in the thermal ALD chamber (SUNALE R-150 by Picosun oy.) equipped with a glovebox where nitrogen gas is filled up in order to prevent samples from oxygen exposure.

Atomic layer deposition model SUNALE R150 is equipped with a glove box to prevent contaminations, hence there are two control panels for each of them.

- **Global box control panel**

  - GB button should be green to maintain the pressure inside (The Global box value is ΔP from atmosphere) as shown in figure 51.
  - N_2 gas is used for pressure control for PB&GB due to its cost comparing to others gases such like O_2 or Ar.
  - Plastic gloves should be worn to protect rubber hands of global box.
  - There is a N_2 gun inside the GB for cleaning purpose.

Figure 51: passing box control panel.

- **Inserting the sample through passing box (PB)**

    - Touch 1st PB button from right to introduce N_2 for pressure equalization with atmosphere which PB with respect to external pressure (ΔP at 1^{st} button from right) =0. Make sure you unlocked the box external door before N_2 introduction to prevent box compression.
    - Put the samples inside the passing box, close the door and locks.
    - Touch 2^{nd} PB button for pumping vacuum (Air evacuation), until the button turn from green to gray.
    - Touch 3^{rd} PB to introduce N_2 gas and pumping vacuum to equalize the pressure inside PB& GB.
    - Open the PB internal gate where inside the GB by raising the internal arm to up and move the gate straight towards the GB.
    - Get the samples and then close the gate to its first position and down the arm.

- **Getting out the samples from GB**

    - Open the PB internal gate where inside the GB by raising the gate arm to up and move the gate straight towards the GB.
    - Put the samples inside passing box and then close the gate to its first position and down the arm.
    - Touch 1st PB button from right to introduce N_2 for pressure equalization with atmosphere which would be PB with respect external pressure (ΔP at 1^{st}

button from right) =0. Make sure you unlocked the box external door before N_2 introduction to prevent box compression.

- Get your samples out and then close &lock the door again.
- Touch 2nd PB button for pumping vacuum (Air evacuation) until the button turn from green to gray.
- Touch 3rd PB to introduce N_2 gas and pumping vacuum to equalize the pressure inside PB& GB.

2. ALD process descriptions:

To Log in into panel; touch log in then "o" small letter following by return button to find the PI chart as shown in figure 52, this ALD system is done by Picosun company. You can go through different sections of the system by touch the target section. Each section is described as following:

- **PI chart:**

- There are three stop manual valves for all sources precursors of A, B& C: TMA, DMZ& water respectively. A&B valves should be closed tightly while C valve is enough to be closed. You should hold container during closing/opening valves to not break any pipe.

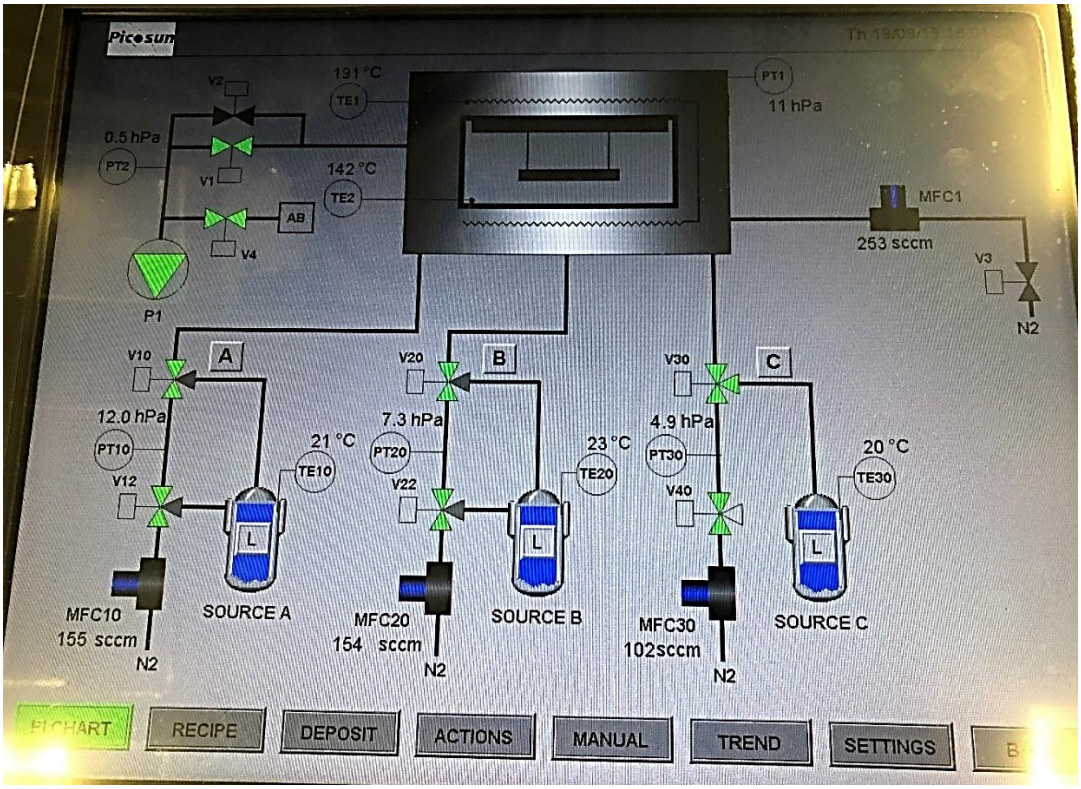

Figure 52: PI chart.

- There are heat jacket to maintain the temperature to 20 °C, with working idea of Peltier effect.
- N_2 gas continually flows inside the process, the valves with flow value are manipulated to control the pressure and pipe purging. During the process; it considers purging in case of no pluses of resources procurers.
- To inject precursors, the valve of targeted one open as pluses. Each resource precursors could be used to more than 10000 pluses.

- **Cleaning entire ALD reactor steps**

It is recommended to clean entire reactor by performing Al_2O_3 layer deposition process before inserting substrates. Cleaning process consist deposit Al_2O_3 layers as covers the pervious metal oxide or any potential contaminations may could interfere in upcoming process.

Cleaning process consists of a deposition of Al_2O_3 using source A: TMA and source C: water with deposition temperature = 250 ^{o}C in following steps:

- From initial screen, touch log in then "o" then return.
- Assure that All stop valves are closed manually and then perform following two steps:
    1. From Manual 1/3, touch quickly and sequentially open &close for Valves 10 and 30 as they are the pipes of TMA and water respectively.
    2. From Actions 3/3 and notice the graphs of PT10 &PT30. You can switch between then after 8000 milliseconds. The graphs peaks should be dissipated [] otherwise the related valve still open. So you close it more tightly and repeat the previous two steps.
- From Manual 3/3; set "TE1 max" (heater) to 250 +80 = 330 ^{o}C& "TE2" (reactor chamber) to 250^{o}C. (please note: max ΔTE1-ΔTE2= 80 ^{o}C, otherwise reactor temperature would increase uncontrollably which would require long time to cool again ~around 2 hrs/1 ^{o}C).
- Flush sources pipes and valves needles as following; from Actions 1/3, touch purge source A&C separately one by one and then touch execute per each. (The N_2 flow of flushing pipe will exponentially increase and decrease at PI chart around 10 times

sequentially from 102 to 1002 sccm. (You can track flush process from Trends of flow rates)

- Touch recipe ¼ then write following information from real cleaning example:
    3. Active folder: OKASHA
    4. Recipe name: AO190918
    5. Active RECICPE: AO190918
    6. SUBSTRATE ID: PREDEPO
    7. Substrate &end Temperature: 250 °C.
    8. Remaining values described in the ALD manual.
- Touch Recipe 2/4 write following values for source A1 (TMA) &C1 (water):
    1. Pulse time: 0.1 s.
    2. Purge time: 4 s.
    3. Remaining values described in the ALD manual.
- From recipe 4/4: choose Number of cycle: 300 times in the big loop cycle after choosing of A1&C1.
- Back to Recipe ¼ and click “save recipe”.
- You can open sources bottles (A&C) and **check their flow** in following two steps:
    1. From Manual 1/3, touch quickly and sequentially open &close for Valves of TMA and water respectively, V10 and V30, in form of pluses.
    1. From Actions 3/3 and notice the graphs of PT10 &PT30. You can switch between them after 8000 milliseconds. The graphs peaks should be constantly high [] in same number of pluses of step 1, Otherwise there are a problem such like bottle close to be empty and time to replace.

- From Deposit, choose “Start” and wait for couple of hours for entire process loop progress.
- After process completed; close sources valves manually then check them tightness in following 2 steps:
    1. From Manual 1/3, touch quickly and sequentially open &close for Valves 10 and 30 as they are the pipes of TMA and water respectively.
    2. From Actions 3/3 and notice the graphs of PT10 &PT30. You can switch between then after 8000 milliseconds. The graphs peaks should be dissipated [] otherwise the related valve still open. So you close it more tightly and repeat the previous two steps.
- From Actions 1/3 touch purge source A&C and then execute one by one separately.
- From Manual 3/3; set TE1 (heater) & TE2 (reactor chamber) to 20^{o}C and not zero.
- From Setting, touch Log out.
- Records deposition values to log note (operation log and status check)

3. Recipe sections:

- There are 5 sub recipes with different parameters per each.
- Recipe (1/4) as shown in figure 53 can change the active folder (ex. OKASHA), recipe name with 8 digits (ex. ZA190919 or Z190919A), and substrate ID (ex. ZnO or ZnO/Al_2O_3) and temperature (ex. 140 ^{o}C).

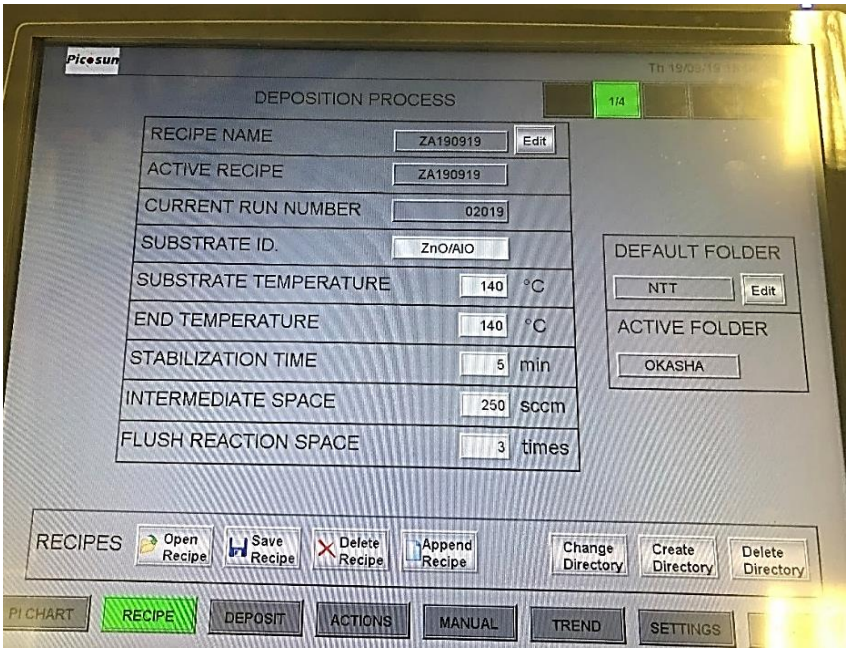

Figure 53: Recipe page 1/4.

- For ZnO deposition temperature is 100 ^{o}C while Al_2O_3 is 170 ^{o}C, so to deposit layers consist of both of them, Temperature chose to be 140 ^{o}C (something in middle).
- After choosing recipe, touch “Save Recipe” button.
- Flush reaction time is the number of cleaning the reactor.
- Intermediate space maintains the toxicity for safe purging.
- Stabilization time is the period after reaching to targeted temperature and before pulsing for temperature stabilization.
- End temperature is for post annealing purpose.

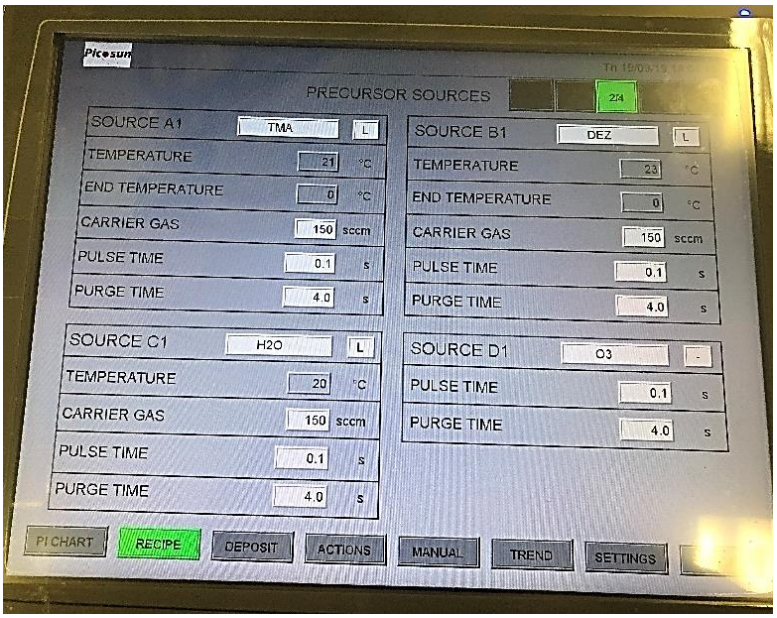

Figure 54: Recipe page 2/4.

- Recipe (2/4) as shown in figure 54 can choose pulse time and purge time for all precursors such 0.1, 4.0 second respectively.
- Carrier gas set to be 150 standard cubic centimeters (SCCM).
- Ozone is not used and not equipped to that ALD.

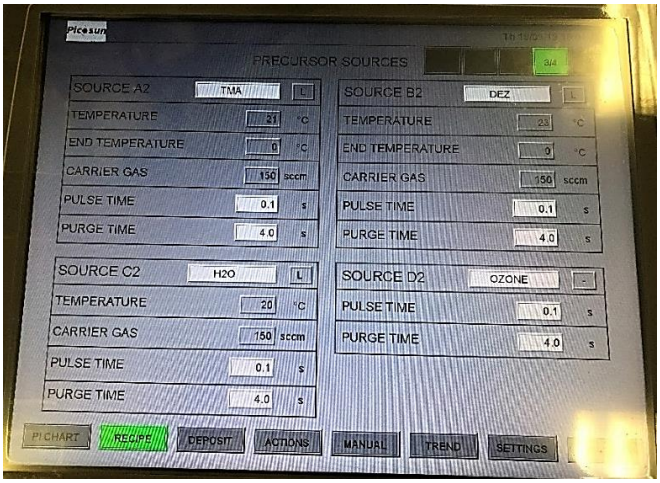

Figure 55: Recipe page 3/4.

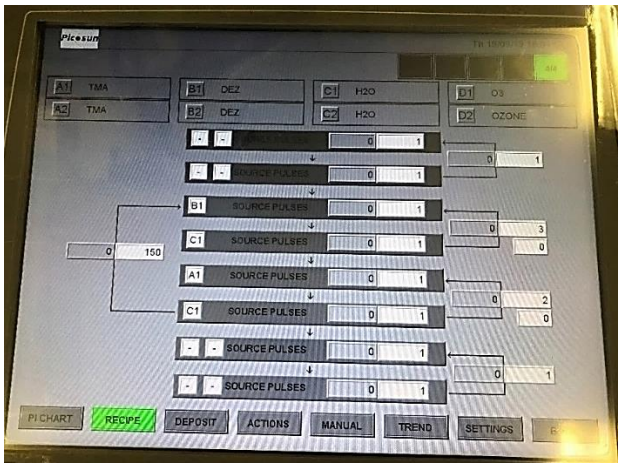

Figure 56: Recipe page 4/4.

- Recipe (3/4) as shown in figure 55 is the same exactly like pervious screen and use when a different two sets of time period required in same process.
- Recipe 4/4 as shown in figure 56 is for cycle process. It could be one to two different types of cycles. For example, 300 cycle of B1&C1 or 150 cycles of (3 layers of B1&C1+ 2 layers of A1&C1).

- **Deposit section**

- Deposit section function is to “start” deposition process or cancel it.
- When arrive to “open-source bottles”, they open manually by hand. All valves should be opened until the maximum.
- During the pulsing process, deposition can be cancelled or stopped.
- To insert substrates, touch open lid then the ALD stage would open.

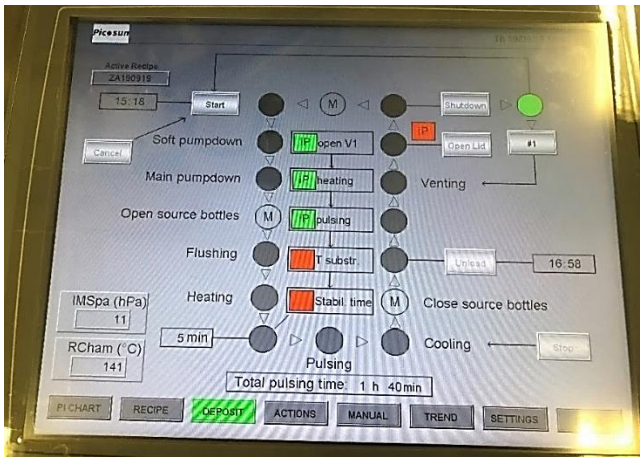

Figure 57: Deposition screen.

- There is a metal plate can be put under stage to prevent samples fall inside the instrument. If sample falls, it would be required an engineer to dissemble the instrument and assemble it gain.
- Best position of samples is the left side towards glass of GB.
- After inserting the sample, remove metal plate then touch shut down.
- There is time estimation appearing once deposition process starts. It is summation of (pulse time + purge time) multiply of number of pluses per each source process precursors.
- IP is internal pressure while IMSPA is intermediate space & RCham for reactions chamber as shown in figure 57.

- **Actions section**

- Actions section (1/3) as shown in figure 58 is mainly to purge sources pipes to clean them before the process and to prevent source accumulation after time.

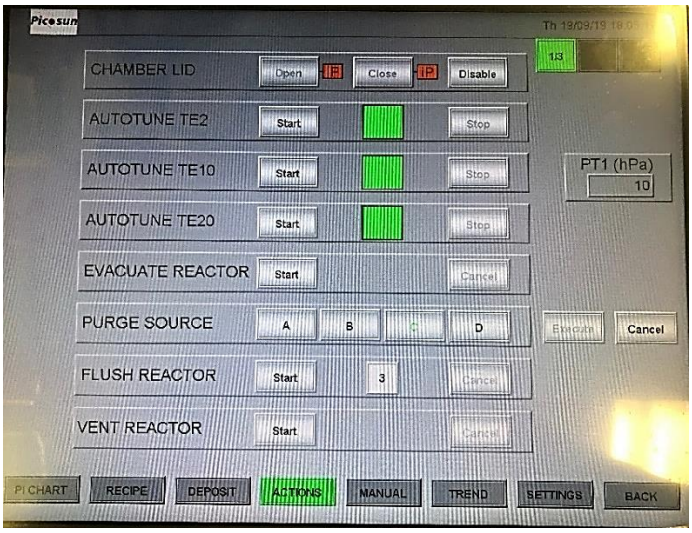

Figure 58: Actions page 1/3.

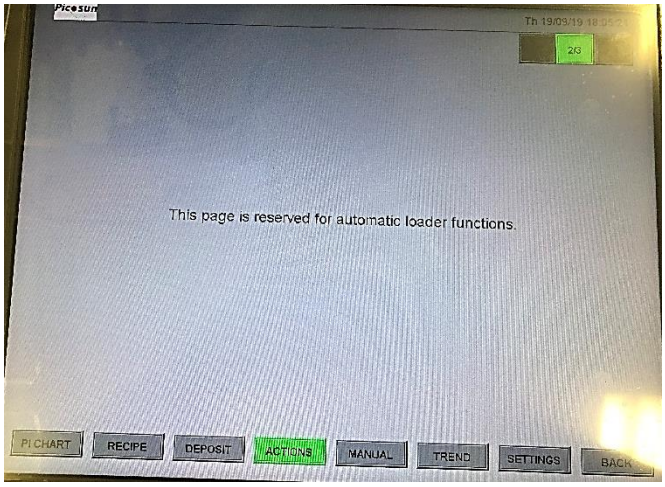

Figure 59: Actions page 2/3.

- Actions section (2/3) as shown in figure 59 is reserved for automatic loader function.
- Actions section (3/3) as shown in figure 60 consists of graphs (x: 8000 milliseconds, y: flow rate) where you can check the flow after closing the sources valves after process. You can switch between lines (PT 10, 20, 30) after 8000 milliseconds.

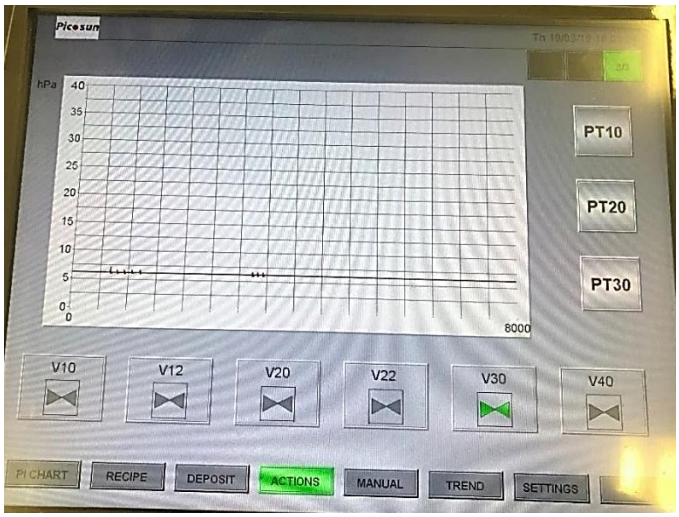

Figure 60: Actions page 3/3.

- You can instantly open valves from Manual (1/3) by quickly touch "open then close" for 3-4 times and then check then on coordination before the process to check bottle situations. The graphs peaks should be constantly high [ ] in same number of pluses, Otherwise there are a problem such like bottle close to be empty and time to replace.

- **Manual sections**

(a)

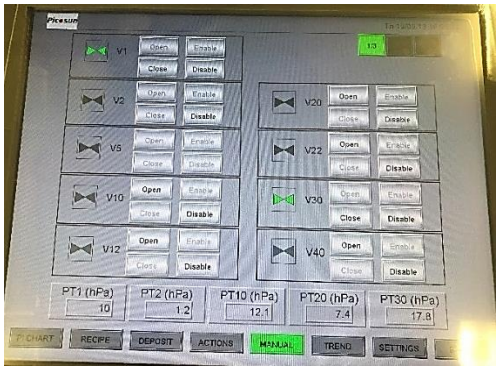

(b)

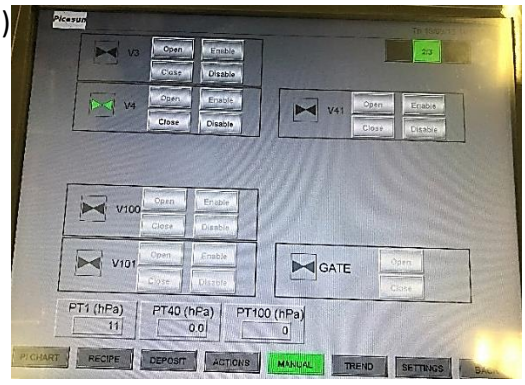

Figure 61: Manual page (a)1/3, and (b)2/3.

Figure 62*:* Manual page 3/3.

- Manual (1/3) & (2/3) as shown in figure 61 contains all process valves where you can control them manually.
- Valves 1&4 are connected to Vacuum pump, one of them are wide another is fine and they use to control the pressure through relieving the gas to keep the Pressure at PT2
- where pumping pressure should be less 1 hpa (~0.5). in case of higher than 1 hpa, system would be collapsed.
- The pressure is measured in hectopascal (hpa) = 10^2 pa.
- Manual (3/3) as shown in figure 62 contains temperatures TE1 max, TE2 values of heater and reactor chamber respectively. There is temperature difference between them around 80 ^{o}C. (ex. To deposit at temperature (TE2) = 140 ^{o}C, it is required to make heater temperature (TE1) = 140+80 =220 ^{o}C.
- Please note that maximum difference ΔTE1-ΔTE2= 80 ^{o}C, otherwise reactor temperature TE2 would increase uncontrollably which would require long time to cool again for around 2 hrs/1 ^{o}C.

- ALD process is very sensitive to temperature even one degree so the heating process raise very slowly to some couple of hours to get exact value of temperature. If the value exceeded, cooling process is much slower (approx. 1 degree down takes 2 hours)
- After deposition process, temperatures values (TE1, TE2) reset to 20 ^{o}C and not zero.
- Flow values aren't required to be changed.

- **Trend section**

(a) (b)

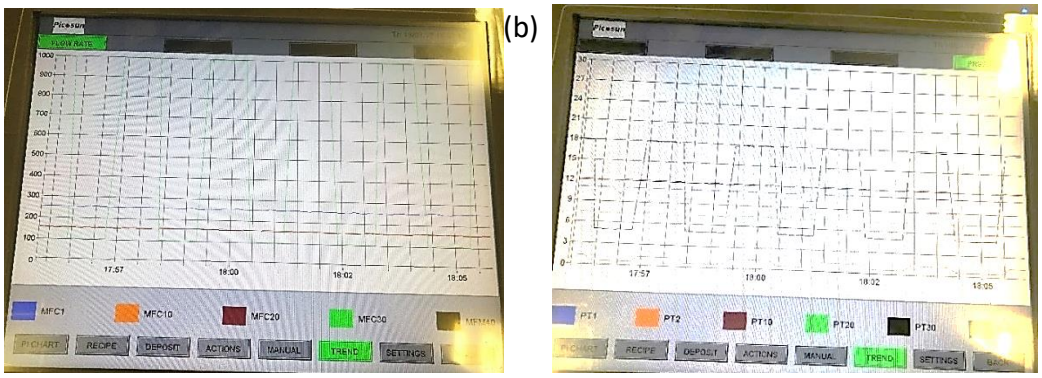

Figure 63: trend page (a) flow rate, and (b) pressure.

(a) (b)

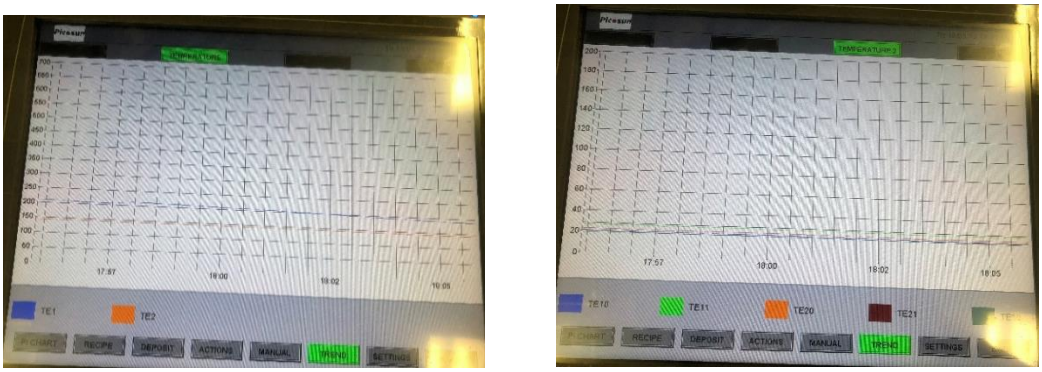

Figure 64: trend screen (a) temperature-1, and (b) temperature-2.

- Trend section contains 4 types of graphs; Flow rates, pressure as shown in figure 63 and Temperature 1&2 as shown in figure 64.
- You can track the trend process conditions and check the fluctuation by increasing the axis range by touching on x: axis then touching +/-.
- From that section, you can track pipe flush steps as you can found 10 peaks representing flush steps per each line.

- **Setting section**

- Setting section as shown in figure 65 is prohibit to be changed.
- You can log out after finishing all deposition process.

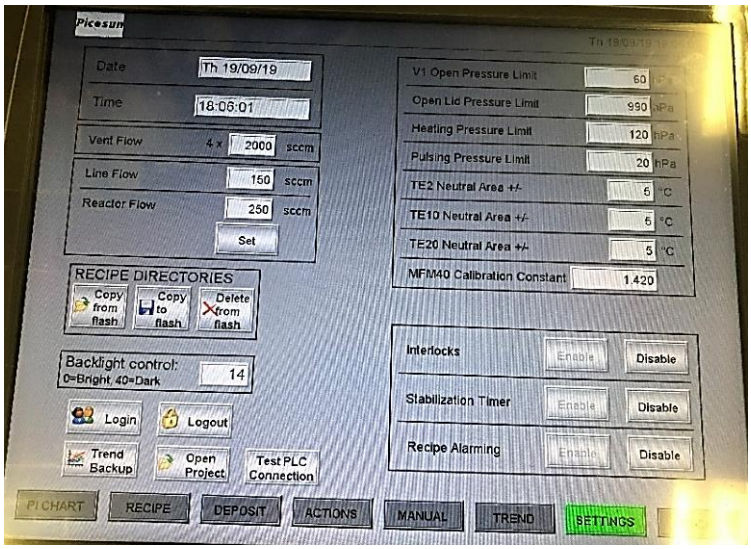

Figure 65: Setting section page.

- **Log note**

  - After the process there a log notes as shown in figure 66.

You can register following data:

Date, User, TEL, recipe,

Material, Temp, cycles and

Sum of TMA or DMZ (accumulate by addition number of process cycle to pervious process). It is important to estimate time change of source materials.

- Tick in water leakage, vacuum condition and GB temp.

- Detoxifier color is a filter color connected to reactor.

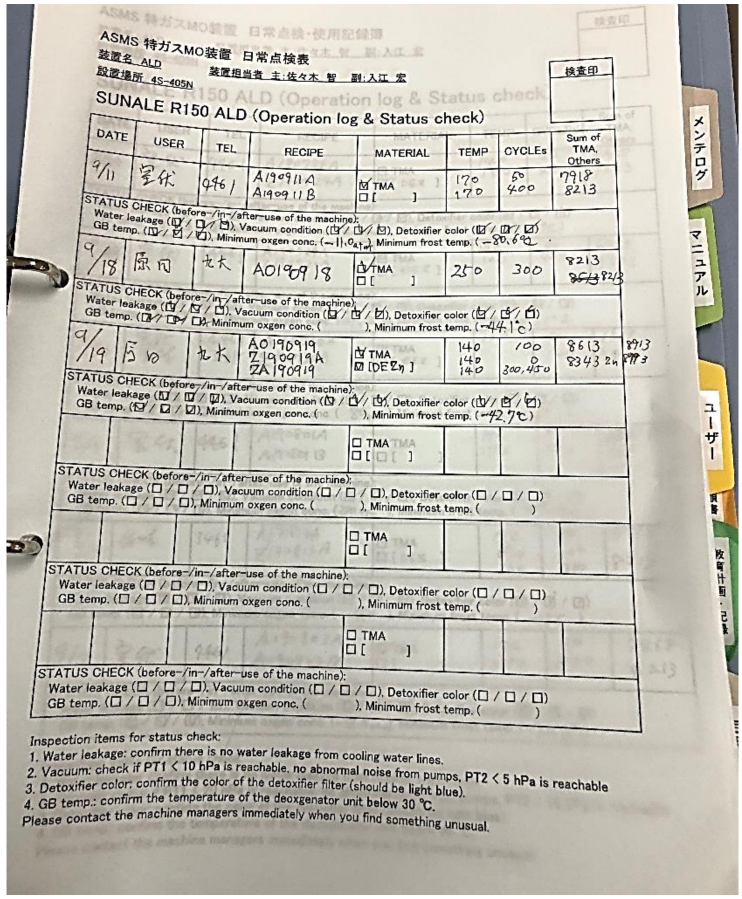

Figure 66: ALD log note.

Appendix (B) Supplementary data

2. Sample (Si/Ti 15º/Al) surface morphology at mirror spot

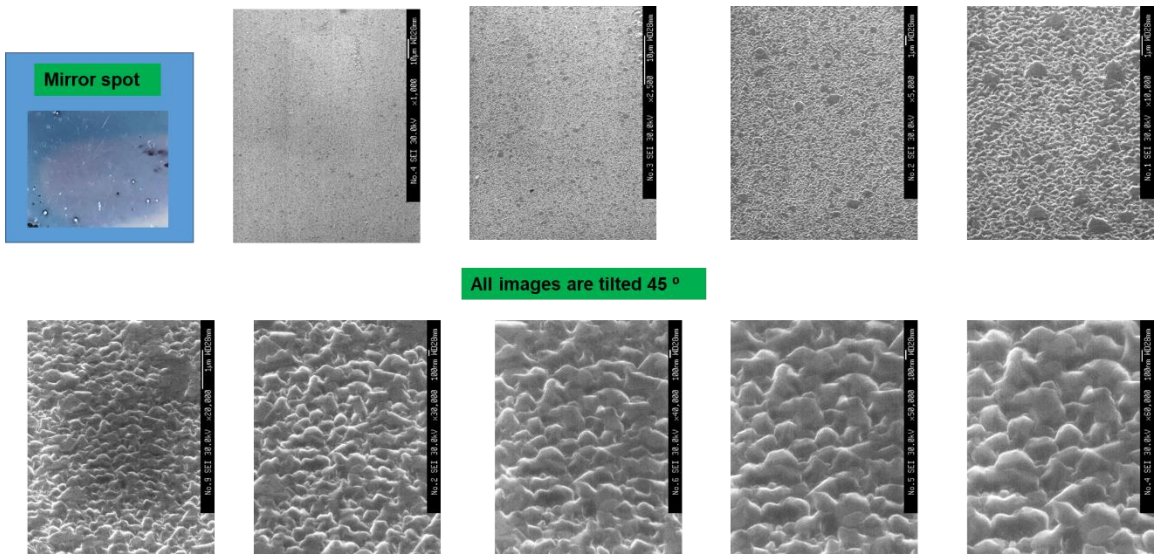

Figure 67: Surface morphology at mirror spot film.

3. Sample (Si/Ti 15º/Al) surface morphology at white spot

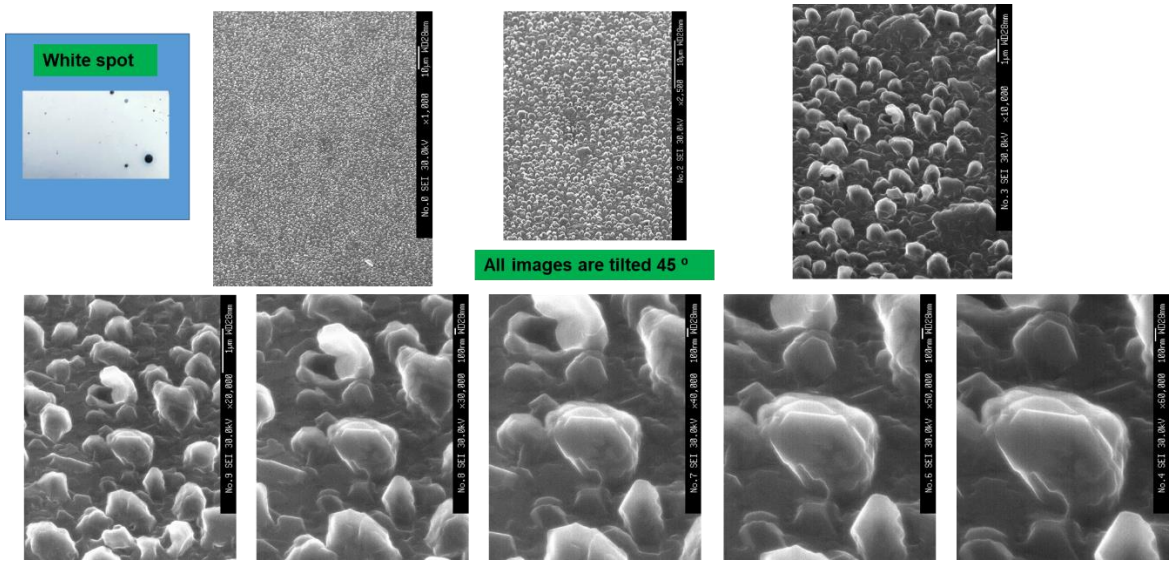

Figure 68: Surface morphology at white spot film.

4. Sample (Si/Ti 15º/Al) surface morphology at white spot (top view)

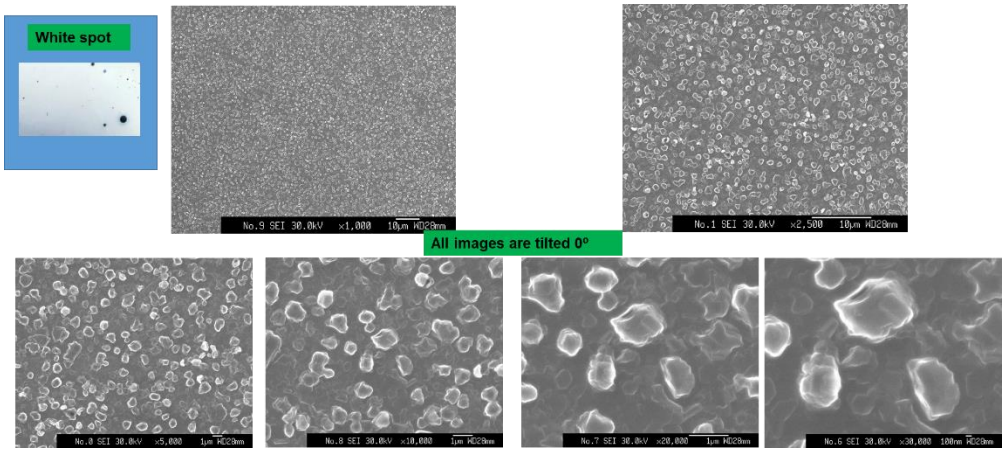

Figure 69: SEM top view at white spot film.

5. Sample (Si/Ti 15º/Al) surface morphology at mirror spot (top view)

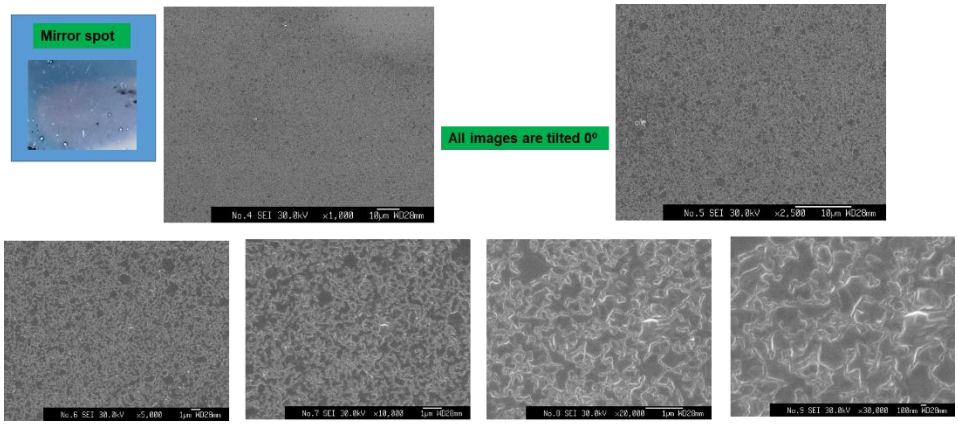

Figure 70: SEM top view at mirror spot film.

6. Sample (Si/Ti 15º/Al) surface morphology at points spot (top view)

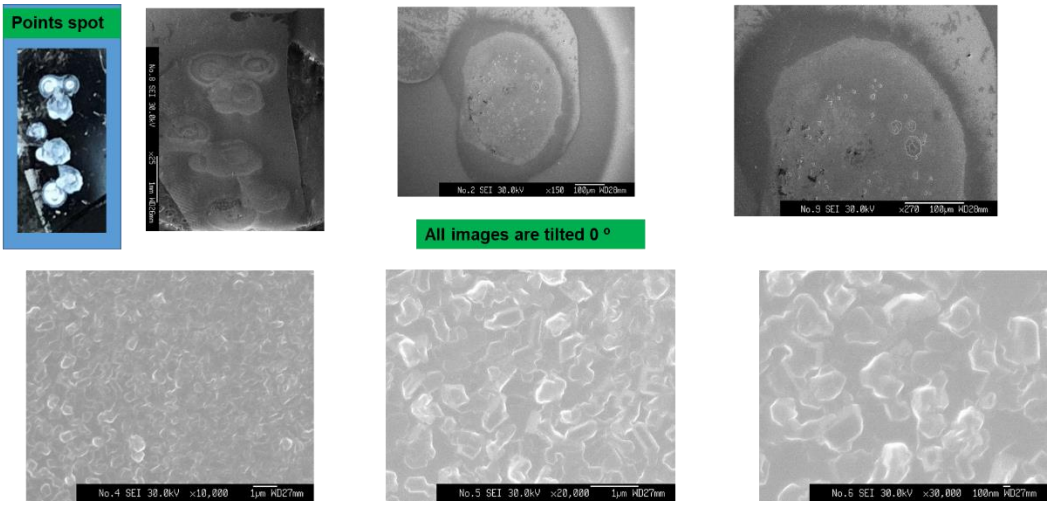

Figure 71: SEM top view at points spot film.

7. SEM comparison of mirror, white, and points

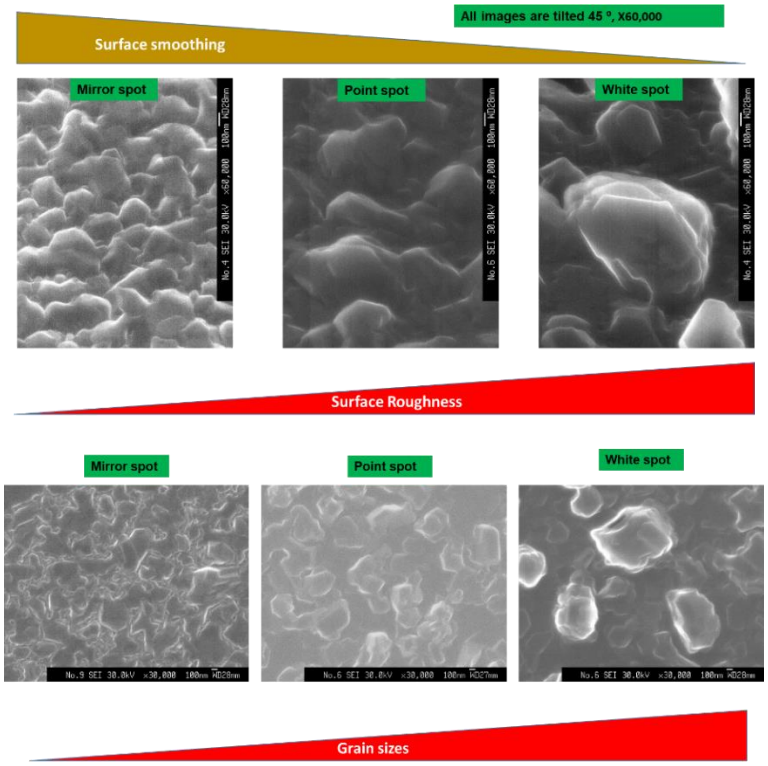

Figure 72: SEM thin films comparison of mirror-like, white rough surface, and points-like thin film.

8. Mirror surface thickness at edge

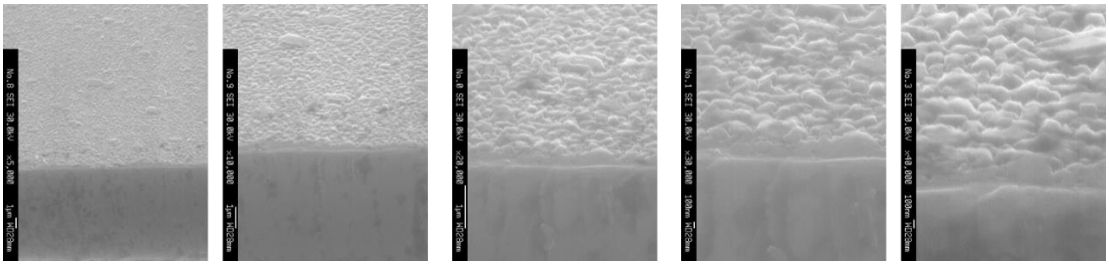

Figure 73: Mirror surface thickness at edge.

9. white surface thickness at edge

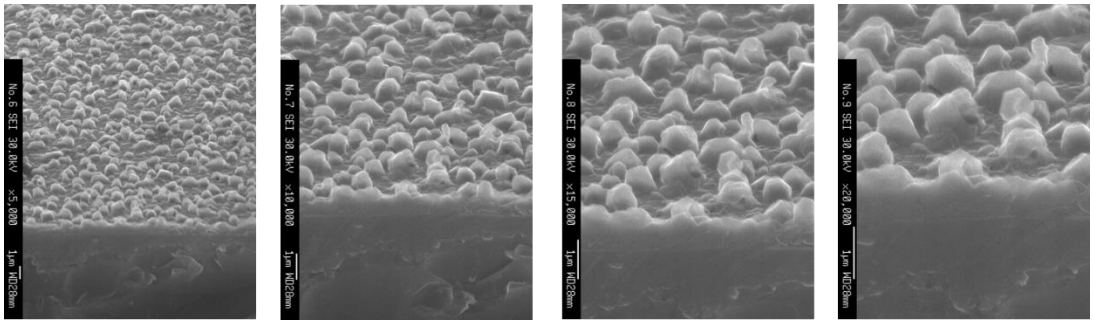

Figure 74: White surface thickness at edge.

10.XRD Comparison of samples A, B, C, and D

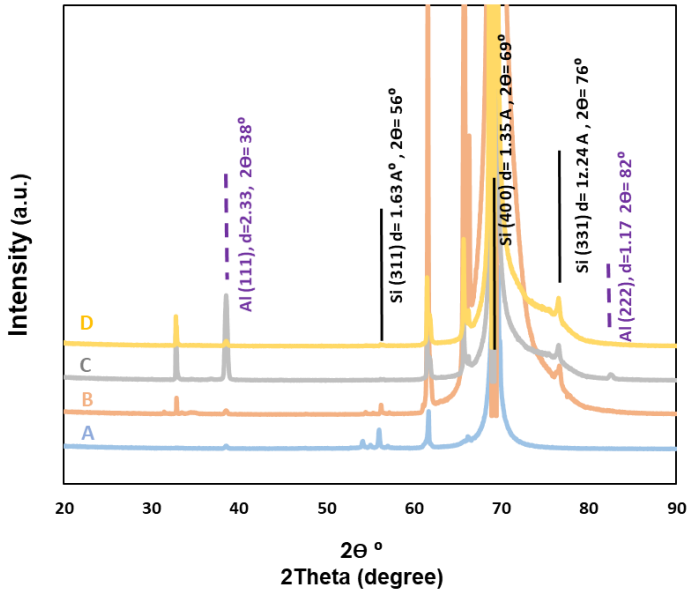

Figure 75: XRD comparison of samples A, B, C, and D.

11. XRD Comparison of (mirror, white, points) thin film

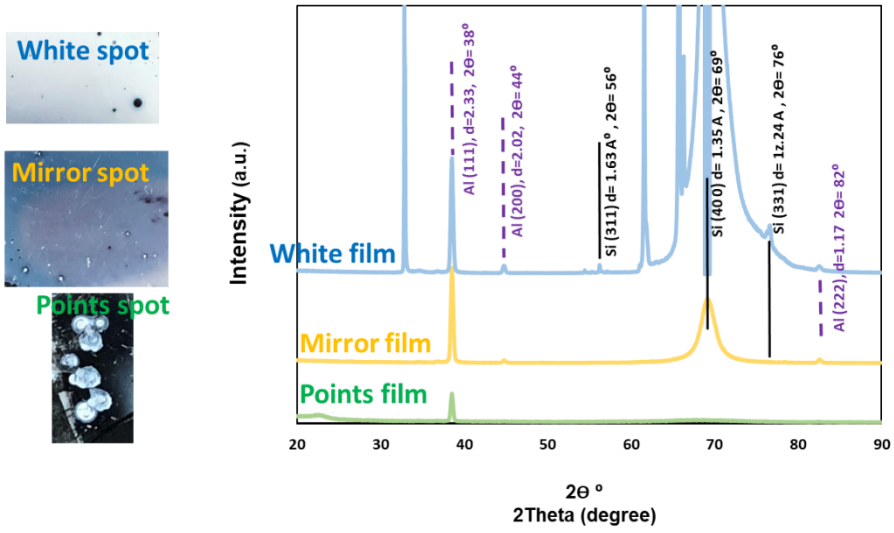

Figure 76: XRD comparison of mirror, white, and points thin film.

12. Nanoparticle's morphology

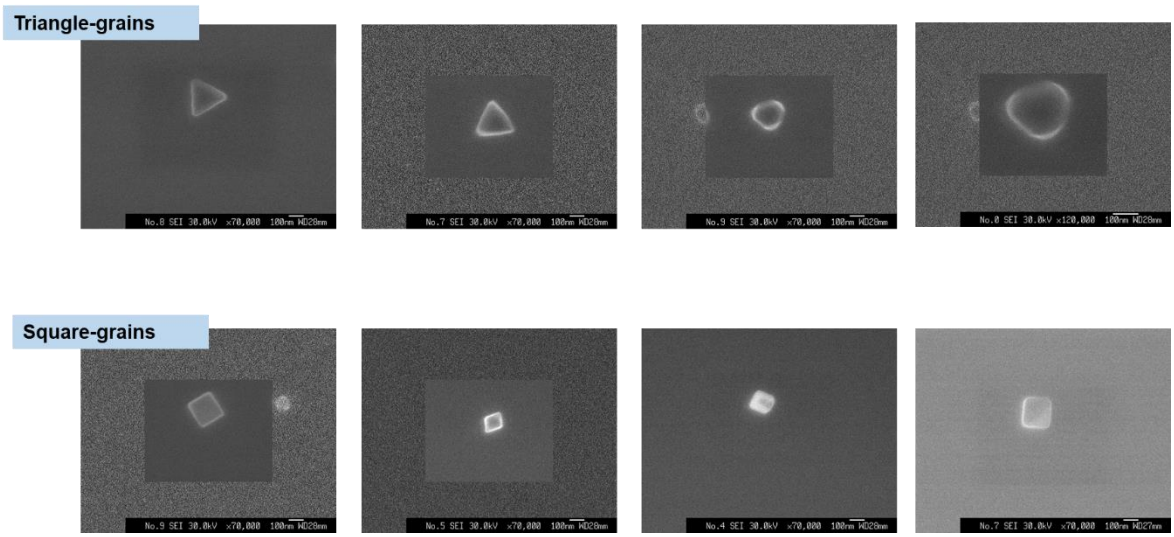

Figure 77: Single-nanoparticle morphology.

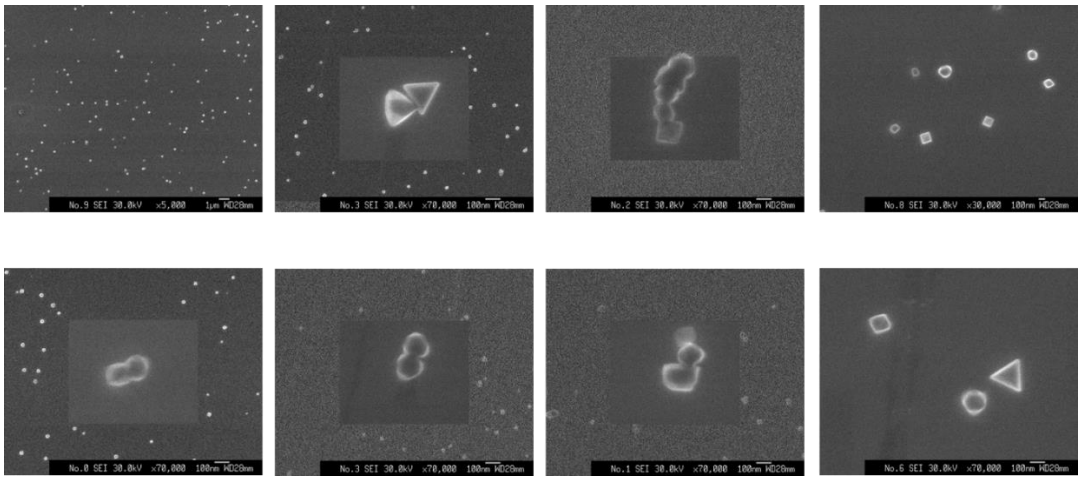

Figure 78: Nanoparticles-connection morphology.

13. SEM-EDX thin film elemental analysis

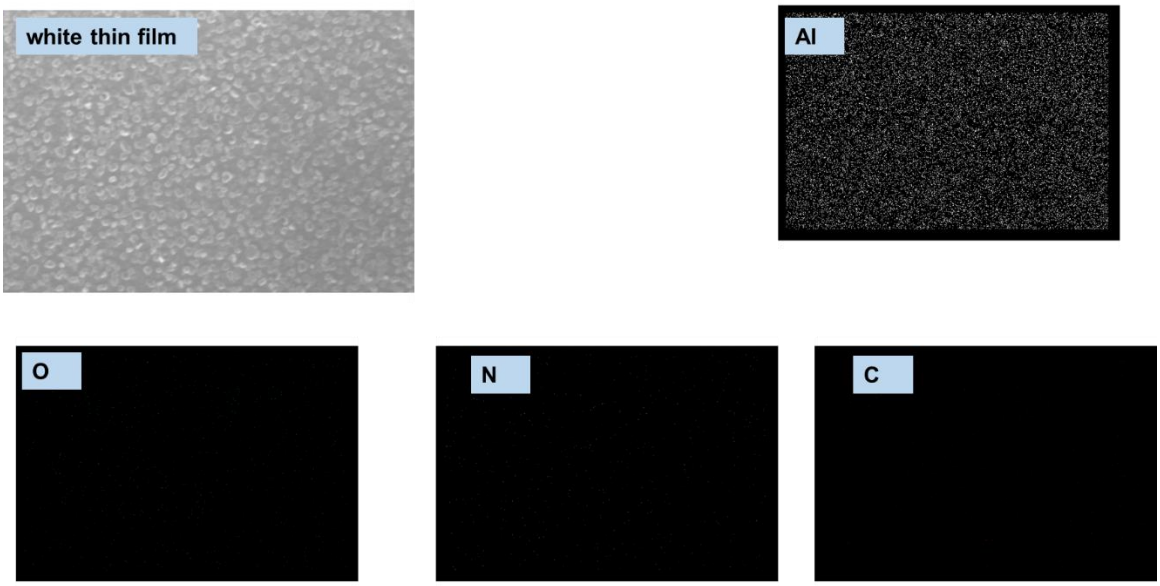

Figure 79: SEM-EDX of white thin film elemental map.

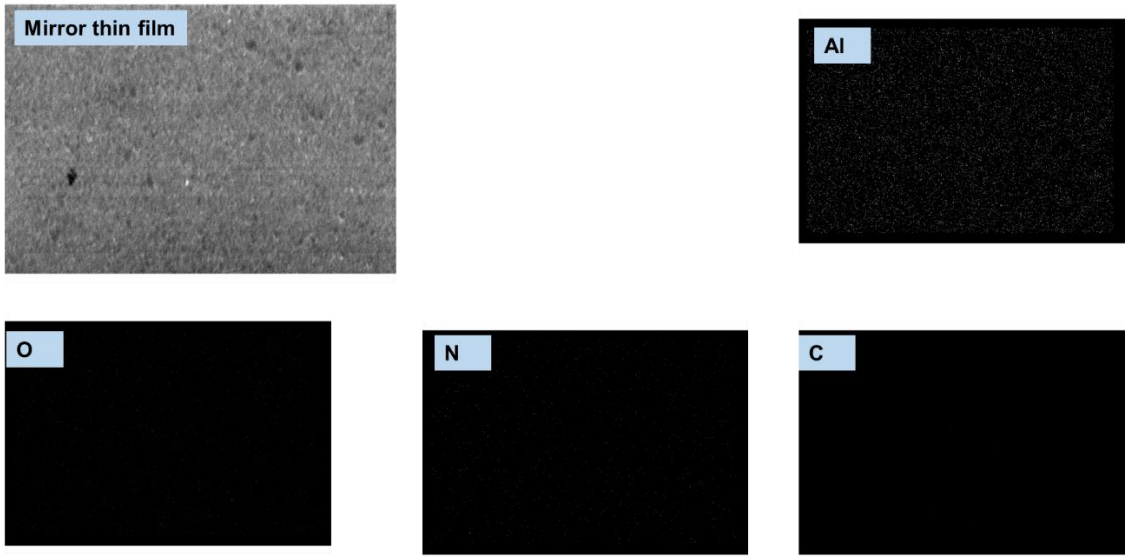

Figure 80: SEM-EDX of mirror thin film elemental map.

Publications

Thin Solid Films 732 (2021) 138784

Contents lists available at ScienceDirect

Thin Solid Films

journal homepage: www.elsevier.com/locate/tsf

Atomic layer deposition of aluminum (111) thin film by dimethylethylaminealane precursor

Sameh Okasha [a,b,*], Yoshiaki Sekine [c], Satoshi Sasaki [c], Yuichi Harada [a]

[a] Global Innovation Center, Kyushu University, 6-1 Kasuga-Koen, Kasuga, Fukuoka 816-8580, Japan
[b] Molecular and material science department, Interdisciplinary Graduate School of Engineering Sciences, Kyushu University, Kasuga, Fukuoka 816-8580, Japan
[c] NTT Basic Research Laboratories, NTT Corporation, 3-1 Morinosato Wakamiya, Atsugi, Kanagawa 243-0198, Japan

ARTICLE INFO

Keywords:
Aluminum (111) thin film
atomic layer deposition
dimethylethylaminealane
selective growth
superconducting thin film

ABSTRACT

We report the growth of aluminum (111) thin film by atomic layer deposition (ALD) technique with dimethylethylaminealane (DMEAA) as a precursor. It is found that the metallic underlayer is essential to grow uniform aluminum films by DMEAA precursor. As a titanium thin film is used as the underlayer, grown aluminum thin film shows (111) orientation irrespective of substrates. The lattice constant and superconducting transition temperature of the aluminum thin films are the same as the bulk one. These findings suggest that ALD technique provides high quality of the aluminum thin films and have potential for the applications of superconducting devices. We discuss ALD technique with DMEAA precursor is the promising method for fabricating vertical small Josephson tunnel junctions, which can be used as the superconducting quantum bits.

1. Introduction

Atomic layer deposition (ALD) technique enables us to fabricate atomically controlled thin films [1]. ALD technique can deposit insulating materials conformally which can cover the whole surface of nanowires [2] and realize quantum point contact made of a narrow $In_{0.75}Ga_{0.25}As$ channel [3]. It can be also used as the passivation layer in order to stabilize adsorbed molecules [4]. ALD technique can also deposit metallic thin films and show a sharp interface between different materials as the sequential deposition [5]. The rather low growth temperature of ALD technique offers in situ photoresist processes. These features are promising to fabricate stacked tunnel junctions including a Josephson tunnel junction that is composed of two superconducting electrodes separated by a very thin (~ 2 nm) insulating barrier.

There are several reports on precursors for the ALD growth of aluminum thin films. Trimethylaluminum (TMA) and water is a standard process to grow aluminum oxide [1], while TMA and hydrogen is used to grow aluminum thin film [6]. Dimethylaluminum hydride (DMAH) is also a good candidate as the precursor which offers reduced carbon contamination [7] and an area-selective growth [8]. Among the three precursors, we decide to use dimethylethylaminealane (DMEAA), which has several advantages: a low decomposition temperature [9], avoiding carbon contamination with long-term sustainability [10]. Although some groups reported the superiority of DMAH compared with DMEAA [7], DMAH has the disadvantages of the rough surface.

Here, we study the growth of aluminum thin films by ALD with DMEAA as a precursor. We found the metallic underlayer is necessary for obtaining aluminum. The ALD-grown aluminum films show superconductivity as same as bulk aluminum.

2. Experimental details

Aluminum thin films are grown in the thermal ALD chamber (SUNALE R-150 by Picosun oy.) equipped with a glovebox where nitrogen gas is filled up in order to prevent samples from oxygen exposure. DMEAA [11,12] precursor is used as the source of aluminum. It is worth noting that the viscosity of DMEAA is stable so that the reproducibility of deposition conditions for aluminum thin films is high while we found that the viscosity of DMAH changes in six weeks and thereby it is very difficult to grow reproducibly aluminum thin films under the same conditions. We used silicon (Si) substrates for aluminum deposition. Two of Si-substrates are prepared, one as bare substrate and the latter with a metallic layer. Both substrates are prepared with the standard degrease process and surface etching by tetramethylammonium hydroxide solution [13]. It is found that aluminum thin films can be grown on the metallic layer [14]. As a metallic underlayer, a 1.5 nm-thick

* Corresponding author.
E-mail address: sokasha@kyudai.jp (S. Okasha).

https://doi.org/10.1016/j.tsf.2021.138784
Received 12 January 2021; Received in revised form 2 June 2021; Accepted 6 June 2021
Available online 9 June 2021
0040-6090/

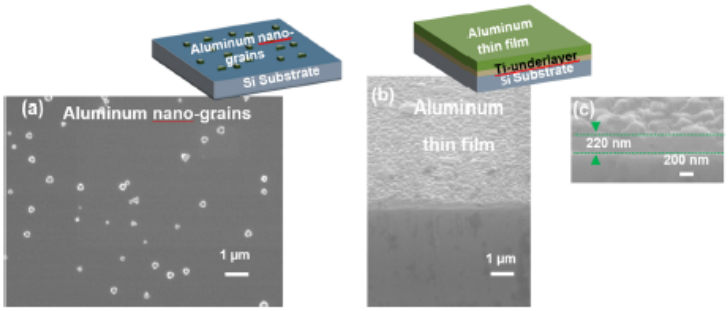

Fig. 1. SEM images with respective illustrative drawings of(a) Top view of aluminum nano-grains grown on the bare Si substrate, (b) titled-view (45°) of the aluminum thin film on the Si substrate with a titanium underlayer, and(c) cross section image of average-thickness of aluminum thin film.

titanium film is deposited on the silicon substrate by electron-beam with a very low deposition rate of 0.05 nm/sec., which gives a smooth surface. After the deposition of Ti seed layer on the Si substrate, the substrate must be installed into the ALD chamber within half an hour in order to avoid the surface oxidation.

The growth of aluminum from DMEAA is not a self-limited process, thus an aluminum monolayer (ML) growth can be tuned by the combination of an amount of DMEAA which is determined by the valve opening time of DMEAA, t_{open}, purging time removing by-products from the chamber, t_{purge}, and the growth temperature in the chamber, T. The ALD chamber is equipped with the hot-wall and thus the whole chamber is kept at the same temperature during the film growth. By adjusting three conditions, we can obtain 0.3 ML to 4 ML growth per cycle (GPC). The following results were obtained with the growth conditions of 300 ALD cycles that t_{open}, t_{purge}, and T are 0.3 s, 3.0 s, and 150 °Celsius, respectively.

The surface morphology of one of the aluminum thin film and its thickness are characterized by field emission scanning electron microscopy (SEM, JEOL JSM-6340F capable of getting image resolution of 3 nm). The rough estimate of the surface roughness was obtained from a 45° tilted view of cross-section SEM image of an Al film prepared over a Ti underlayer. No signal filtering was applied and data was corrected for the tilted geometry. The average distance between the edges of the Ti layer and along the lumen was evaluated. Moreover, the maximum peak-to-valley (PV) distance and root mean square (RMS) roughness of the edge of the Al film with the lumen were also estimated, all of these with the help of the Gatan digital micrograph ver. 3.4. The composition and crystal orientation of the two films were estimated from X-ray diffraction (XRD) measurements performed with XRD (Rigaku TTR-III) apparatus, using a Cu Kα x-ray source (1.5406 Å) and the apparatus software package.

The resistance measurements were performed into the 0.3 K refrigerator with a 3 T superconducting magnet. The temperature was measured by the ruthenium oxide thermometer located at the sample stage.

3. Results and discussion

Fig. 1(a) and (b) show the SEM images of the grown thin film of aluminum on a silicon substrate without and with a titanium underlayer, respectively. We grow aluminum thin films onto the bare silicon substrates at various growth conditions. However, in the absence of a Ti underlayer, only aluminum nano-grains were obtained on the Si substrate as shown in Fig. 1(a). On the other hand, as shown in Fig. 1(b), aluminum thin film with the Ti underlayer shows a mirror-like smooth surface. We speculate that Ti removes hydrogen ions from alane (AlH_3) in a similar mechanism of the decomposition of alane by titanium (IV)

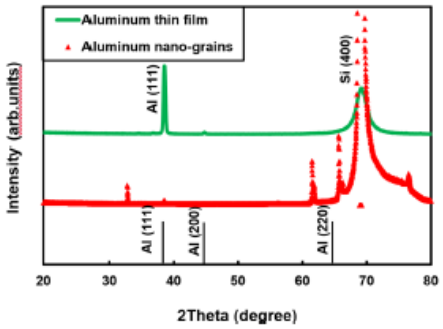

Fig. 2. XRD analysis shows the aluminum texture of (111) orientation at 2Θ ° = 38.5° for both the thin film and nano-grains along with stacked lines of the standard reference at the bottom. The peak at 2Θ ° = 69° represents Si (400) orientation of the substrate.

isopropoxide [15]. Indeed, aluminum films can't be obtained when a 1.5 nm thick Ti underlayer is exposed into the ambient atmosphere for more than half an hour due to the surface oxidation of a Ti film. The average thickness and standard deviation of the aluminum film grown for 300 ALD cycles with a GPC of 3ML/cycle are 220 ± 33 nm, and estimates of the RMS roughness and maximum observed peak-to-valley of the cleaved edge of the sample are 16 nm and 150 nm, respectively. The material choice of the underlayer is also considered. We found gold sometimes produces intermetallic compounds with aluminum, which may become an insulator [16]. We choose a very thin titanium film as the underlayer in this work.

XRD measurements indicate that an aluminum film with the Ti seed layer on the Si substrate has (111) orientation with a peak of 2Θ ° = 38.5° [17] as shown in Fig. 2. The peak at 2Θ° = 69° represents Si (400) orientation of the substrate. Al (111) is an ideal orientation due to the high resistance of stress migration with a longer lifetime as an electrode for device applications [17,18]. We also grew aluminum films on other substrates, such as GaAs and sapphire, with a Ti under layer and found all of the aluminum films show (111) orientation. Our results are coincident with the reference [17]. Further analysis for the XRD peak of Al (111) at 2Θ ° = 38.5° is performed to acquire crystal information of the grown thin film. The full width at half maximum (FWHM) value was obtained to be 0.295°. The plane distance of the grown aluminum (111) thin film was derived to be 0.233 nm. The mean grain size of the aluminum thin film was 32 nm calculated from the Scherrer equation as following: $Lc = (K_\lambda)/(FWHM^*Cos\theta)$, where Lc is crystallite size, $K = 1$.

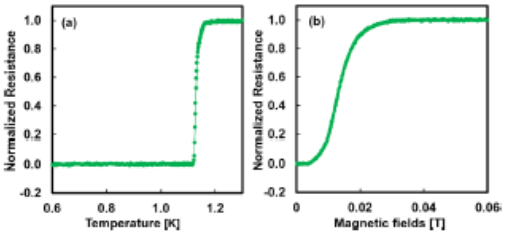

Fig. 3. (a) The temperature dependence with zero magnetic fields and (b) the magnetic field dependence with $T = 0.3$ K of the aluminum film with the thickness of 110 nm. The resistance is normalized.

Fig. 3 shows the temperature and magnetic field dependence of the aluminum film with the thickness of 110 nm. The onset of the superconducting transition temperature is 1.18 K which is very close to the bulk value, 1.19 K [19]. It is well known that thin aluminum films show the enhancement of superconductivity due to either impurity effects [20] or phonon softening [21,22]. As measured by XRD, the (111) plane distance of 0.233 nm for the grown aluminum thin film Al (111) plane distance of the Al thin film is almost same as that of 0.234 nm for bulk aluminum [23]. These suggest that grown Al films are very pure and ideal thin films. However, the magnetic field dependence of the aluminum film at 0.3 K shows rather a broad transition although aluminum is a type I superconductor, which implies that the distribution of aluminum grains may play a role [24].

As we already pointed out, aluminum film only grows onto the metallic layer, not on the bare silicon substrate. This gives the selective growth of aluminum thin film onto the Ti seed layer and it is very useful for fabricating superconducting small Josephson tunnel junctions, which have the nominal area less than $100 \times 100\ nm^2$. Current standard fabrication of small Josephson tunnel junctions uses the shadow evaporation technique with a suspended bridge [25]. As the etching process of small Josephson tunnel junctions causes the degraded junction quality, the suspended bridge technique is only the way to fabricate small Josephson tunnel junctions. However, the suspended bridge technique leaves unnecessary patterns due to the pattern shift [26] and it makes difficult to fabricate large integrated circuits of small Josephson tunnel junctions. Our findings of the selective area growth of aluminum thin films may enable us to fabricate the self-aligned vertical type of small Josephson tunnel junctions and contribute to a way of making superconducting quantum circuits, such as superconducting quantum bits.

4. Conclusion

We grew uniform aluminum (111) thin film using the atomic layer deposition technique with dimethylethylaminealane precursor. A smooth aluminum thin film with strong texture of (111) is obtained by using the titanium underlayer regardless of the substrate materials. The superconducting transition temperature of the grown aluminum thin films is the same as the bulk one and the lattice constant of the thin films is coincident with the bulk one, which indicates aluminum thin films are high quality. The selective area growth has the potential to obtain the way to fabricate self-aligned vertical Josephson tunnel junctions.

CRediT authorship contribution statement

Sameh Okasha: Conceptualization, Methodology, Software, Formal analysis, Investigation, Writing – original draft, Writing – review & editing, Visualization. **Yoshiaki Sekine:** Resources, Writing – review & editing. **Satoshi Sasaki:** Resources, Writing – review & editing. **Yuichi Harada:** Supervision, Conceptualization, Methodology, Project administration, Writing – review & editing, Funding acquisition, Investigation.

Declaration of Competing Interest

The authors declare that they have no known competing financial interests or personal relationships that could have appeared to influence the work reported in this paper.

Acknowledgments

One of the authors is grateful for the financial assistance provided by the green Asia program at Kyushu University.

References

[1] R.L. Puurunen, Surface chemistry of atomic layer deposition: a case study for the trimethylaluminum/water process, J. Appl. Phys. 97 (2005) 1–52, https://doi.org/10.1063/1.1940727, https://doi.org/.
[2] S. Sasaki, K. Tateno, G. Zhang, H. Pigot, Y. Harada, S. Saito, A. Fujiwara, T. Sogawa, K. Muraki, Self-aligned gate-all-around InAs/InP core-shell nanowire field-effect transistors. Jpn. J. Appl. Phys., Japan Society of Applied Physics, 2015, p. 04DN04, https://doi.org/10.7567/JJAP.54.04DN04, https://doi.org/.
[3] H. Irie, Y. Harada, H. Sugiyama, T. Akazaki, Josephson coupling through one-dimensional ballistic channel in semiconductor-superconductor hybrid quantum point contacts, Phys. Rev. B - Condens. Matter Mater. Phys. 89 (2014), 165415, https://doi.org/10.1103/PhysRevB.89.165415 https://doi.org/.
[4] K. Hirama, H. Sato, Y. Harada, H. Yamamoto, M. Kasu, Thermally stable operation of h-terminated diamond FETs by NO 2 adsorption and Al 2O 3 passivation, IEEE Electron Device Lett 33 (2012) 1111–1113, https://doi.org/10.1109/LED.2012.2200230, https://doi.org/.
[5] S.M. George, Atomic layer deposition: an overview, Chem. Rev. 110 (2010) 111–131, https://doi.org/10.1021/cr900056b, https://doi.org/.
[6] Y.J. Lee, S.-.W. Kang, Study on the characteristics of alumdinum thin films prepared by atomic layer deposition, J. Vac. Sci. Technol. A Vacuum, Surfaces, Film. 20 (2002) 1983, https://doi.org/10.1116/1.1513636, https://doi.org/.
[7] H. Matsuhashi, C.H. Lee, T. Nishimura, K. Masu, K. Tsubouchi, Superiority of DMAH to DMEAA for al CVD technology, Mater. Sci. Semicond. Process. 2 (1999) 303–308, https://doi.org/10.1016/S1369-8001(99)00032-3, https://doi.org/.
[8] K. Tsubouchi, K. Masu, Area-selective CVD of metals, Thin Solid Films 228 (1993) 312–318, https://doi.org/10.1016/0040-6090(93)90624-X, https://doi.org/.
[9] S.P. Douglas, C.E. Knapp, Low-Temperature Deposition of Highly Conductive Aluminum Metal Films on Flexible Substrates Using Liquid Alane MOD Precursors, ACS Appl. Mater. Interfaces. 12 (2020) 26193–26199, https://doi.org/10.1021/acsami.0c05429, https://doi.org/.
[10] H.M. Lee, J.Y. Seo, A. Jung, S.Y. Choi, S.H. Ko, J. Jo, S. Bin Park, D. Park, Long-term sustainable aluminum precursor solution for highly conductive thin films on rigid and flexible substrates, ACS Appl. Mater. Interfaces. 6 (2014) 15480–15487, https://doi.org/10.1021/am504134f, https://doi.org/.
[11] W.L. Gladfelter, D.C. Boyd, K.F. Jensen, Trimethylamine Complexes of Alane as Precursors for the Low-Pressure Chemical Vapor Deposition of Aluminum, Chem. Mater. 1 (1989) 339–343, https://doi.org/10.1021/cm00003a013, https://doi.org/.
[12] V. Shashkin, S. Rushworth, V. Danil'tsev, A. Murel, Y. Drozdov, S. Gusev, O. Khrykin, N. Vostokov, Microstructure and properties of aluminum contacts formed on GaAs(100) by low pressure chemical vapor deposition with dimethylethylamine alane source, J. Electron. Mater. 30 (2001) 980–986, https://doi.org/10.1007/BF02657721, https://doi.org/.
[13] P.T. Michaud, D. Babic, A Raman Study of Etching Silicon in Aqueous Tetramethylammonium Hydroxide, J. Electrochem. Soc. 145 (1998) 4040–4043, https://doi.org/10.1149/1.1838911, https://doi.org/.
[14] M.G. Simmonds, I. Taupin, W.L. Gladfelter, Selective Area Chemical Vapor Deposition of Aluminum Using Dimethylethylamine Alane, Chem. Mater. 6 (1994) 935–942, https://doi.org/10.1021/cm00043a012, https://doi.org/.
[15] B.D. Clark, C.J. Desantis, G. Wu, D. Renard, M.J. McClain, L. Bursi, A.L. Tsai, P. Nordlander, N.J. Halas, Ligand-Dependent Colloidal Stability Controls the Growth of Aluminum Nanocrystals, J. Am. Chem. Soc. 141 (2019) 1716–1724, https://doi.org/10.1021/jacs.8b12255, https://doi.org/.
[16] R.C. Blish, S. Li, H. Kinoshita, S. Morgan, A.F. Myers, Gold - Aluminum intermetallic formation kinetics, in: IEEE Trans. Device Mater. Reliab., 2007, pp. 51–63, https://doi.org/10.1109/TDMR.2007.891533, https://doi.org/.
[17] A. Kamijo, T. Mitsuzuka, A highly oriented Al[111]texture developed on ultrathin metal underlayers, J. Appl. Phys. 77 (1995) 3799–3804, https://doi.org/10.1063/1.358555, https://doi.org/.
[18] H. Shibata, M. Murota, K. Hashimoto, The effects of al(1,1l) crystal orientation on electromigration in half-micron layered a1 interconnects, Jpn. J. Appl. Phys. 32 (1993) 4479–4484, https://doi.org/10.1143/JJAP.32.4479, https://doi.org/.
[19] B.T. Matthias, T.H. Geballe, V.B. Compton, Superconductivity, Rev. Mod. Phys. 35 (1963) 1–22, https://doi.org/10.1103/RevModPhys.35.1, https://doi.org/.
[20] J.J. Hauser, Enhancement of superconductivity in aluminum films, Phys. Rev. B. 3 (1971) 1611–1616, https://doi.org/10.1103/PhysRevB.3.1611, https://doi.org/.

[21] R.B. Pettit, J. Silcox, Film structure and enhanced superconductivity in evaporated aluminum films, Phys. Rev. B. 13 (1976) 2865–2872, https://doi.org/10.1103/PhysRevB.13.2865, https://doi.org/.
[22] K. Houben, J.K. Jochum, S. Couet, E. Menéndez, T. Picot, M.Y. Hu, J.Y. Zhao, E. E. Alp, A. Vantomme, K. Temst, M.J. Van Bael, The influence of phonon softening on the superconducting critical temperature of Sn nanostructures, Sci. Rep. 10 (2020) 1–9, https://doi.org/10.1038/s41598-020-62617-4, https://doi.org/.
[23] R.J. Needs, Calculations of the surface stress tensor at aluminum (111) and (110) surfaces, Phys. Rev. Lett. 58 (1987) 53–56, https://doi.org/10.1103/PhysRevLett.58.53, https://doi.org/.
[24] R.W. Cohen, B. Abeles, Superconductivity in granular aluminum films, Phys. Rev. 168 (1968) 444–450, https://doi.org/10.1103/PhysRev.168.444, https://doi.org/.
[25] G.J. Dolan, Offset masks for lift-off photoprocessing, Appl. Phys. Lett. 31 (1977) 337–339, https://doi.org/10.1063/1.89690, https://doi.org/.
[26] D. Born, T. Wagner, W. Krech, U. Hübner, I. Fritzsch, Fabrication of ultrasmall tunnel junctions by electron beam direct-writing, in: IEEE Trans. Appl. Supercond., 2001, pp. 373–376, https://doi.org/10.1109/77.919360, https://doi.org/.

J Nanopart Res (2022) 24:242
https://doi.org/10.1007/s11051-022-05618-w

RESEARCH PAPER

Atomic layer deposition of self-assembled aluminum nanoparticles using dimethylethylamine alane as precursor and trimethylaluminum as an initiator

Sameh Okasha · Yuichi Harada

Received: 7 July 2022 / Accepted: 7 November 2022 / Published online: 19 November 2022

Abstract Our research provided a way to produce earth-abundant plasmonic nanoparticles with a well-defined orientation (111) for energy materials and nanosensing applications. In the atomic layer deposition (ALD) of aluminum nanoparticles, dimethylethylamine alane (DMEAA; AlH3N(CH3)2(CH2CH3)) has been employed as a processor of the aluminum source, while trimethylaluminum (TMA) as a growth initiator. We studied the morphology of self-assembled aluminum nanoparticle growth with the ALD process by passivating TMA on a silicon surface with previously absorbed hydroxyl groups. The reaction mechanism was proposed for the dissociation of the initiator (TMA), the precursor (DMEAA), and the effect of each one of them on the particle size by analyzing the obtained morphologies. Our results led us to theorize that to initiate the nucleation and the growth of aluminum nanoparticles, a conductive source of electrons is required such as TMA. We discussed the growth of aluminum nanoparticles as well as morphology step by step through SEM images. The observations showed that tetrahedrons of aluminum nanoparticles continue growing to octahedrons. The XRD analysis confirmed the orientation of aluminum nanoparticles in (111), in addition to obtaining their crystallinity information in-depth. This approach could allow for further development of new controlled morphologies and increase the knowledge in the growth of earth-abundant plasmonic nanoparticles.

Keywords Atomic layer deposition · Dimethylethylamine alane · Aluminum (111) · Nanoparticles · Trimethylaluminum · Polyhedron morphology

S. Okasha (✉) · Y. Harada
Global Innovation Center, Kyushu University, 6-1 Kasuga-Koen, Kasuga, Fukuoka 816-8580, Japan
e-mail: sokasha@kyudai.jp

S. Okasha
Molecular and Material Science Department, Interdisciplinary Graduate School of Engineering Sciences, Kyushu University, Kasuga, Fukuoka 816-8580, Japan

Introduction

Atomic layer deposition (ALD) is a technology to deposit conformal oxide and nitride thin films with the film's thickness being determined by the number of reaction cycles due to its self-limiting reaction growth mechanism. Therefore, the main advantage of ALD processes is that it gives atomic-scale control of the growth [1–3]. This technique can also be used to produce thin metallic films. In most cases, metal film growth by ALD does not have a self-limiting mechanism, but the growth conditions can be tuned in order to obtain a single atomic layer of metal per cycle [1, 4, 5].

Dimethylethylamine alane (DMEAA; AlH3: N(CH3)2(CH2CH3)) has been used successfully as an aluminum source and we produced the aluminum (111) thin film on a silicon (Si) substrate [6]. A conductive layer on a (Si) substrate is needed as a surface modification to produce aluminum thin films by DMEAA; however, there is no such ALD process to produce aluminum nanoparticles. There is a significant interest in the growth of plasmonic metal nanoparticles [7–13], and in particular, aluminum nanoparticles, as they have many applications such as high-performance energy materials [14], chromaticity devices such as flat panel displays [15], and nanosensing applications [16–20].

In this study, we produce and control the growth of aluminum nanoparticles by passivating and introducing trimethylaluminum (TMA) as an initiator before the main ALD growth process. DMEAA remains the main precursor of aluminum for the process under conditions that imitate a self-limiting growth mechanism per cycle. We designed three different experiments with different cycles of TMA and DMEAA to investigate the particle size distribution, orientation on the substrate, and morphology.

The orientation of aluminum nanoparticles was characterized by X-ray diffraction (XRD), while the crystallinity information was calculated using the integrated XRD apparatus software. A field emission scanning electron microscope (FESEM) was used to characterize the surface morphology and size of the grown nanoparticles [19–23]. The image processing of particle sizes was calculated by using GATAN software. The resulting SEM images showed the self-assembling of the aluminum atoms from tetrahedrons to octahedrons.

Experimental

Materials and the growth process

The atomic layer deposition chamber (SUNALE R-150, Picosun Oy.) was integrated with the glovebox covering the top of the chamber was used to grow aluminum as shown in Fig. 1(a). The glovebox is filled with pure nitrogen to prevent the oxidation of the samples before loading them into the ALD chamber. The concentration of the residual oxygen in the glovebox was controlled to be less than 0.1 ppm.

DMEAA precursor is decomposed into alane (AlH_3) at about 150 degrees Celsius [10–12], and it can be absorbed onto the Si substrate. Hydrogen reduction from alane occurs to initiate aluminum growth on the Si substrate. ALD growth process is based on surface reaction, which is the main difference from the gas-phase reaction in CVD. Our strategy to control the morphology growth is through modifying surface conditions. So, we used TMA as a passivation agent on the Si surface that was absorbed by OH^- groups; then, we start pulsing the main precursor (DMEAA) to the ALD chamber, which led

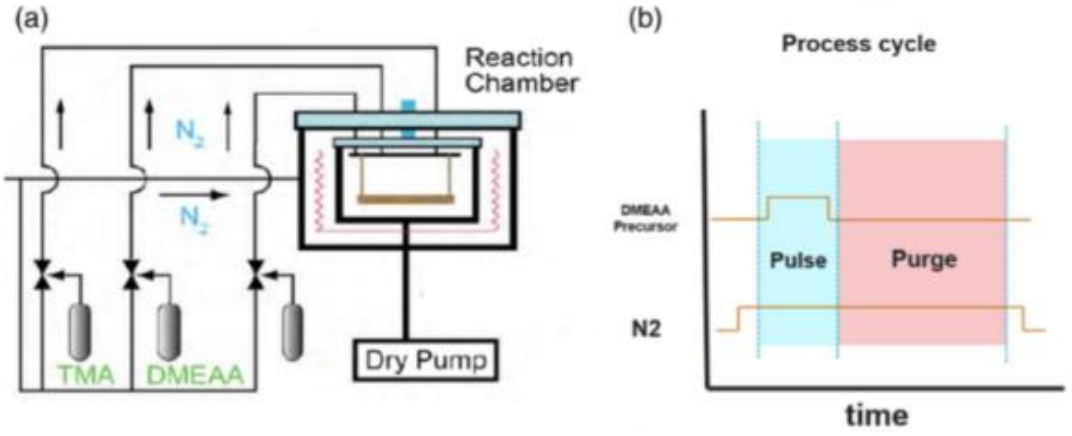

Fig. 1 (a) The schematic illustration of the atomic layer deposition chamber. (b) Process cycle of aluminum nanoparticles growth

to obtaining aluminum nanoparticles with a well-defined orientation.

Si substrates are prepared and cleaned by wet processes. The first step is a standard degreasing process using acetone and isopropanol. In the second step, Si substrates are dipped into SEMICO Clean 23 for two minutes [24] containing tetramethylammonium hydroxide aqueous solution to eliminate the contaminations and then rinsed in pure water. Finally, as a hydroxyl group (-OH) source, ethanol is sprayed onto Si substrates and dried up by a nitrogen blow gun. Then, the cleaned Si substrates are immediately loaded into the glovebox.

For our process, we demonstrate the capability to grow the aluminum nanoparticles by utilizing specific machine and experimental parameters. We defined the process parameters of the deposition cycle as the total time of pulse and purge as follows: the valve pulse time (t_{pulse}) and purging time (t_{purge}) as shown in Fig. 1(b), which were used to manage the cycles of the TMA and DMEAA. While the chamber temperature (T) was used as the growth temperature, the cycles of TMA and DMEAA were used to control the number of monolayers (ML) instead of the convenient self-limiting process of ALD. The hot wall, equipped with the ALD chamber, maintained a growth temperature of 150 °C. We designed three experiments to study the effects of the TMA and DMEAA cycles and they are as follows:

1. Experiment (A) TMA had 20 cycles, while DMEAA has 200 cycles
2. Experiment (C) TMA had 20 cycles, while DMEAA has 400 cycles
3. Experiment (D) TMA had 10 cycles, while DMEAA has 300 cycles

The initial stage's growth parameters of TMA, t_{pulse} and t_{purge}, are 0.1 s and 3.0 s, respectively. Simultaneously, t_{pulse} and t_{purge} at the second stage of DMEAA were 0.3 and 3.0 s, respectively. The flow rate of the carrier gas, N_2 for TMA and DMEAA, is set to be 150 and 100 sccm, respectively.

Characterization techniques

The characterizations of the nanoparticles' crystallinity were carried out by an XRD machine (Rigaku TTR-II), which is equipped with an X-ray source of Cu Kα = 1.5406 Å. The scan step and scan time are selected carefully as 0.02 degree and 2 degree/min., respectively, using the continuous mode with machine power of 50 kV and 300 mA to maximize the XRD peaks of the nanoparticles. The crystallinity information was calculated using the integrated XRD apparatus software. FESEM (JEOL JSM-6340F) was used to characterize the surface morphology of the grown nanoparticles and the particle size is measured by using a microscope image processing of GATAN software [25–27].

Results and discussion

Nanoparticles were self-assembled on the Si substrate after surface modifications explained in the last section. SEM images show the morphology of the isolated nanoparticle, as shown in Fig. 2(a–d) as a tetrahedron, polyhedron, and octahedron, respectively.

XRD measurements show that aluminum nanoparticles produced by (a), (c), and (d) conditions have a peak of $2\Theta^\circ = 38.5^\circ$ as shown in Fig. 3, which indicates (111) orientation [28, 29].

Besides, the substrate's Si (100) orientation has a peak of $2\Theta\ ^\circ = 69^\circ$ with their derived characteristic peaks between 60° and 70°. It was found that the highest peak of aluminum particles of (111) among our experiments required TMA 20 cycles at the first stage and DMEAA 400 cycles at the second stage, as shown in experiment (c) in Fig. 3. That gives the impression that (C) was the most efficient method to fabricate Al nanoparticles. Alane (311) was also detected in samples (C) and (D) at the peak of $2\Theta^\circ = 32^\circ$ [30]. Further detailed analysis of the XRD peak of Al (111) at $2\Theta^\circ = 38.5^\circ$ was performed to acquire the crystal information of the grown particles. The full width at half maximum (FWHM) values of the nanoparticles from experiments (A), (C), and (D) were 0.275, 0.303, and 0.261°, respectively. The difference in the FWHM values could reflect the purity of the aluminum (111) nanoparticles. The plane distance of the grown aluminum (111) was 0.233 nm. The mean crystallite sizes of the aluminum nanoparticles of (A) and (C), and (D) were estimated to be 34, 31, and 36 nm, respectively, calculated from the Scherrer equation: $Lc = (K\lambda)/(FWHM*Cos\theta)$, where Lc is the crystallite size, K = 1. Thus, the XRD peak angle analysis confirmed the

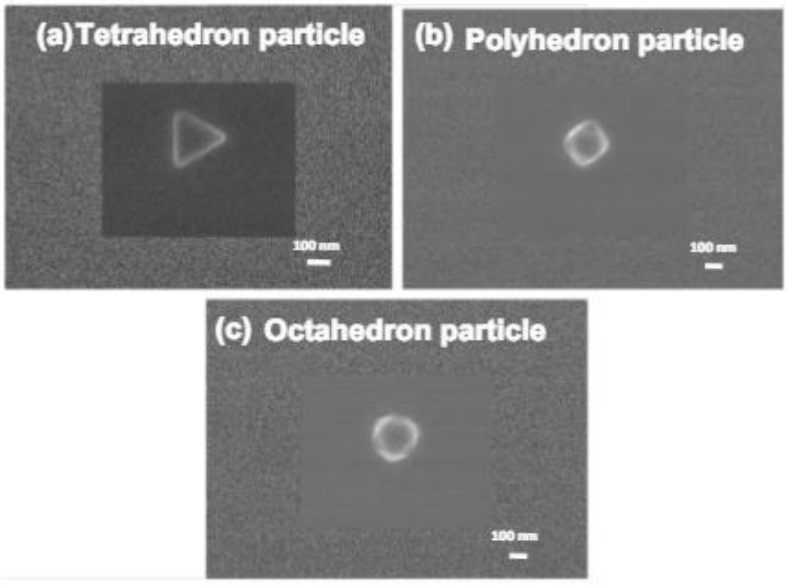

Fig. 2 SEM images of (**a**) single-particle of tetrahedron morphology, (**b**) single-particle of polyhedron morphology, and (**c**) single-particle of octahedron morphology

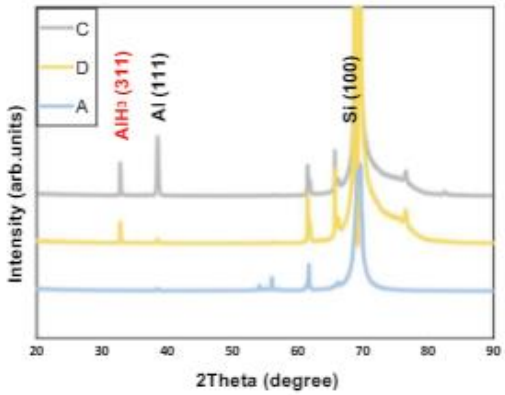

Fig. 3 XRD analysis shows the aluminum nanoparticles of (111) orientation at 2 Θ °=38.5°. The peak at 2Θ°=69° represents the substrate's Si (100) orientation

nanoparticles that appeared in the SEM images shown in Fig. 2 are aluminum nanoparticles (111).

Our results lead us to theorize that to enable initiating the nucleation and the growth of aluminum nanoparticles, a conductive source of electrons is required. In our case of the aluminum nanoparticles growth, TMA associated with OH-groups was the initial source of the electron; then, the self-assembled aluminum atoms on the surface keep growing by adsorbing more DMEAA in the following theoretical pathway of reaction mechanism:

The chemisorption of the TMA due to the dihydrogen-bonded (DHB) [31] of the proton-transfer or H-elimination by the surface chemisorption of the TMA with (-OH) groups is as shown in Eq. (1), so we intentionally introduced it during the cleaning process of Si-substrates as part of Lewis' acid–base complex pathway [32]. The adsorption (ads) pathway reactions are as follows:

$$(CH4)3Al\ (g) + OH^{-}(ads) \rightarrow (CH3)2AlOH\ (ads) + CH_{4}\ (g) \quad (1)$$

The dissociation of DMEAA starts with removing the amine ligand as in equation (2); then, the ligand of DMEA desorbing in equation (3). Finally, the adsorbed molecule of TMA reacts with the adsorbed molecule of alane forming aluminum atoms and releasing methane and water from equation (4) by removing hydrogen ions from alane (AlH_3) itself. The last reaction is similar to the decomposition mechanism of alane by titanium [6, 33] turning to methane [34].

$$C2H5(CH3)2NAlH3\ (g) \rightarrow AlH3(ads) + C2H5(CH3)2N\ (ads) \quad (2)$$

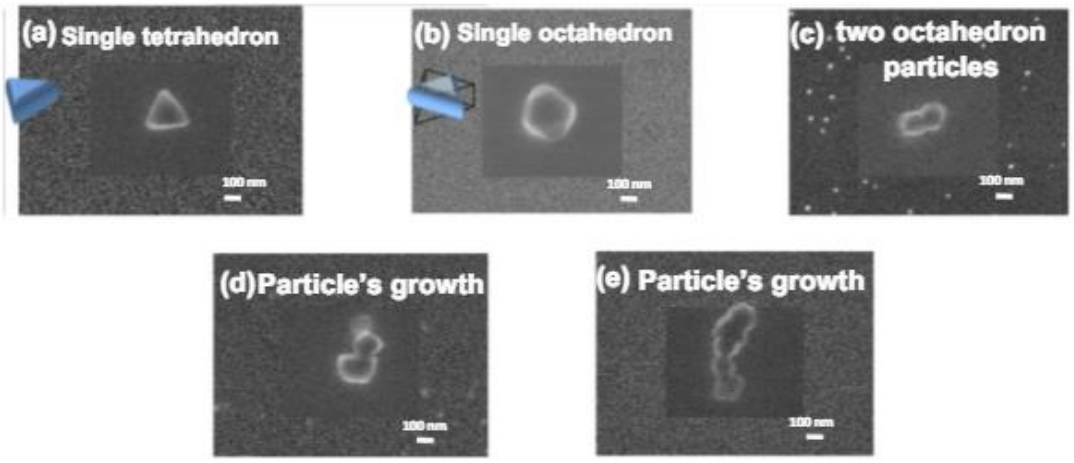

Fig. 4 SEM images of aluminum crystallites growth on the bare Si substrate (**a**) isolated tetrahedron crystallite, (**b**) isolated octahedron crystallite, (**c**) two octahedron particles, and (**d**, **e**) particle growth

$$C2H5(CH3)2\ N\ (ads) \rightarrow C2H5(CH3)2N\ (g) \quad (3)$$

$$AlH3\ (ads) + (CH3)2AlOH\ (ads) \rightarrow 2Al\ (s) + 2CH4\ (g) + H2O\ (g) \quad (4)$$

With more cycles of DMEAA, the ligand of the amine group keep desorbing in form of DMEA, and aluminum keeps growing as nanoparticles without oxidation [18]. That reaction mechanism is revealed from the reactant gasses that we fed and products that we analyzed by XRD in Fig. 3.

To study the effects of TMA cycles on particle size, we measured results from the three designed experiments. The average size of the aluminum nanoparticles of (A), (C), and (D) is 130, 180, and 120 nm, respectively. From the statistical comparison of experiments (A) and (D), in the case of a high number of cycles of TMA in experiment (A), we obtained a bigger size of nanoparticle of aluminum in (A) than in (D), even though we have a higher number of the cycles of DMEAA in (D). That shows clearly the initial cycle of TMA is more crucial to controlling the size growth of the nanoparticles. After that, the cycles of DMEAA are secondary to increasing the particle size, as concluded from the experiments comparison between (A) and (C).

From our investigation of particles morphology growth, we found the initial aluminum particle coalesce as tetrahedrons, as shown in Fig. 4(a), then grows to octahedrons in Fig. 4(b) and then keep growing in Fig. 4(c–e). The SEM images indicate that the initial texture growth of aluminum is an orientation-independent process that comes from self-nucleated crystallites during the deposition process of ALD. The geometry of the particles changes with the accumulative deposition during aluminum growth. The reasons for polyhedron structures could be due to the atomic binding energy, fragmentation energy [35], and geometry shape stability [36]. Stating the fact that aluminum is a metal with face-centered cubic (FCC), that makes (111) planes have the most stable surface energy and preferable to be grown rather than (100) [36, 37]. Our work proposes TMA is essential as an initiator to grow aluminum nanoparticles on Si-substrate in (111) orientation when using DEMAA precursor for the ALD process. The results open the door to growing plasmonic nanoparticles of aluminum in a well-defined orientation of (111) for their applications.

Conclusion

Using TMA as a passivation agent, we were able to grow aluminum nanoparticles (111) by ALD technology using a DMEAA as the main precursor. The SEM images show aluminum nanoparticles

have morphologies of tetrahedrons and octahedrons. The orientation of aluminum nanoparticles of (111) is confirmed by XRD. TMA chemisorbed by OH^- groups on Si substrate surface as Lewis complex initiates the dehydration of AlH_3 in DMEAA, enabling the assembly of aluminum nanoparticles in the (111) orientation and liberating methane. The tetrahedron (111) growth can be linked to the geometric shape and surface stability. As the growth continues, the tetrahedron aluminum nanoparticles grow to octahedrons. From our experiments and particle size analysis, the TMA cycles are more essential for growing aluminum nanoparticles and achieving bigger particle sizes than DMEAA cycles. Our well-defined orientation of plasmonic aluminum nanoparticles can be used in energy, nanosensing applications, and chromaticity devices.

Acknowledgements We sincerely thank Nippon Telegraph and Telephone Basic Research Laboratories (NTTBRL), Dr. Yoshiaki Sekine, and Dr. Satoshi Sasaki for allowing us to use their facilities, including the cleanroom.

Declarations

Ethics approval The authors declare that the current research was conducted in agreement with all existing ethical standards.

Consent to participate All authors have their consent to participate in this research.

Consent for publication All authors have their consent to participate in this publication as it is presented here.

Conflict of interest The authors declare that they have no conflict of interest.

References

1. Puurunen RL (2005) Surface chemistry of atomic layer deposition: a case study for the trimethylaluminum/water process. J Appl Phys 97:1–52. https://doi.org/10.1063/1.1940727
2. Hirama K, Sato H, Harada Y et al (2012) Thermally stable operation of h-terminated diamond FETs by NO 2 adsorption and Al 2O 3 passivation. IEEE Electron Device Lett 33:1111–1113. https://doi.org/10.1109/LED.2012.2200230
3. George SM (2010) Atomic layer deposition: an overview. Chem Rev 110:111–131. https://doi.org/10.1021/cr900056b
4. Sasaki S, Tateno K, Zhang G et al (2015) Self-aligned gate-all-around InAs/InP core-shell nanowire field-effect transistors In: Japanese Journal of Applied Physics. Japan Soc Appl Phys 54(4S):04DN04
5. Irie H, Harada Y, Sugiyama H, Akazaki T (2014) Josephson coupling through one-dimensional ballistic channel in semiconductor-superconductor hybrid quantum point contacts. Phys Rev B Condens Matter Mater Phys 89:165415. https://doi.org/10.1103/PhysRevB.89.165415
6. Okasha S, Sekine Y, Sasaki S, Harada Y (2021) Atomic layer deposition of aluminum (111) thin film by dimethylethylaminealane precursor. Thin Solid Films 732:138784. https://doi.org/10.1016/j.tsf.2021.138784
7. Lee JH, Kamada K, Enomoto N, Hojo J (2007) Morphology-selective synthesis of polyhedral gold nanoparticles: what factors control the size and morphology of gold nanoparticles in a wet-chemical process. J Colloid Interface Sci 316:887–892. https://doi.org/10.1016/J.JCIS.2007.08.053
8. Henzie J, Andrews SC, Ling XY et al (2013) Oriented assembly of polyhedral plasmonic nanoparticle clusters. Proc Natl Acad Sci U S A 110:6640–6645. https://doi.org/10.1073/PNAS.1218616110/SUPPL_FILE/SM04.MP4
9. Polani S, Melamed S, Burlaka L et al (2017) Large-scale synthesis of polyhedral Ag nanoparticles for printed electronics. RSC Adv 7:54326–54331. https://doi.org/10.1039/C7RA11370F
10. Montaño-Priede JL, Pal U (2019) Estimating near electric field of polyhedral gold nanoparticles for plasmon-enhanced spectroscopies. J Phys Chem C 123:11833–11839. https://doi.org/10.1021/ACS.JPCC.9B01105/SUPPL_FILE/JP9B01105_SI_001.PDF
11. Tang P, Xing M, Zhong L et al (2022) Polyhedral-Au@SiO2@Au core–shell nanoparticle reveals a broadband and tunable strong local field enhancement. J Phys Chem C 126:8165–8176. https://doi.org/10.1021/ACS.JPCC.2C01586
12. Agarwal D, Aspetti CO, Cargnello M et al (2017) Engineering localized surface plasmon interactions in gold by silicon nanowire for enhanced heating and photocatalysis. Nano Lett 17:1839–1845. https://doi.org/10.1021/ACS.NANOLETT.6B05147/ASSET/IMAGES/LARGE/NL-2016-051475_0004.JPEG
13. Jacobson CR, Wu G, Alemany LB et al (2022) A dual catalyst strategy for controlling aluminum nanocrystal growth. Nano Lett 22(13):5570–5574. https://doi.org/10.1021/ACS.NANOLETT.2C01854
14. Shahravan A, Desai T, Matsoukas T (2014) Passivation of aluminum nanoparticles by plasma-enhanced chemical vapor deposition for energetic nanomaterials. ACS Appl Mater Interfaces 6:7942–7947. https://doi.org/10.1021/AM5012707/SUPPL_FILE/AM5012707_SI_001.PDF
15. Olson J, Manjavacas A, Basu T et al (2016) High chromaticity aluminum plasmonic pixels for active liquid crystal displays. ACS Nano 10:1108–1117. https://doi.org/10.1021/ACSNANO.5B06415/SUPPL_FILE/NN5B06415_SI_004.AVI
16. Lin SW, Wu JY, di Lin S et al (2013) Characterization of single-crystalline aluminum thin film on (100) GaAs substrate. Jpn J Appl Phys 52:045801. https://doi.org/10.7567/JJAP.52.045801
17. Miller KK, Gottfried JL, Walck SD et al (2019) Plasma surface treatment of aluminum nanoparticles for energetic material applications. Combust Flame 206:211–213. https://doi.org/10.1016/j.combustflame.2019.04.042

18. Meziani MJ, Bunker CE, Lu F et al (2009) Formation and properties of stabilized aluminum nanoparticles. ACS Appl Mater Interfaces 1:703–709. https://doi.org/10.1021/am800209m
19. Katyal J, Soni RK (2013) Size- and shape-dependent plasmonic properties of aluminum nanoparticles for nanosensing applications. J Mod Opt 60:1717–1728. https://doi.org/10.1080/09500340.2013.856483
20. Schefflan R, Kovenklioglu S, Kalyon D et al (2006) Formation of aluminum nanoparticles upon condensation from vapor phase for energetic applications. J Energ Mater 24:141–156. https://doi.org/10.1080/07370650600672041
21. Gladfelter WL, Boyd DC, Jensen KF (1989) Trimethylamine complexes of alane as precursors for the low-pressure chemical vapor deposition of aluminum. Chem Mater 1:339–343. https://doi.org/10.1021/cm00003a013
22. Shashkin V, Rushworth S, Danil'tsev V et al (2001) Microstructure and properties of aluminum contacts formed on GaAs(100) by low pressure chemical vapor deposition with dimethylethylamine alane source. J Electron Mater 30:980–986. https://doi.org/10.1007/BF02657721
23. Douglas SP, Knapp CE (2020) Low-temperature deposition of highly conductive aluminum metal films on flexible substrates using liquid alane MOD precursors. ACS Appl Mater Interfaces 12:26193–26199. https://doi.org/10.1021/acsami.0c05429
24. Michaud PT, Babic D (1998) A Raman study of etching silicon in aqueous tetramethylammonium hydroxide. J Electrochem Soc 145:4040–4043. https://doi.org/10.1149/1.1838911
25. Hezave AZ, Esmaeilzadeh F (2010) Investigation of the rapid expansion of supercritical solution parameters effects on size and morphology of cephalexin particles. J Aerosol Sci 41:1090–1102. https://doi.org/10.1016/j.jaerosci.2010.08.004
26. Kim H, Han J, Han TYJ (2020) Machine vision-driven automatic recognition of particle size and morphology in SEM images. Nanoscale 12:19461–19469. https://doi.org/10.1039/d0nr04140h
27. Roth GA, Neu-Baker NM, Brenner SA (2015) SEM analysis of particle size during conventional treatment of CMP process wastewater. Sci Total Environ 508:1–6. https://doi.org/10.1016/j.scitotenv.2014.11.075
28. Kamijo A, Mitsuzuka T (1995) A highly oriented Al[111] texture developed on ultrathin metal underlayers. J Appl Phys 77:3799–3804. https://doi.org/10.1063/1.358555
29. Xu X, Liu Z, Zhang B et al (2019) Effect of Mn content on microstructure and properties of 6000 series aluminum alloy. Appl Phys A Mater Sci Process 125:490. https://doi.org/10.1007/s00339-019-2780-9
30. Xu B, Liu J, Wang X (2014) Preparation and thermal properties of aluminum hydride polymorphs. Vacuum 99:127–134. https://doi.org/10.1016/j.vacuum.2013.05.009
31. Filippov OA, Tsupreva VN, Golubinskaya LM et al (2009) Proton-transfer and H2-elimination reactions of trimethylamine alane: role of dihydrogen bonding and Lewis acid-base interactions. Inorg Chem 48:3667–3678. https://doi.org/10.1021/IC802262H/SUPPL_FILE/IC802262H_SI_001.PDF
32. Corma A, García H (2003) Lewis acids: from conventional homogeneous to green homogeneous and heterogeneous catalysis. Chem Rev 103:4307–4365. https://doi.org/10.1021/CR030680Z
33. Clark BD, Desantis CJ, Wu G et al (2019) Ligand-dependent colloidal stability controls the growth of aluminum nanocrystals. J Am Chem Soc 141:1716–1724. https://doi.org/10.1021/jacs.8b12255
34 Parsons GN, George SM (2011) Knez M (2011) Progress and future directions for atomic layer deposition and ALD-based chemistry. MRS Bulletin 36(11):865–871. https://doi.org/10.1557/MRS.2011.238
35. Arab A, Habibzadeh M (2016) Theoretical study of geometry, stability and properties of Al and AlSi nanoclusters. J Nanostructure Chem 6:111–119. https://doi.org/10.1007/s40097-015-0185-7
36. Guisbiers G, Abudukelimu G (2013) Influence of nanomorphology on the melting and catalytic properties of convex polyhedral nanoparticles. J Nanopart Res 15:1–12. https://doi.org/10.1007/s11051-013-1431-x
37. Ahlrichs R, Elliott SD (1999) Clusters of aluminium, a density functional study. Phys Chem Chem Phys 1:13–21. https://doi.org/10.1039/a807713d